BULK FOIL PT-RH MICRO-RELAYS FOR HIGH POWER RF AND OTHER APPLICATIONS

by

Fatih Mert Ozkeskin

A dissertation submitted in partial fulfillment of the requirements for the degree of Doctor of Philosophy (Mechanical Engineering) in The University of Michigan 2011

Doctoral Committee:

Professor Yogesh B. Gianchandani, Chair
Professor Kamal Sarabandi
Associate Professor Katsuo Kurabayashi
Assistant Professor Mina Rais-Zadeh

© Fatih Mert Ozkeskin

2011

To father, Tayfur Ozkeskin

ACKNOWLEDGEMENTS

First of all, I would like to thank and express my deepest gratitude to my research advisor Professor Yogesh B. Gianchandani for his endless support, mentoring and encouragement throughout my doctoral study. Second of all, I would like to thank Professor Kamal Sarabandi for his invaluable guidance. I would also like to thank Professor Katsuo Kurabayashi and Professor Mina Rais-Zadeh for being in my dissertation committee.

I would like to thank Dr. Tao Li and Dr. Mark Richardson for being great mentors and for training me on the μEDM which I have used extensively. I would also like to thank to Sangjo Choi, for spending a great deal of effort and countless of hours for RF design and testing. I would like to thank to Dr. Adip Nashashibi for helping with RF testing equipment. I am also indebted to all the WIMS and SSEL staff especially to Trasa Bukhardt and Fran Doman for taking care of all my administrative work and research purchases.

I would like to thank my research group members Tao, Naveen, Karthik, Christine, Scott Wright, Scott Green, Allan, Heidi, Erwin, Jun, Ravish, Seungdo and Xin. It has been a wonderful experience working with them all along. I would also like to thank my friends, Erkan, Razi, Angelique, Ali, Jae Yoong, Daniel, Jeff, James, Seow Yuen, Tzeno, Yonghyun, Zhengzheng, Vikrant, Vikram, Morteza, Fikadu, Meysam,

Mehrnoosh, Jungsuek and many others who have made my years at The University of Michigan memorable ones.

Finally, I would like to thank my parents and my sister for their unlimited love, support and encouragement without which I would have never reached this day.

TABLE OF CONTENTS

DEDICATION .... **ii**
ACKNOWLEDGEMENTS .... **iii**
LIST OF FIGURES .... **viii**
LIST OF TABLES .... **xviii**
ABSTRACT .... **xix**
Chapter

1. INTRODUCTION **1**

1.1 Types of micro-relays 2
1.1.1 DC micro-relays 2
1.1.2 RF micro-relays 4
1.2 Performance measures of MEMS switches 7
1.2.1 Figure of merit 10
1.2.2 Actuation voltage 12
1.2.3 Power handling 16
1.2.4 Switching speed 16
1.3 Contact resistance and material considerations in ohmic-contact micro-relays 18
1.3.1 Theoretical model 18
1.3.2 Contact metal selection 21
1.4 Micro electro-discharge machined bulk foil Pt-Rh relays for high power applications 22
1.4.1 Platinum-rhodium 23
1.4.2 Micro electro-discharge machining 24
1.5 Hybrid assembly and packaging on the printed circuit boards 28
1.6 Goals and approach…. 30
1.7 Outline 31

2. POWER HANDLING OF MEMS SWITCHES 32

2.1 Failure mechanisms and power handling of MEMS switches 33

2.1.1 Low-medium power failure mechanisms for MEMS capacitive switches….. 33

2.1.2 Low-medium power failure mechanisms for MEMS ohmic-contact switches 36

2.1.3 High power failure mechanisms for MEMS capacitive switches………….. 36

2.1.4 High power failure mechanisms for MEMS ohmic-contact switches 38

2.2 Quantitative benchmarking 40

3. MICROMACHINED Pt-Rh AND STAINLESS STEEL RELAYS FOR HIGH POWER DC APPLICATIONS 43

3.1 Design…. 43

3.2 Fabrication and assembly…. 53

3.3 Experimental evaluation…. 58

3.3.1 Electrical testing 58

3.3.2 Thermal testing 61

3.3.3 Lifetime testing 65

3.4 Discussion and conclusions…. 66

4. AN ALL-METAL MICRO-RELAY WITH BULK FOIL Pt-Rh CONTACTS FOR HIGH POWER RF APPLICATIONS 69

4.1 Design…. 70

4.2 Fabrication and assembly…. 79

4.3 Experimental evaluation…. 83

4.3.1 Electrical testing 83

4.3.2 Thermal testing 88

4.3.3 Lifetime testing 90

4.4 Discussion and conclusions…. 91

5. BATCH FABRICATED HIGH POWER RF MICRO-RELAYS WITH DIRECT ON-PCB PACKAGES...93

5.1 Design…. 93

5.2 Fabrication and assembly…. 104

5.3 Experimental evaluation…. 108

5.3.1 Electrical testing 108
5.3.2 Lifetime testing 117
5.3.3 Package testing 117
5.4 Discussion and conclusions…. 118
6. CONCLUSIONS AND FUTURE WORK **123**
6.1 Conclusions…. 123
6.2 Future work…. 127
APPENDIX **131**
BIBLIOGRAPHY **147**

LIST OF FIGURES

Figure 1.1: The SEM photographs of the micro-relays with different structures (a) A micro-relay with plate electrodes, (b) a micro-relay with a single beam and a single comb drive, (c) a micro-relay with a double-fold beam and a pair of comb drives [Li00]…………………………………………………………………………………...3

Figure 1.2: Orthogonal MEMS-series switches with (a) one electrode, (b) two electrodes, and (c) inline MEMS-series switches [Reb01] …………………………………………...9

Figure 1.3: Raytheon MEMS capacitive shunt switch: (a) cross-section view and (b) electrical RLC model [Gol96, Gol98]…………………………………………………....9

Figure 1.4: S-parameters of a MEMS capacitive shunt switch, (a) up-state position and (b) down-state position [Mul00]…………………………………………………………12

Figure 1.5: (a) A MEMS fixed-fixed (suspended) beam, (b) cantilever beam [Reb03] ……………………………………………………………………………………………12

Figure 1.6: The beam height versus the applied voltage for exemplary values of W=w=100 µm, g_0=3 µm and k=10 N/m. The pull-in voltage is 30 V. Dashed line is the unstable portion of the beam height [Reb03]……………………………………..……..15

Figure 1.7: (a) Cross section of a miniature switched capacitor, (b) SEM picture a miniature switched capacitor [Lac06]…………………………………………………17

Figure 1.8: (a) Surface profile of contact having multiple asperities, (b) calculated contact radius versus contact force for a gold contact [Maj97] …………………………19

Figure 1.9: Measured contact resistance of Au, $AuNi_5$ and Rh [Sch98] ……………….21

Figure 1.10: Electrical resistivity versus hardness for various metal films (1500 nm thickness) on the Si substrate, expanded from [Lee06] ………………………………23

Figure 1.11: Material hardness versus resistivity of Pt-Rh (80:20) compared with several alloys and pure metals…………………………………………………………25

Figure 1.12: Electrical configuration and setup for µEDM adapted from [Tak05]……..26

Figure 1.13: Machining mechanism of μEDM. Normal discharges are shown in Steps 1-4. In step 5, repeated discharges cause debris accumulation. Eventually, excess amounts of debris lead to discharges through debris accumulations clusters and individual debris particles shown in the middle and at the edges respectively [Ric08] ……………….…27

Figure 1.14: Schematic of the batch mode μEDM setup used for fabrication of microtools [Li09]…………………………………………………...…………………27

Figure 1.15: SEM image of the RF MEMS switch (a) CPW etch profile. (b) Switch with 200 μm wide Al membrane [Cha05] ……………………………………………..……29

Figure 2.1: SEM image of RF-MEMS switch adhered to substrate [Zha03]...…………35

Figure 2.2: Stiction release design (a) device SEM image, (b) mechanism schematic [Tou08]..………………………………………………...…………………………35

Figure 2.3: (a) Clean gold contact, (b) contact after pitting and hardening under high actuation voltages, (c) hardness measurements done using AFM probe [Mih01b]……...36

Figure 2.4: Self-actuation mechanism. (a) The switch is initially in its up-state over a CPW line. (b) RF generated force on the CPW line is higher than the pull-in force and the switch is actuated with no bias voltage present [Per03]….…………………………37

Figure 2.5: Mechanism of the breakdown due to small peak in rough dielectric layer surface [Hou07]…………………………………………...……..………………37

Figure 2.6: Pictures of the capacitive MEMS switch after the dielectric breakdown [Hou07]……………………………………………………..…………………...…38

Figure 2.7: Illustration of the surface asperities and their contribution to high current induced heating. Heating due to the current flow in the contact spot leads to a resistance decrease caused by the material annealing or film breakdown [Jen05]….………………39

Figure 2.8: SEM image of a melted gold contact due to excessive heating [Jen05]……40

Figure 3.1: (a) Exploded view of micro-relay showing double cantilever structure. Gold posts align and hold the cantilever over gold-coated copper traces on the PCB. Recess depths are 2 μm and 100 μm on contact and actuation cantilevers respectively. The actuation cantilever is isolated from the contact cantilever and pushes it down via thermally conductive microsphere. An extension at the tip prevents pull-in. Heat sink is integrated atop. The design has an actuation area of 1.32 mm^2 as defined by the footprint of the pull down electrode (1200×1100 μm^2). (b) Side view showing critical gaps for electrostatic actuation and pull-in prevention……………….……………………44

Figure 3.2: Heat sink dimensions………………………………………………………46

Figure 3.3: Electrostatic FEA showing displacement results for micro-relay. V_{ACT} is electrostatic actuation voltage (120 V) applied on the pull-in electrodes to cause cantilevers to travel 7 µm, before stopped by the stand-off tip. Simulated contact force and actuation time are 1.1 mN/contact region and 9.4 ms, respectively, for an increased voltage of 150 V……………………………………………………………………………...49

Figure 3.4: Preliminary estimation of total series contact resistance with for use in the thermal model. Experimental plot showing the change of contact resistance with increasing force supplied from a force gauge on a Pt-Rh contact cantilever. The force was supplied in 200 µN increments, up to 2.2 mN total force (to obtain 1.1 mN force equally per contact area). The data is compared with Holm's contact model. For 2.2 mN, the experimentally estimated contact resistance was 0.8 Ω whereas Holm's model predicted 0.62 Ω……………………………………………………………………………...50

Figure 3.5: Particle image velocimetry experiment showing the smoke displacement every frame (33 ms) ……………………………………………………………………51

Figure 3.6: Air flow rate as a result of a twelve-run test. The test was done in air, at atmospheric pressure and room temperature……………………………………………52

Figure 3.7: Smoke flow near the heat sink fins on micro-relay. Mini-fan (Sunon UF3A3) was placed 1 mm away from the switch and smoke was fed horizontally from the right side through a glass capillary of 100 µm diameter. Air flow velocity of 0.22 m/s was extracted from recorded images……………………………………………………52

Figure 3.8: FEA results at 1 s into the on-state time with 0.22 m/s upward air flow. Temperature distribution results for (a) unforced (b) forced cooling (Pt-Rh contact cantilever, 0.8 Ω estimated total series contact resistance, 2.5 A line current, 300 K ambient temperature). Compared to unforced cooling, forced cooling suppresses temperature at contact region by around 25 K……………………………………………53

Figure 3.9: Contact cantilever SEM image showing machined recess for contact gap ……………………………………………………………………………………………54

Figure 3.10: SEM image of the actuation cantilever standing upside down……………55

Figure 3.11: SEM image of the heat sink………………………………………………...55

Figure 3.12: SEM micrographs of assembly sequence for all-metal micro-relays showing: (a) floating anchor with alignment posts inserted. (b) Contact cantilever (Pt-Rh or SS316L) aligned on top of the posts through perforations and anchored with thermally conductive epoxy. Contact gap of 2 µm is shown. (c) Actuation cantilever directly placed on PCB substrate. Stand-off tip prevents electrostatic pull-in. (d) Microsphere inserted into the hole-2, secured with thermally conductive epoxy. (e) Heat sink placed by aligning the center hole around the microsphere, fixed with epoxy……………………………………..57

Figure 3.13: (a) Circuitry for device testing, using actuation voltage (V_G) and line current (I_{ON}) inputs. (b) Actuation concept showing V_{S-OFF} and V_{S-ON} conditions. V_{FLOAT} is always near 0, whereas V_{ISO} is equal to V_G……………………..……………………..59

Figure 3.14: Switching sequence showing the hysteresis. Vertical displacement at the tip of the actuation cantilever was recorded using a laser displacement sensor with 0V–170V–0V actuation voltage sweep. Device pull-in and turn-off voltages were 130 V and 60 V respectively. The combined stiffness of pair of cantilevers, heat sink and the microsphere, extracted from these measurements, was 70.8 N/m………………………60

Figure 3.15: Experimental results showing change of on-state resistance with actuation voltage. Line current I_{ON} was kept constant at 1 A. Increase of V_G yielded higher contact force on signal line hence lower on-state resistance. Pt-Rh devices accommodated lower on-state resistance……………………..…………………………………………………62

Figure 3.16: On-state resistance derived from I-V curve. R_{ON} is shown for a contact line current up to 2.6 A (in 50.7 KPa nitrogen, unforced cooling). Actuation voltage V_G was maintained constant at 150 V. Resistances augmented sharply past 1.2 A and 1.5 A of I_{ON} for SS316L and Pt-Rh contacts respectively due to softening at contact asperities. Microwelding failures due to localized heating occurred at 1.8 A and 2.6 A for SS316L and Pt-Rh devices, respectively……………………..……………...……………………62

Figure 3.17: Contact temperature for the Pt-Rh micro-relays subjected to unforced and forced cooling in vacuum nitrogen (50.7 KPa) after 1 s on-state operation at varying current levels. Experimental data was compared with simulations. Device failure due to microwelding occurred at 2.6 A and 2.8 A for unforced and forced cooling respectively. Heat management with upward forced cooling (compatible with Sunon UF3A3 mini fan, 10x10x3 mm^3 size, 0.22 m/s air flow) yielded lowest temperature……………..………63

Figure 3.18: SEM micrographs of failed contact cantilevers after disassembly (view from below). Excessive local heating due to high current yielded metal transfer of PCB material on (a) stainless steel and (b) Pt-Rh contacts at 1.8 A and 2.6 A of line current, respectively, and in 50.7 KPa vacuum nitrogen. Energy dispersive X-ray spectroscopy (EDX) was performed on contact cantilevers after 50 operation cycles at 1 A current. The regions of interest for averaged EDX spectroscopy were 75 x 150 μm^2 and enclosed the particles shown on SEM micrographs (c)-(d). EDX spectra for (e) stainless steel and (f) Pt-Rh contacts showed presence of gold……………………..…………………………..64

Figure 3.19: Lifetime characterization of the micro-relay. Hot switching test was run in nitrogen (50.7 KPa) with 1 A line current and 160 V actuation voltage. The frequency was 0.5 Hz and duty cycle was 50%. A drastic change in on-state resistance was observed past 1900 cycles leading to failure in the 2226th cycle. The corresponding contact temperatures are also shown. At device failure the contact temperature recorded was 443 K…………..65

Figure 4.1: Exploded view of the three-terminal micro-relay. Four regions of the PCB are shown. Cantilever and ground spacers, both from stainless steel, are placed to elevate the cantilever above the signal line to define the actuation and the contact gaps. Gold posts align and hold the spacers and the cantilever over the gold-coated copper traces on the PCB. Cantilever pushes the Pt-Rh contact bridge, located at the distal end, via a micro-rod which couples both components. An Al heat sink is integrated atop the point of contact. Device footprint (as defined by the footprint of the cantilever) is 6.4 mm^2...70

Figure 4.2: Electrostatic FEA for RF micro-relay. (a) Tip displacement was 12 µm as a result of 85 V pull-in voltage. (b) Von Mises stress distribution after the contact. All four contact points had the same stress. Simulated total contact force and actuation time were 1.44 mN (evenly distributed over four contact regions) and 16 ms for 130 V actuation voltage, respectively……………………..……………………………………73

Figure 4.3: Preliminary contact resistance (R_C) estimate for use in the thermal model and in HFSS. Experimental plot showing the change of contact resistance with an increasing force supplied from a force gauge. The force was supplied in 80 µN increments, up to 1.44 mN, distributed evenly on four contacts. The data compared with Holm's contact model. At 1.44 mN total contact force, the experimentally estimated contact resistance was 1.34 Ω whereas Holm's model predicted 1.09 Ω……………………..……………75

Figure 4.4: Electric field distribution at 10 GHz for three configurations in (a-c) the down-state and in (d-f) the up-state. (a,d) In Configuration-1, the DC ground electrode had no plated vias. (b,e) In Configuration-2, the DC ground electrode had plated vias shunted to RF ground. In addition, the corners of the electrodes were rounded and the contact pad for the pull-in was flipped away from the transmission line. (c,f) In Configuration-3, the L-shaped electrode was placed next to the pull-in electrode and shunted to the RF ground through plated vias. A 1 pF DC-blocking capacitor was assumed. The transmission line was designed to have smooth variation of width. In addition, it had fork-shaped open ends to reduce the capacitance with the contact bridge and the dissipation through it. Configuration-3 provided an electric field distribution with minimized coupling to DC ground and pull-in electrode…………………………..77

Figure 4.5: Full-wave HFSS simulation results showing S-parameters for three-configurations. (a) In the down-state, Configuration-3 provides the best insertion loss and return loss at higher frequencies. (b) In the up-state, Configuration-3 presents return loss better than -0.4 dB at 10 GHz. The isolation is also better than the other configurations by about 4 dB over the bandwidth……………………..……………....…78

Figure 4.6: Multiphysics electrothermal FEA results for 1 s into the on-state. The HFSS high power electric field distribution was imported to ANSYS as a boundary condition for joule heating. Contact area temperature distribution for (a) unforced (b) forced cooling (3 GHz, 30 W incident RF power, 1.34 Ω modeled contact resistance, 300 K ambient temperature, 0.22 m/s upward flow) ……………………..……………......…79

Figure 4.7: Assembly sequence for the RF micro-relay: (a) alignment posts inserted. (b) Cantilever and ground spacers (SS304) aligned on top of the posts through the perforations and anchored with electrically conductive epoxy. (c) The cantilever and the heat sink placed on top. Interelectrode gap of 10 μm and stacked PCB-spacer-cantilever structure are shown in the inset. (d) The contact bridge placed on the signal line and coupled with the cantilever through an embedded micro-rod fixed with epoxy in the mid-section of the heat sink, ensuring uniform contact when actuated. Contact gap is shown in the inset………...82

Figure 4.8: (a) Circuitry for testing of three-terminal RF micro-relay. Actuation voltage, V_G was used for the electrostatic actuation. V_{ISO} was monitored to detect any leakage with a 1 MΩ resistor, R_{ISO}, and was always equal to V_G. R_{ON} was the on-state resistance and included the contact resistance, the bridge resistance and the parasitics. A 1 pF surface mount capacitor was used for DC blocking. RF input and outputs were realized via SMA coaxial connectors. (b) High power RF test setup (limited to 45 dBm, 30 W of maximum RF power at 3 GHz) ……………………..……………...……………………84

Figure 4.9: Experimental results for micro-relay showing the change of on-state resistance with actuation voltage after a four probe DC I-V test. Pull-in occurred at 90 V. Further increase of V_G yielded higher contact force on signal line hence lower on-state resistance. Contact resistance was approximately 1.8 Ω and did not vary significantly past 130 V……………………..………………………………………………........…85

Figure 4.10: Switching hysteresis. Vertical displacement at the tip of the cantilever was recorded using a laser displacement sensor with 0V–150V–0V actuation voltage sweep. Device pull-in and turn-off voltages were 90 V and 62 V, respectively. Device stiffness of 159 N/m was extracted……………………..……………..…86

Figure 4.11: (a) Equivalent circuit for the switch in the down-state. An actuation voltage of 130 V was maintained. Characteristic impedance of the contact bridge was 64 Ω. (b) Down-state small-signal analysis for 500 MHz–10 GHz. Experimental data compared with HFSS. The down-state insertion loss was below -0.2 dB for up to 5 GHz………...86

Figure 4.12: (a) Equivalent circuit for the switch in the up-state. Up-state capacitance of 110 fF was extracted from the full-wave simulations. (b) Up-state small-signal analysis for 500 MHz–10 GHz. Experimental data compared with HFSS. The isolation was better than -25 dB up to 5 GHz……………………..…………………………..……...…87

Figure 4.13: High power testing for the RF micro-relay. Tests were realized at 3 GHz and up to 30 W of RF power (test setup limit), at 130 V actuation voltage and in air ambient. Heat management was used throughout the testing with upward forced cooling (compatible with Sunon UF3A3 mini fan, 10x10x3 mm^3 size, 0.22 m/s air flow). (a) Testing with 1 s on-state times. Insertion loss in the down-state was below -0.25 dB for up to 10 W and decayed down pass -0.4 dB at around 18.5 W where the device failure occurred due to microwelding. The up-state isolation was around -26 dB throughout and self-actuation was not observed. (b) Testing with 20 s on-state times. The down-state

insertion loss decayed significantly faster down to approximately -0.4 dB at 7 W where microwelding occurred. The up-state isolation was around -26 dB up to 30 W and no failures were observed……………………..…………………………..…………..…89

Figure 4.14: Average contact temperature for 1 s and 20 s on-state times in air ambient with the forced cooling. Contact temperatures were measured using an infrared thermometer. Experimental data was compared with the thermal model. The device with 1 s and 20 s on-state times failed at 18.5 W and 7 W, respectively……………………...90

Figure 4.15: Lifetime characterization of the micro-relay. The test was run under the hot switching conditions in air ambient with forced air cooling. Test conditions included 1 W of RF power at 3 GHz and 130 V actuation voltage. The switching frequency was 0.5 Hz and duty cycle was 50%. A drastic increase in the down-state insertion loss was observed past 2800 cycles leading to failure in the 3074th cycle at nearly -1 dB. Isolation was reduced slightly to -22.5 dB at the point of failure…………………….………………....91

Figure 5.1: Exploded view of the 4×1 array batch micro-relays. Individual Pt-Rh contact bridges are placed on a Parylene coated steel cantilever frame which carries four cantilevers. Gold posts align and hold the cantilever frame on a multi-layer PCB……..95

Figure 5.2: Exploded view of the single packaged micro-relay. Pt-Rh contact bridge is placed at the tip of the Parylene coated steel cantilever. The assembly is then mounted on a three-layer PCB. An LCP based lid completes the package. Device footprint (as defined by the footprint of the cantilever) is 8.4 mm^2. A–A' cross section is shown in Figure 5.4…………………..………………...…………………….………………...96

Figure 5.3: Dimensions for the cantilever and the contact bridge………………………96

Figure 5.4: A–A' cross section as noted in Figure 5.2. PCB substrate is neglected. The actuation gap is 7 µm as a result of 4 µm of machined recess and 3 µm Parylene thickness. The contact gap is defined by the Parylene thickness alone and is 3 µm.……97

Figure 5.5: DC and RF lines shown in separation from the PCB substrate. All the vias are plated with Cu/Ni/Au traces. Through vias connect the top layer to the bottom layer whereas blind vias connect the top layer to the layer-2…………………..…………...98

Figure 5.6: Package lid dimensions. Wavy epoxy preform allows gas intake…………99

Figure 5.7: Assembled, singulated and packaged micro-relay. The package lid is shown in transparent…………………..………………...…………………….……………..99

Figure 5.8: Electrostatic FEA for the micro-relay. (a) Tip displacement was 3 µm for 72 V pull-in voltage. (b)Post-contact stress distribution. All four contact points had the same stress. Simulated total contact force was 2.2 mN (evenly distributed over four contact regions) for an increased actuation voltage of 100 V………………………..……101

Figure 5.9: Geometric configurations for the thru transmission lines used in RF optimization study……………………..…………………...………………………..……….103

Figure 5.10: Full-wave HFSS simulation results showing S_{11} for five configurations. The cantilever and the contact bridge were discarded in simulations. Configuration-5 provides the smallest reflection with nearly -28 dB at 10 GHz……………………..….104

Figure 5.11: Assembly sequence for the batch RF micro-relay. (a) Individual components are shown. (b) Cantilever frames deposited with Parylene and assembled with contact bridges. (c) Cantilever frame-PCB assembly. (d) Packaged single devices……………………..…………………...……………………..……………......107

Figure 5.12: (a) Testing circuitry for batch fabricated RF micro-relay. Actuation voltage, V_G was used for the electrostatic actuation. V_{ISO} was monitored to detect any leakage with a 1 MΩ resistor. On-state resistance R_{ON} included the contact resistance, the bridge resistance and the parasitics. A 10 pF surface mount capacitor was used for DC blocking. (b) High power RF test setup (limited to 30 W at 3 GHz) ……………………..…………………...……………………..……………...………..109

Figure 5.13: Displacement hysteresis for the micro-relay. Actuation voltage was swept 0V–120V–0V. Device pull-in and turn-off voltages were 78 V and 40 V respectively. Combined stiffness of Parylene coated cantilever and the contact bridge was 125 N/m……………………..…………………...……………………..……………...…..110

Figure 5.14: Experimental results showing the change of total series on-state resistance with increasing actuation voltage. Test was run on packaged devices with nitrogen at atmospheric pressure. Pull-in occurred at 78 V. Further increase of actuation voltage resulted in a lower resistance due to larger contact forces. On-state resistance saturated past 115 V and was approximately 1.1 Ω……………………..……………….............110

Figure 5.15: Small-signal analysis for the unpackaged micro-relay in air ambient at atmospheric pressure. Experimental data compared with HFSS. (a) In the down-state, the insertion loss was better than -0.2 dB for up to 5 GHz. (b) Up-state isolation was better than -18 dB up at 5 GHz……………………..…………………...………………………....112

Figure 5.16: Small-signal analysis for the packaged micro-relay in nitrogen at atmospheric pressure. Experimental data compared with HFSS. (a) Down-state insertion loss was better than -0.25 dB at 5 GHz. (b) In the up-state, isolation was better than -15 dB for up to 5 GHz……………………..…………………...……………………..……...113

Figure 5.17: Small-signal analysis for another packaged micro-relay to show consistency among fabricated devices. Experimental result and HFSS data for the device (a) in the down-state and (b) in the up-state……..…………………...……………………..……...114

Figure 5.18: High power handling test for the packaged RF micro-relay (nitrogen in atmospheric pressure). Tests were performed at 3 GHz and up to 30 W of RF power (test setup limit), at 120 V actuation voltage, and 1 s on-state time. Insertion loss in the down-state was below -0.2 dB for up to 5 W and decayed down to -0.9 dB at 20 W where the device failed due to microwelding. The up-state isolation was approximately -21 dB over the 12 gain steps and self-actuation was not observed……………………..…………..115

Figure 5.19: Output power estimated from the input power, down-state small-signal S_{11} and down-state high power S_{21}. Output power exhibited a relatively linear relationship with the input power up to approximately 13 W, beyond which the linearity was distorted due to dominant effect of down-state S_{21} which degrades significantly at the point of failure at 20 W…………………..………………...……………………..…………..116

Figure 5.20: Hot switching lifetime characterization of packaged micro-relays operating in nitrogen at atmospheric pressure. Actuation voltage was set for 120 V. (a) Test with 1 W continuous RF power supplied at 3 GHz. Switching frequency was 0.5 Hz with 1s on and off-times. The device failed after 10,913 cycles in the down-state. (b) Test with 10 W continuous RF power at 3 GHz. Switching frequency was 0.2 Hz with 0.1s on and 4.9s off-times. The device failed after 8,414 cycles in the down-state. For both cases, insertion loss was below -0.8 dB at the point of failure whereas isolation remained within ± 3 dB of -21 dB and self-actuation was not observed……………………………………………...119

Figure 5.21: Device packages were observed under optical microscope after testing for any deformation or crack formation in the cured epoxy as a possible reason for high pressure He bombing. No such formations were observed for any of the nine packages………………………………………………………………………….....120

Figure 6.1: (a) Potential energy (Si) and (b) reaction force plots (Si and Ni) for a typical bi-stable element…………………..…………..……………………..………………129

Figure A.1: Schematic of the existing design. (a) Top view, (b) side view…………..132

Figure A.2: A spring restrained parallel plate capacitor…………………..……...…133

Figure A.3: Various parts of the beam…………………..…………..………………134

Figure A.4: Model used for beam FEM showing (a) actuation and contact gaps (b) Dirichlet boundary value problem with recoil force…………………..……………..136

Figure A.5: Variation of pull-in voltage with different actuation and contact gaps…..136

Figure A.6: Result of structural optimization problem. (a) Shape-1, $\Lambda_1 \neq 0$ and $\Lambda_2 \neq 0$, (b) Shape-2 $\Lambda_1 = 0$ and $\Lambda_2 \neq 0$…………………..…………..……………………..139

Figure A.7: Generic shape of the optimized structure. (a) Side view, (b) top view…...140

Figure A.8: Modeled pull-in voltages for six configurations..............................141

Figure A.9: Exploded view of the test structure for Configuration-2. Gold posts align and hold the cantilever over gold-coated copper traces on the PCB. The cantilever has two recessed regions with depths 6 µm and 4 µm over the ground electrode and contact pad, respectively (shown upside down in the inset) 142

Figure A.10: SEM micrographs for Configuration-2 test structure. (a) Cantilever is shown upside down with recessed regions. (b) Assembled structure with 6 µm gap between the cantilever and the ground electrode shown in the inset...144

Figure A.11: (a) Circuitry for testing, using variable gate actuation voltage (V_G), and constant drain voltage V_D as the input. R_{ON} was the on-state resistance, and was combination of contact resistance and all the parasitic resistances. (b) Actuation concept showing $V_{OUT-OFF}$ and V_{OUT-ON} conditions..145

Figure A.12: Experimental result showing change of V_{OUT} with the actuation voltage. V_{OUT} was zero until pull-in occurred at 40.95 V. Beyond this point, V_{OUT} remained constant at approximately 1 V...146

Figure A.13: Experimentally found pull-in voltage compared to model for all six configurations...146

LIST OF TABLES

Table 1.1: Performance comparison of FETs, PIN Diodes and RF MEMS electrostatic switches……………………..……………………...……………………..…..………...8

Table 2.1: Cross-technology comparison of various semiconductor switches…………41

Table 2.2: In-technology comparison of various RF MEMS switches………………….41

Table 3.1: Device performance summary. Fabricated devices provide small footprint and high current handling. …………………….……………………..............................68

Table 5.1: Via dimensions and configurations for the thru line optimization…………102

Table 5.2: Package test results for nine packages tested for helium detection immediately after bombing, 30 minutes after bombing and 60 minutes after bombing……………...120

Table A.1: Critical lengths for the optimized design……………………..……………140

Table A.2: Slope and width values for different configurations……………………….141

Table A.3: Summary of pull-in and turn-off voltages and associated actuation and recoil force estimates for all six configurations……………..……………..……………..…...146

ABSTRACT

This work explores the potential of bulk foil metal alloys on micromachined relays for high power DC and RF applications. Platinum-rhodium (Pt-Rh) is of particular interest because it is both chemically inert and mechanically robust. The contributions include the investigation of design and manufacturing options, addressing issues such as the geometry of electrostatically actuated cantilevers, the integration of heat sinks, the integration of encapsulation, batch mode fabrication, and other aspects.

In one part of the investigation, DC micro-relay test structures using Pt-Rh contacts were benchmarked against the ones using stainless steel (SS316L) contacts. Devices with 6.5 mm^2 footprint were directly assembled on the printed circuit boards (PCB). Devices also included microfabricated on-device heat sinks subjected to a heat management using forced cooling to dissipate contact heat. Fabricated micro-relays exhibited 1.5 Ω and 1.25 Ω on-state resistances for SS316L and Pt-Rh contacts, respectively. In hot switching high power tests, Pt-Rh and SS316L micro-relays operated up to 1.8 A and 2.6 A, respectively.

In another part of the investigation, RF micro-relays with Pt-Rh contacts were designed and fabricated. Test structures with 6.4 mm^2 footprint had 90 V pull-in voltage. The micro-relays had down-state insertion loss and up-state isolation better than-0.2 dB and -25 dB up to 5 GHz, respectively. Unpackaged micro-relays exhibited RF power handling up to 18.5 W hot switching in ambient air.

The third part of this investigation was directed at batch mode manufacturing and packaging of micro-relays directly on PCB substrates. For this, 4×1 device arrays were designed, fabricated, and encapsulated. Subsurface metal layers on the PCB were used to transfer the signal into and out of the sealed encapsulation. The footprint of packaged test structures was 8.4 mm^2. The contact resistance and the pull-in voltage for the fabricated devices were 78 V and 1.1 Ω for an actuation voltage of 115 V, respectively. The packaged devices operated in atmospheric pressure nitrogen and exhibited down-state insertion loss and up-state isolation better than -0.25 dB, and -15 dB, respectively for up to 5 GHz. Packaged devices operated up to 20 W hot switching RF power.

CHAPTER 1

INTRODUCTION

The uses of micro-relays range from common DC applications in industrial machinery and automotive control circuits to high frequency signal switching applications such as in the aerospace sector, radio frequency (RF) communications and portable electronics [Jac06, Li00, Liu0, Luc04, Boz00]. Minimization of weight, size and production cost of a relay is of primary interest to enable use in larger switching networks. Recently, the developments in microelectromechanical systems (MEMS) have made the fabrication of micro-relays possible. Consequently, the miniaturization and the integration of relays for DC and RF applications has been the topic of extensive research [Alm07, Reb03, Lar91, Mih01a]. Any effort towards the micro-relays benefits from the distinction of different types of switching devices along with the physical properties.

This chapter introduces the micro-relays for DC and RF MEMS applications. Section 1.1 describes the types of micro-relays and Section 1.2 provides a brief introduction to performance measures of MEMS switches. Section 1.3 introduces contact resistance and material considerations for ohmic-contact micro-relays. Section 1.4 and Section 1.5 present the background and the motivation for the applications targeted in this dissertation: micro electro-discharge machined bulk Pt-Rh switches and hybrid assembly and packaging on the printed circuit boards, respectively. Section 1.6 provides the goals and approach for this work whereas Section 1.7 outlines the thesis.

1.1. Types of micro-relays

1.1.1. DC micro-relays

MEMS switches can be investigated in several categories. A possible classification is according to the switching signal type. DC switches simply break an electrical circuit, interrupting the current or diverting it from one conductor to another. Thyristors are considered as conventional high power DC switches. A thyristor is a bi-stable solid state relay composed of a four layer stacking of alternating n and p-type material. Electrical conduction occurs when the gate receives a current pulse, and continues for as long as the device is forward biased [Chr04].

There are distinct types of thyristors such as silicon controlled rectifier, phase-controlled thyristors, gate-turn-off thyristors, bi-directional triode thyristors and reverse-conducting thyristors and so on. The distinction stems from the reconfigurations of ports and cascade of multiple devices. Traditionally, thyristors are used in lower switching frequencies up to 60 Hz except for fast switching thyristors that enables kHz range switching frequency. Turn off-times of thyristors range between 5-100 μs and on-state (when the switch is on) voltage drop is around 1.2-2 V for 1000 V, 100 A ratings. Power ratings for thyristors can go up to 2500 V and 2000 A. While they can be a good candidate for high power DC applications, the bulk structures and slow responses impede the use in microsystems or in applications which requires a dense, large network of switches. There exist several studies on DC micro-relays [Woo98, Lee02, Sch96, Li00, Xu06]. Most of the micro-relyas employ electrostatic attraction principle, later described in full detail in this chapter.

Scanning electron microscope (SEM) images of a few electrostatically actuated lateral switch configurations are shown in Figure 1.1 [Li00]. These devices were bulk micromachined with a combination of wafer bonding and deep reactive ion etching resulting in a maximum aspect ratio of 20:1. Typical contact resistance of the micro-relay was measured 1 Ω with an actuation voltage of 20 V and stand-off voltage of 300 V. It should be noted that none of the DC micro-relays reported any power handling capability. The maximum switched current was 80 mA.

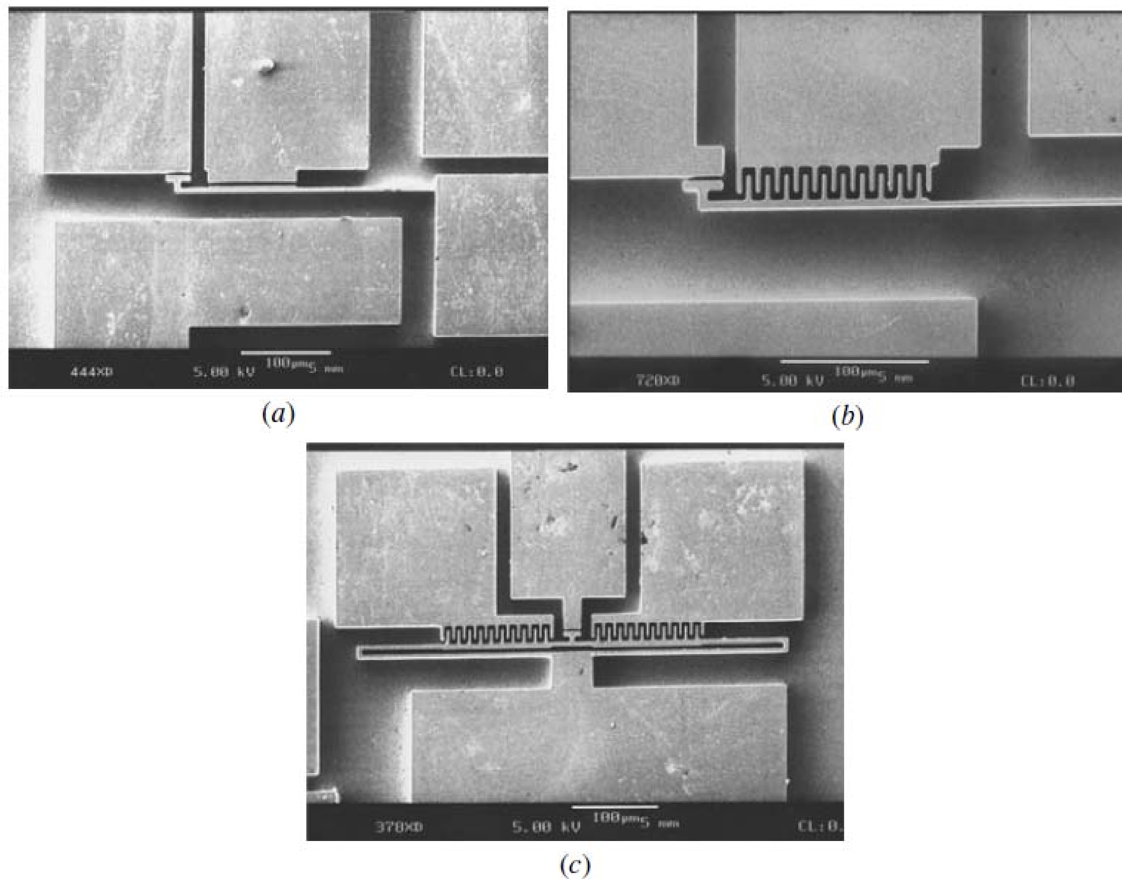

Figure 1.1: The SEM photographs of the micro-relays with different structures (a) A micro-relay with plate electrodes, (b) a micro-relay with a single beam and a single comb drive, (c) a micro-relay with a double-fold beam and a pair of comb drives [Li00]

Apart from the thyristors and DC micro-relays switches, there are many switching devices such as metal–oxide–semiconductor field-effect transistor (MOSFET), bipolar

junction transistor (BJT) and insulated gate bipolar transistor (IGBT). Power MOSFETs, IGBTs and silicon-carbide BJTs exhibit good characteristics in higher power switching [Zit99, Mit00, Aga02]. In addition, Positive-Intrinsic-Negative (PIN) diodes and FETs have been used as RF switches however, RF characteristics are inferior compared to RF MEMS switches, as will be discussed in the next section.

1.1.2. RF micro-relays

While non-MEMS technologies are now established within the high volume range of commercial markets, MEMS switches are approaching commercial success as well. Especially since Hughes Research Lab's success in making a microwave switch in 1990, RF MEMS devices have been researched, and are on the verge of wide commercialization [Lar91]. The first RF MEMS papers started to appear three decades ago, with electrostatically actuated cantilever-type switches [Pet79]. However, even though RF MEMS technology can still be considered immature, a number of interesting components and circuits have been demonstrated over the past decade [Rob01, Luc04, Reb01].

Switches are considered the most important RF MEMS components. MEMS switches are devices that use mechanical movement to achieve a short circuit or an open circuit in the RF transmission line. RF MEMS switches are the specific micromechanical devices that are designed to operate at RF-to-millimeter-wave frequencies (0.1 to 100GHz).

The importance of RF MEMS switch can be correlated to the implementation potential of very high performance and digitally-controlled components such as R, L and

C lumped-elements, circuits (e.g. reconfigurable networks, attenuators, phase shifters, and antennas) and subsystems such as antenna arrays and signal routing [Luc04, Reb01, San04].

The forces required for the mechanical movement can be obtained using electrostatic, magnetostatic, piezoelectric, or electrothermal actuation principle [Reb01]. To date, mostly electrostatic-type switches have demonstrated functionality at 0.1-100 GHz whereas other design and actuation principles provide distinct benefits in various other ways as will be discussed in later sections.

The common microwave switches currently employed in the microwave industry are mechanical switches (coaxial and waveguide) and semiconductor switches (PIN diode and FET). Mechanical coaxial and waveguide switches present the benefits of low insertion loss, large off-state (when the switch is off) isolation, high power handling capabilities, and are highly linear in essence. However, they are often bulky, heavy and slow. On the other hand, PIN diodes and FET switches offer much faster switching speeds and are smaller in size and weight, but are inferior to the mechanical counterparts in insertion loss, DC power consumption, isolation and power handling. MEMS switches promise to merge the favorable properties of both mechanical and semiconductor switches [Gra04]. The exclusive advantages of RF MEMS switches over conventional PIN diodes or FET switches are [Reb01]:

- **Near-zero power consumption**: Actuation voltages can vary from 3 V to 150 V for different actuation mechanisms but most of the switches (electrostatic) does not consume any current, leading to significantly low power dissipation (10–100 nJ per switching cycle).

- **Very low insertion loss**: RF MEMS switches can offer an insertion loss of 0.1 dB up to 40 GHz for contact resistances as low as 1 mΩ.

- **Very high isolation**: RF MEMS series switches are fabricated with air gaps, and therefore, have very low off-state capacitances (2–4 fF) resulting in exceptional isolation at 0.1–40 GHz range.

- **Low manufacturing cost**: RF MEMS switches are fabricated using surface micromachining techniques and can be built on Pyrex, quartz, low-temperature co-fired ceramic (LTCC), mechanical-grade high-resistivity silicon, or GaAs substrates.

However, RF MEMS switches also suffer from some problems [Reb01], such as:

- **Power handling**: Most RF MEMS switches cannot handle more than few watts which is required in high-power applications, such as transmitters in satellites and/or earth-based communications stations.

- **High-voltage drive**: Most of the electrostatic RF MEMS switches require 20-150 V to operate, and this necessitates a voltage up-converter chip when used in portable telecommunication systems.

- **Relatively low speed**: The switching speed of most RF MEMS switches is around 2-100 µs. Certain communication and radar systems require much faster switching.

- **Packaging and cost**: RF MEMS switches need to be packaged in hermetic or near-hermetic seals with inert atmospheres containing nitrogen, argon, etc. and in very low

humidity levels. Packaging cost is the major contributor to the overall switch cost which is often much higher than for PIN diodes and FET switches.

- **Reliability**: The majority of the reliability issues for RF MEMS switches are due to the inability of handling high power. The reliability of mature RF MEMS switches that operate in low power is usually 0.1-10 billion cycles. However, many systems require switches with much higher cycles (20-200 billion). Also, the long-term reliability in years has not yet been addressed. Reliability is usually lower due to a number of failure mechanisms that will be explained in detail later.

Table 1.1 provides a numerical performance comparison between RF MEMS, FET and PIN diodes [Reb03].

1.2. Performance measures of MEMS switches

The performance criteria of MEMS switches rely on several concepts and parameters. This section highlights those concepts and discusses the parameters for different types of switches.

Regardless of actuation mechanism, there are two generic structures for a MEMS switch: (i) ohmic-contact or DC-contact (metal-air-metal); and (ii) capacitive (metal-insulator-metal) [Luc04, Gra04]. The main advantages of the former are that a very low on-state insertion loss and very high off-state isolation can be achieved. The reason for this is that the ohmic-contact area needed for this type of switch can be very small. This area creates a small parasitic capacitance when the electrodes are separated and, hence good isolation can be achieved. Unfortunately, ohmic-contact switches are prone to

corrosion and static friction (stiction). Moreover, significant amount of force is required to create an efficacious metal-to-metal contact and this may not be possible for certain applications where force generation is limited by actuation mechanism.

Table 1.1: Performance comparison of FETs, PIN Diodes and RF MEMS electrostatic switches

Parameter	RF MEMS	PIN	FET
Voltage (V)	20–80	±3–5	3–5
Current (mA)	0	3–20	0
Power handling (W)	<1	<10	<10
Power Consumption (mW)	0.05–0.1	5–100	0.05–0.1
Switching time	1–300 μs	1–100ns	1–100ns
C_{UP} (series) (fF)	1–6	40–80	70–140
R_S (series) (Ω)	0.5–2	2–4	4–6
Capacitance ratio	40–500	10	n/a
Curoff frequency (THz)	20–80	1–4	0.5–2
Isolation (1-10 GHz)	Verh high	High	Medium
Isolation (10-40 GHz)	Very high	Medium	Low
Isolation (60-100 GHz)	High	Medium	None
Loss (1-100 GHz) (dB)	0.05–0.2	0.3–1.2	0.4–2.5

With the capacitive switch, a larger electrode surface area improves the on-state insertion loss; on the other hand compromises the off-state isolation. As a result, the electrode separation needs to be maximized and this may not be feasible in certain cases. The main benefit of the capacitive switch is often the longer lifetime for low power cases. The lifetime of an ohmic-contact switch is typically few orders of magnitude less than that of a capacitive switch. Another advantage of the capacitive membrane switch is that the on-state insertion loss is not fully dependent on the contact force, which eliminates certain design considerations.

Figure 1.2 shows two types of series switches: The orthogonal series switch (Figure 1.2(a) and (b) and the inline series switch (Figure 1.2(c)) [Reb01]. The actuation

of the orthogonal switch occurs in a perpendicular plane to the transmission line, whereas the actuation of the inline switch occurs in the same plane as the transmission line, which provokes the RF signal to pass by the entire inline switch. Figure 1.3 exhibits first practical MEMS capacitive shunt switch developed by Raytheon [Gol96, Gol98]. The switch is based on a fixed-fixed metal (gold or aluminum) beam design. The anchors are grounded to the coplanar-waveguide (CPW) ground plane; a high resistivity silicon substrate upon which a centre line (signal) and two ground lines on the sides are placed.

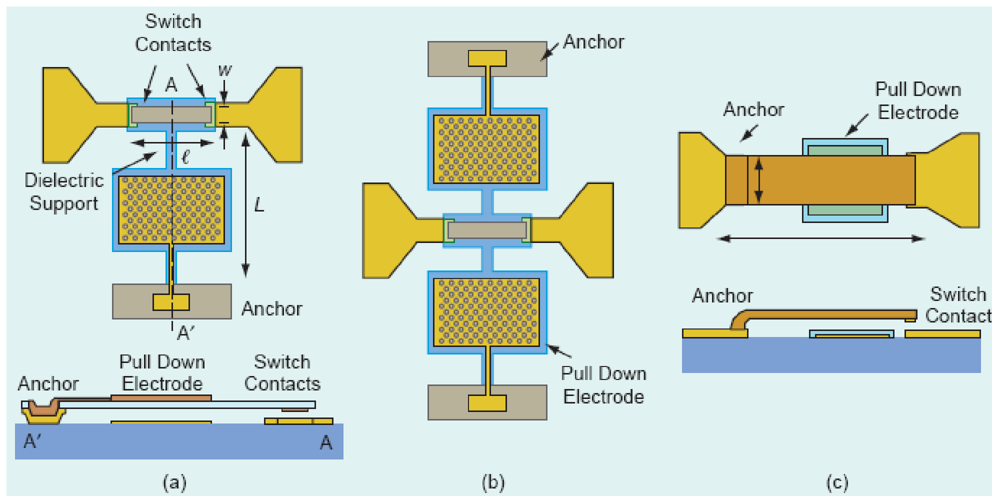

Figure 1.2: Orthogonal MEMS-series switches with (a) one electrode, (b) two electrodes, and (c) inline MEMS-series switches [Reb01]

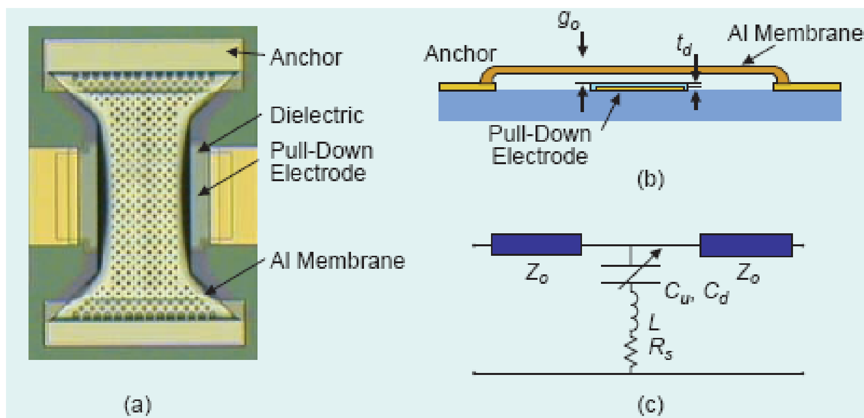

Figure 1.3: Raytheon MEMS capacitive shunt switch: (a) cross-section view and (b) electrical RLC model [Gol96, Gol98]

1.2.1. Figure of merit

The RF performance of a switch can be represented by the following cut-off frequency figure of merit:

$$f_c = \frac{1}{2\pi R_{on} C_{off}} \quad (1.1)$$

where R_{on} is the on-state resistance, which effectively represents the on-state insertion loss, and C_{off} is the off-state capacitance, representing the off-state isolation. Since the on-state resistance and the off-state capacitance have different connotations for series and capacitive switches, it would be meaningful to analyze them separately [Reb03].

The electrical model of a MEMS series switch is a series capacitance in the up-state position and a small resistance in the down-state position. The isolation of a series switch in the up-state position can be expressed in terms of microwave scattering parameters (S-parameters), where in the frequency domain, the reflected signal is denoted S_{11} and the transmitted signal is denoted S_{21}:

$$|S_{21}|^2 = 4\omega^2 C_u^2 Z_0^2 \quad (1.2)$$

where C_u is the up-state capacitance and Z_0 is the transmission line impedance. The insertion loss is defined as:

$$|S_{21}|^2 = 1 - R_s Z_0 \quad (1.3)$$

where R_s denotes the contact resistance of the switch. It is apparent that an up-state capacitance of 2-4 fF and a contact resistance of 1 Ω results in an isolation of 46 to 40 dB at 4 GHz and a 0.1 dB loss up to 40 GHz [Luc04]. This is a notable performance not attained by any solid-state device. The figure of merit cut-off frequency is:

$$f_c = \frac{1}{2\pi R_s C_u} \tag{1.4}$$

The above term is an indication of the low-loss performance of a switch. The cut-off frequency of MEMS series switches is around 30-80 THz, while it is only 1-2 THz for GaAs PIN diodes and 0.2-0.5 THz for FET switches. Goldsmith et al. reported RF MEMS switches with an extracted f_c=2 THz, marking an order of magnitude improvement over that attainable with PIN diodes [Gol95].

For a capacitive type switch, the up-state reflection coefficient is:

$$|S_{11}|^2 = \frac{\omega^2 C_u^2 Z_0^2}{4} \tag{1.5}$$

The down-state isolation is:

$$\begin{cases} \frac{4}{\omega^2 C_d^2 Z_0^2} & for\ f \ll f_0, \\ \frac{4R_s^2}{Z_0^2} & for\ f = f_0, \\ \frac{4\omega^2 L^2}{Z_0^2} & for\ f \gg f_0 \end{cases} \tag{1.6}$$

where C_d is the down-state capacitance, L is the inductance and f_0 is the resonant frequency. The down-state resonant frequency of the capacitive switch becomes:

$$f_c = \frac{1}{2\pi\sqrt{LC_d}} \tag{1.7}$$

Figure 1.4 exhibits the electrical performance of a capacitive switch with exemplary values of C_u = 35 fF and C_d = 2.7 pF, L=8 pH and R_s=0.25 Ω [Mul00].

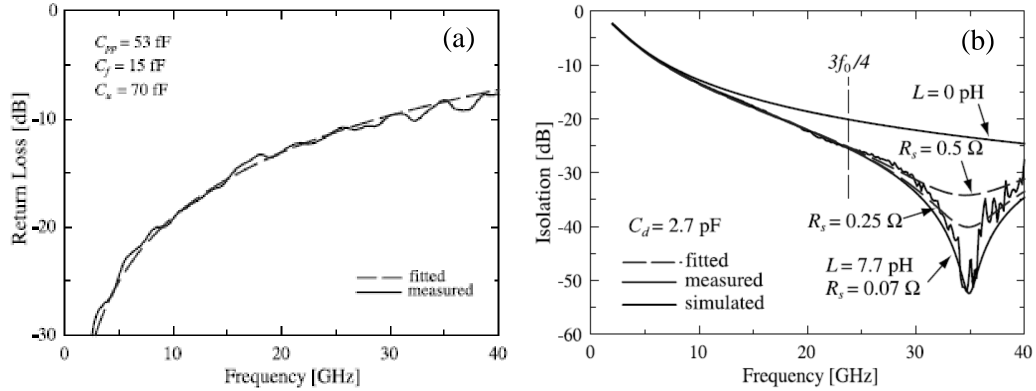

Figure 1.4: S-parameters of a MEMS capacitive shunt switch, (a) up-state position and (b) down-state position [Mul00]

1.2.2. Actuation voltage

The electromechanical modeling of RF MEMS switches relies on the actuation mechanisms which should be individually taken into consideration for different types such as electrostatic, electrothermal, electromagnetic, or piezoelectric [Zha03]. Since the electrostatic actuation is the most popular one and since the devices presented in this thesis employ the electrostatic actuation principle, it is detailed in this section.

Majority of RF MEMS switches are based on an electrostatic out-of-plane actuation principle featuring a fixed-fixed type suspending beam or a cantilever beam which are illustrated in Figure 1.5 [Reb03].

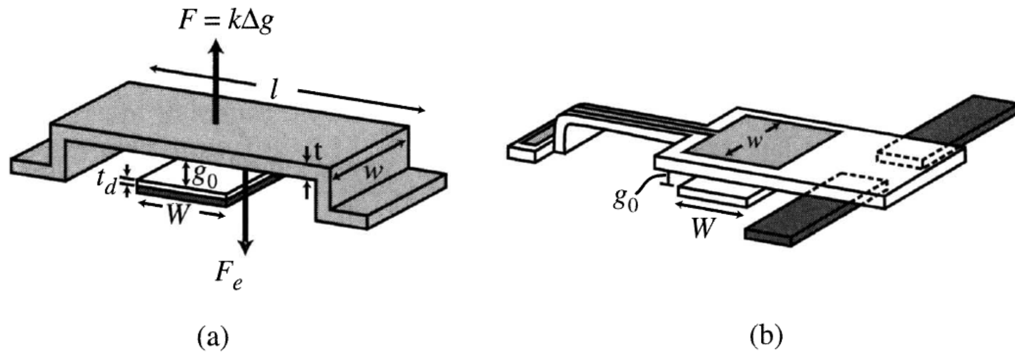

(a) (b)

Figure 1.5: (a) A MEMS fixed-fixed (suspended) beam, (b) cantilever beam [Reb03]

The electrostatic force applied on the actuation beam can be derived by considering the power delivered to a time-dependent capacitance [Zah79]:

$$F_e = \frac{1}{2}V^2\frac{dC(g)}{dg} = -\frac{1}{2}\frac{\varepsilon_0\varepsilon_r WwV^2}{g^2} \tag{1.8}$$

where V is the actuation voltage applied between the actuation beam and the pull-in electrode underneath, and g is the beam height. In the above equation, the effects of the dielectric layer between the actuation beam and pull-in electrode are neglected. Considerations which includes a dielectric layer of around 1000-2000 Å, results in the following capacitance formula:

$$C = \frac{\varepsilon_0\varepsilon_r A}{g+\left(\frac{t_d}{\varepsilon_{dl}}\right)} \tag{1.9}$$

where t_d and ε_{dl} are the thickness and relative dielectric constant of dielectric layer, respectively. The electrostatic force then becomes:

$$F_e = -\frac{1}{2}\frac{\varepsilon\varepsilon_0\varepsilon_r WwV^2}{\left(g+\left(\frac{t_d}{\varepsilon_r}\right)\right)^2} \tag{1.10}$$

$$\varepsilon = \begin{cases} 1 & (g \neq 0) \\ 0.4 - 0.8 & (g = 0) \end{cases}$$

where ε accounts for the reduction of parallel-plate capacitance due to the roughness of metal-dielectric interface. For $g>>t_d$, the above equation is simplified to equation 1.8.

Electrostatic force is assumed to be evenly distributed across the actuation beam section which overlaps with the pull-in electrode. Therefore, the beam spring constant can be used to determine the beam displacement under the applied force. Equating the applied electrostatic force with the mechanical restoring force due to beam stiffness results in:

$$\frac{1}{2}\frac{\varepsilon_0\varepsilon_r WwV^2}{g^2} = k(g_0 - g) \tag{1.11}$$

where g_0 is the initial height of the actuation beam when no bias voltage is applied and k is the beam spring constant. Solving (1.11), the following expression can be obtained:

$$V = \sqrt{\frac{2k}{\varepsilon_0\varepsilon_r Ww} g^2(g_0 - g)} \tag{1.12}$$

The above equation is plotted with respect to the actuation beam height in Figure 1.6 [Reb03]. The figure shows two possible beam positions for any applied voltage. By taking the derivative of (1.12), with respect to the beam height and setting it to zero, the height where the instability occurs is found to be two-thirds of the zero-bias beam height (2/3 g_0). This condition of pull-in, in which top plate collapses onto the bottom electrode suddenly, is satisfied when the electrode separation decreases below two-thirds of the fully open (up-state) condition [Luc04]. The amount of the voltage required to bring the beam to that distance is called the pull-in voltage (V_{pd}). This phenomenon takes place at the point where the electrostatic attractive (downward) force is equal to the linear restoring (upward) spring force and is due to the positive feedback in the electrostatic actuation.

If 2/3 g_0 is replaced with g back in the equation 1.12, the pull-in voltage V_{pi} is found:

$$V_{pi} = V\left(\frac{2g_0}{3}\right) = \sqrt{\frac{8k}{27\varepsilon_0\varepsilon_r Ww} g_0^3} \tag{1.13}$$

It is worth noting that although the beam width w, is expressed in the above equation, the pull-in voltage is independent of the beam width since the spring constant scales with the width and cancels out its overall effect.

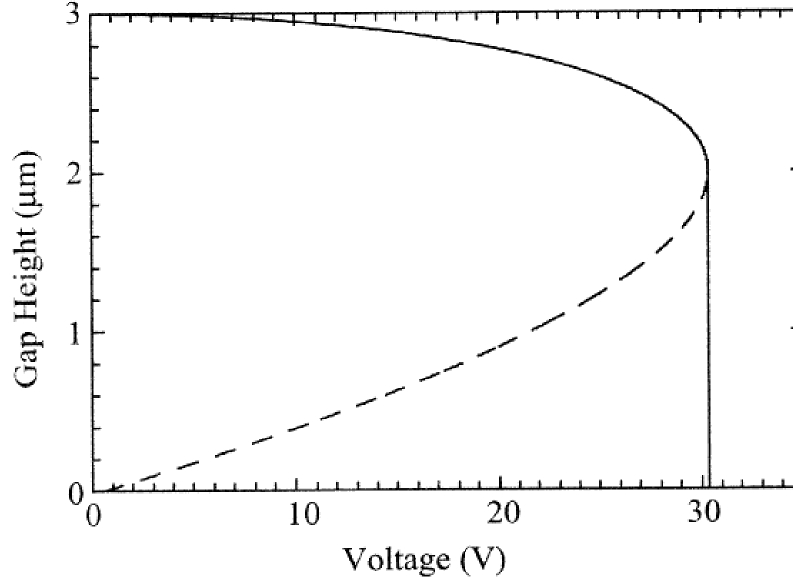

Figure 1.6: The beam height versus the applied voltage for exemplary values of W=w=100 µm, g_0=3 µm and k=10 N/m. The pull-in voltage is 30 V. Dashed line is the unstable portion of the beam height [Reb03]

The applied voltage is typically 1.2×–1.4× V_{pd} for achieving fast switch operation [Reb01]. Once the switch is pulled down the electrostatic voltage can be reduced to a value lower than V_{pd} while still keeping the switch in the down-state position. For the cases where there is a dielectric between the actuation beam and the pull-in electrode, this is done often to reduce both the electric field in the dielectric and to alleviate the possibility of dielectric breakdown or charge injection into the dielectric.

A low actuation voltage is a desirable switch characteristic since it will broaden the range of possible applications especially for portable devices [Cha03]. In recent years, many efforts have been put on to reduce the actuation voltage of the electrostatic switches. Those efforts includes using a variety of beam geometries such as added serpentine beams [Hua01], meanders [Pac00, Per03], and materials to decrease the spring constant of beam [Ke08, Seg07]. Other methods such as decreasing the interelectrode gap i.e. the gap between the beam and the pull-in electrode, increasing the area of

electrostatic field, and the dielectric constant between parallel plates were also explored [Son07].

Goldsmith et al. reported on the lifetime characterization of capacitive RF MEMS switches [Gol01]. They have demonstrated an exponential relationship between lifetime and actuation voltage. According to the study, a reduction in the actuation voltage by 5-6 V results in an order of magnitude increase in the lifetime of typical MEMS switches. Therefore, reducing the actuation voltage can significantly enhance the reliability performance of MEMS switches.

1.2.3. Power handling

High power handling in micro-relays is sought for applications such as in electronic test circuitry, power conversion, satellite transmitters [Jac06, Nor99]. Design challenges for high power micro-relays include finding ways to overcome a number of failure mechanisms such as self-actuation, contact metal softening and microwelding. These failure mechanisms will be explained in greater detail in the next chapter. Contact failure mechanisms that define the power handling capability of the ohmic-contact micro-relays are strongly related to the nature of the contact metals [Jen05, Kwo07]. A detailed section is allocated for high power considerations in MEMS switches in the next chapter.

1.2.4. Switching speed

Slower switching speed is one of the few disadvantages of MEMS relays compared to the semiconductor counterparts [Per03]. While the mass is typically very small (in the order of 10^{-11} to 10^{-9} kg), the inertia exerted due to the mechanical

movement still restricts the speed typically from few microseconds to few milliseconds. One of the fastest switches thus far has been developed by Massachusetts Institute of Technology (MIT) Lincoln Laboratories [Duf01]. The effort resulted in a very compact cantilever switch (less than 50 μm long) with a response time of approximately 1 μs. This comparably low response time is primarily due to its very small dimensions, mass, and limited squeeze-film damping due to air compressed between the actuation electrodes [Lam04, Ste05]. Sub-μs time switching speeds have been proven using RF MEMS switched capacitors (Figure 1.7) and it is mostly due to much smaller dimensions and masses [Lac06, Mer05].

Low-voltage switches are generally expected to be slower since they typically have to drive a relatively large actuation unit area for same voltage. This is particularly true if the switch is expected to operate in air or another gas environment, such as N_2 for limiting the humidity level surrounding the structure. Those effects are taken into consideration in the comprehensive dynamics studies of switching speed [Mul01a, Mul01b]. A common way to improve the switching speed is to form damping holes on the actuation part so as to reduce air damping during switch actuation [Mul00].

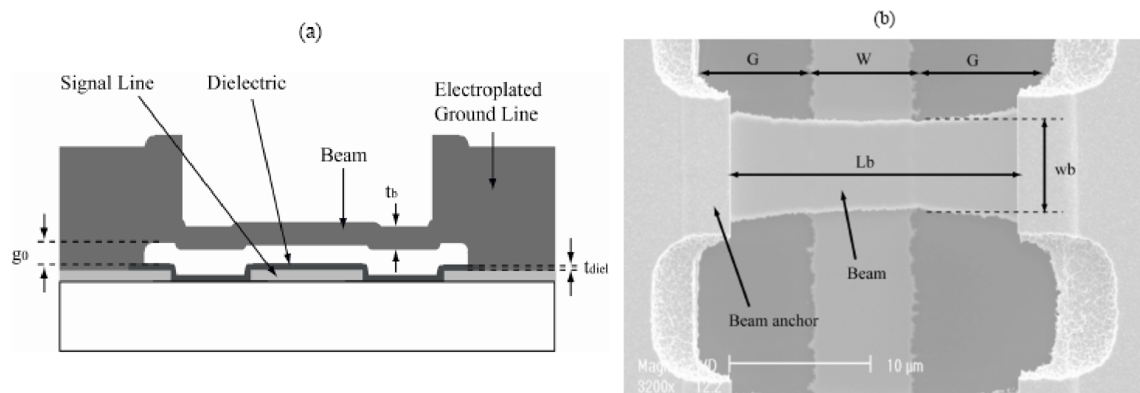

Figure 1.7: (a) Cross section of a miniature switched capacitor, (b) SEM picture a miniature switched capacitor [Lac06]

1.3. Contact resistance and material considerations in ohmic-contact micro-relays

Contact resistance and contact material selection is among the most important design considerations for high power ohmic-contact micro-relays. A material selection which allows low contact resistance is important to reduce the joule heating at the contact points and consequently enable high power handling [Pat05]. A low contact resistance is also essential from RF performance perspective to obtain a low on-state insertion loss [Tan02]. In addition, properties such as the hardness and the melting temperature of the contact material are crucial to achieve high power operation. Contact resistance modeling and contact material selection are detailed in this section.

1.3.1. Theoretical model

Contact resistance modeling requires an accurate surface profiling around the contact area which is usually a microfabricated dimple. A generic contact profile was proposed more than a decade ago [Maj97]. The model consisted of a single point asperity or a group of asperities as shown in Figure 1.8. As two contact surfaces come close during switching, initial interactions take place at the tip of these asperities that extend further than average surface roughness. A relationship between the contact force and the contact radius could then be established for a number of contact asperities by employing a generalized elastic-plastic model for contact of a rough surface on a flat surface build upon Greenwood-Williamson model [Gre66, Cha87]. This model particularly holds true for contact forces up to few hundreds of μN as shown in the figure below.

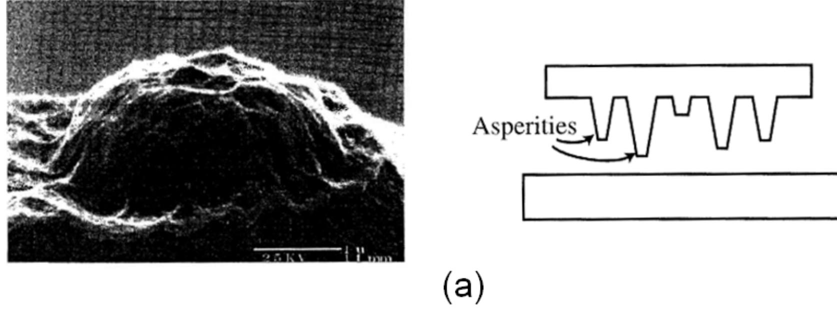

(a)

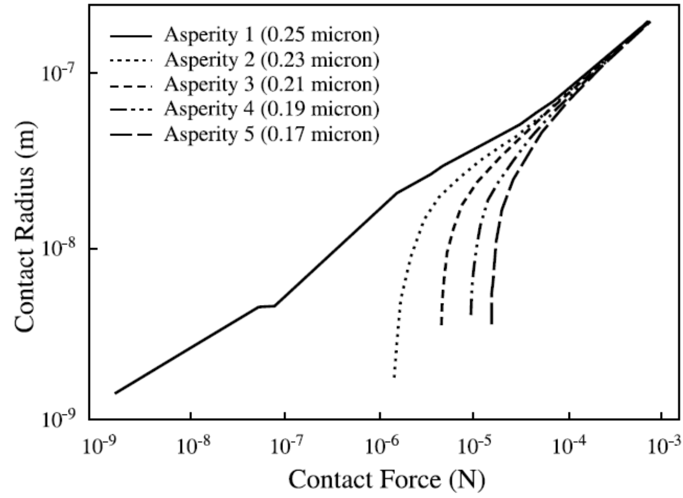

(b)

Figure 1.8: (a) Surface profile of contact having multiple asperities, (b) calculated contact radius versus contact force for a gold contact [Maj97]

For larger contact forces, a purely plastic model can be used [Hol68]. This plastic model follows:

$$F = A_C H n \tag{1.14}$$

where F is the contact force, A_C is the actual mechanical contact area of overlapping contact asperities between touching surfaces, H is the contact metal hardness, and n is an empirical factor which depends on material and approaches 1 for clean surfaces. Incorporating the contact radius into this model gives:

$$\alpha_H = \sqrt{\frac{F}{Hn\pi}} \tag{1.15}$$

where α_H is the radius of Holm's contact spot (α-spot) representing a cluster of multiple small contact spots. Contact radius α_H can be used to estimate the Maxwell spreading resistance between two contacting surfaces assuming that the contact radius is much larger than the electron mean free path length of contacting materials. This spreading resistance is also known as constriction resistance.

$$R_C = \frac{\rho}{2\alpha_H} \tag{1.16}$$

where ρ is the contact metal resistivity. The equations 1.15 and 1.16 show that a larger contact force translates into a larger α-spot and a smaller contact resistance in turn. An important interpretation of the expressions above is that the contact resistance is independent of the nominal contact area and only depends on the hardness of the contact materials.

Studies show that harder metals such as rhodium show much less adherence than gold [Sha74, Sha76]. Comparing gold and rhodium, it is known that rhodium has both 2x higher hardness and resistivity of gold hence resulting with a 4x larger contact resistance for same contact force. On the other hand, gold has around 3.6 times more adhesion coefficient than rhodium, therefore two materials exhibits similar behavior considering plastic deformation characteristics.

Figure 1.9 shows measured contact resistance of gold, $AuNi_5$, and rhodium versus applied force. As seen on the plot, increasing contact force reduces contact resistance for pure gold, $AuNi_5$ alloy and rhodium.

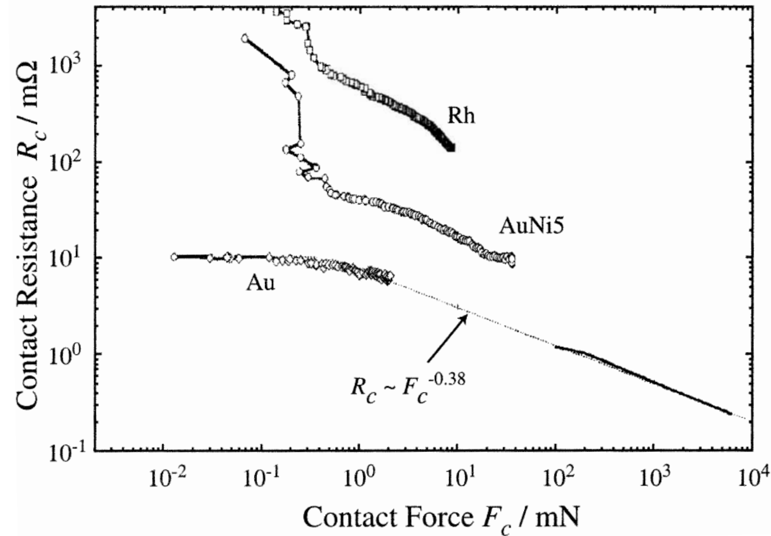

Figure 1.9: Measured contact resistance of Au, $AuNi_5$ and Rh [Sch98]

MEMS switches typically exhibit release forces of 50 μN – 1 mN [Hym99, Sak99, Woo98, Str01]. For switches with large forces (> 1 mN), adherence forces do not have any significance and hard metals can be used.

Large contact forces are desirable not only to reduce the contact resistance but also to penetrate the residual contamination accumulated on the contact surfaces in non-hermetic packages and to extend the device lifetime in turn.

1.3.2. Contact metal selection

The selection of contact metals is an important consideration to enhance power handling capability of ohmic-contact DC and RF micro-relays. Gold-gold contacts provide low resistivity and low corrosion however they have low hardness and low melting point [Cou04, Lee06]. For large contact forces (usually above 1 mN), some amount of contact wear is tolerable. However for smaller contact forces (usually below 1 mN), the metal-to-metal adhesion due to the localized welding of gold contacts is

predominant failure mode because the switch restoring forces are smaller. Gold can also form intermetallic compounds with copper [Cou04]. Poor corrosion resistance eliminates many metals from consideration for contact materials in MEMS switches such as silver and copper because the switch closing forces are not large enough to break through an oxide or sulfide layer on the surface, particularly with the electrostatic actuation.

The ideal micro-relay contact material would have a high melting point and hardness, low resistivity and corrosion, and it would be easily and repeatedly fabricated. For this reason, research into alloys of gold has been conducted to try to find a harder material while maintaining low resistivity [Cou04, Lee06]. The hardness and the electrical resistivity data for several elements and gold alloys are plotted in Figure 1.10 [Lee06]. When gold is alloyed with harder metals, the effective resistivity increases significantly. Compared to platinum-gold alloy (10:90), pure platinum has greater hardness at the same resistivity. Pure ruthenium is a good material for obtaining hardness, but it forms a native oxide on the surface. Pure rhodium, on the other hand, has low corrosion and resistivity with larger hardness but is extremely expensive and so is commonly used as an alloying metal.

1.4. Micro electro-discharge machined bulk foil Pt-Rh relays for high power applications

While significant progress has been made in micromachined relays over the past two decades, available technologies are not authenticated as best for high power handling. As mentioned earlier in the chapter, contact failure mechanisms that define the power handling capability of the ohmic-contact micro-relays are strongly related to the

nature of the contact metals. Most of the past efforts in high power DC and RF micro-relays have focused on surface micromachined contact materials for increased power handling [Cou04, McG06]. Surface micromachining techniques only allow the use of metals that can be sputtered or electroplated. Subtractive bulk micromachining of foils offers a complementary approach. Micro-relays micromachined from bulk foils can utilize metal alloys as contact metals, and take advantage of the properties such as high hardness and high melting point, and thereby accommodate high DC and RF power.

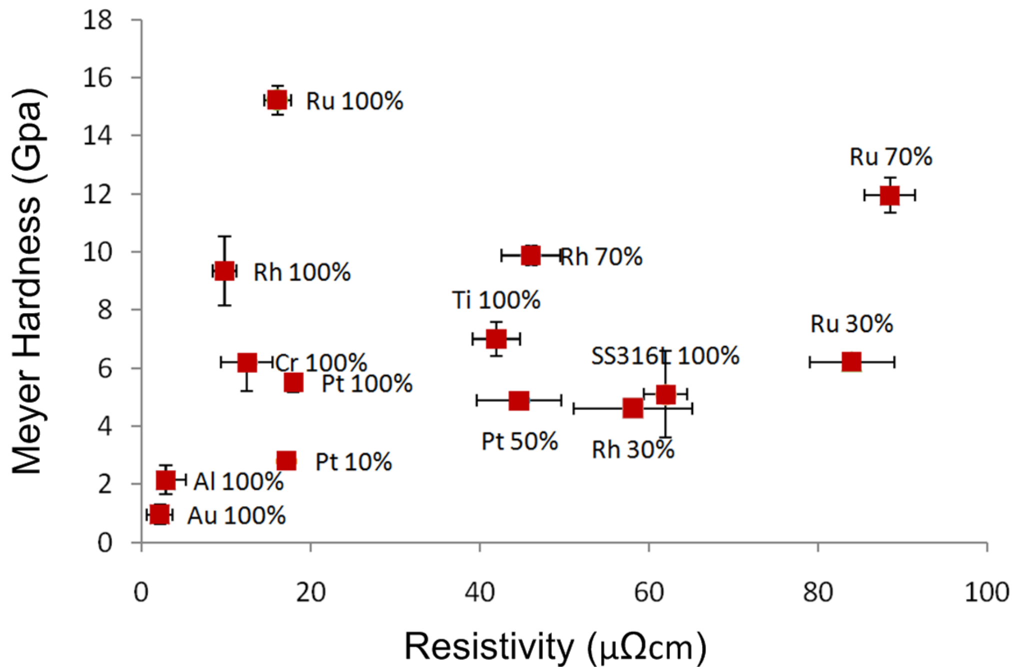

Figure 1.10: Electrical resistivity versus hardness for various metal films (1500 nm thickness) on the Si substrate, expanded from [Lee06]

1.4.1. Platinum-rhodium

Pt-Rh is the material used to make high quality crucibles. It is not only chemically inert but also mechanically robust (particularly because of the Rh content), and has been reliably used to withstand very harsh conditions.

Platinum group and platinum contact metals were studied and indicated to significantly reduce the stiction [Maj03b, Duf01]. Pt-Rh alloy has higher hardness, and higher melting point and lower corrosion than pure platinum. Pt-Rh with 20% Rh content provides 2-3x higher hardness while increasing the resistivity by only 15-20% compared to pure platinum [Pla09, Der97]. The examination of the resistivity and the hardness (interpreted from [Lee06] and [Pla09]) in Figure 1.11 shows that gold alloys compromise low resistivity for increased hardness. The percentages cited against plotted data points indicate the percentage of the alloy metal; the remainder is Au. It can be seen that 80:20 Pt-Rh is roughly at the same hardness as rhodium but has lower resistivity than the 30:70 Au-Rh alloy. In overall comparison, 80:20 alloy of Pt-Rh shows excellent compromise between resistivity and hardness. These properties make Pt-Rh an attractive candidate for high power DC and RF micro-relays; it is expected to be resistant to the softening and microwelding at elevated temperatures that may rise during high power signal transmission.

1.4.2. Micro electro-discharge machining

Although hard-metal alloys exhibit superior properties as mentioned earlier, until recently there has not been a lithography-compatible, subtractive micromachining technology that could be used for these materials. Micro electro-discharge machining (μEDM) provides such a technology. The technique employs controlled, continuous, spark discharges between a tool and workpiece (cathode and anode interchangeably), submerged in a dielectric fluid. The machining is suitable to pattern microstructures with any conductive material including metals such as stainless steel, tungsten carbide, permalloys

which are otherwise challenging to machine [Mas90, Ho03, Ehr96, Koc00]. Feature sizes down to 5 μm with position accuracy as small as 100 nm are possible with μEDM [Sma09]. Serial mode μEDM uses a cylindrical tool such as a wire that is scanned across the workpiece surface to machine desired features much like a Computer Numerical Control milling tool. Serial μEDM finds applications in high aspect ratio hole drilling for fuel injector or jet printer nozzles, mould and die manufacture, and various aerospace and surgical components. Figure 1.12 shows a typical μEDM setup with electrical configuration [Tak05].

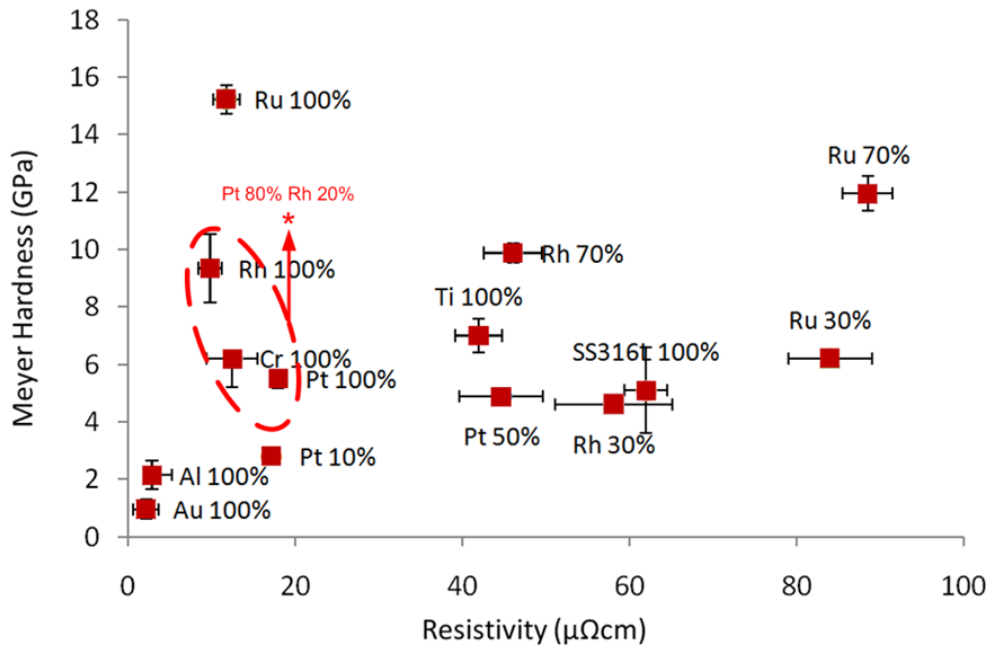

Figure 1.11: Material hardness versus resistivity of Pt-Rh (80:20) compared with several alloys and pure metals

The μEDM is based on a thermal process and forms a recast layer on the surface after machining. When a voltage bias is applied across the tool cathode and the workpiece anode in a dielectric fluid, a spark discharge occurs between the two and thermally erodes the anode side. However the cathode side is also eroded and leads to

tool wear for elongated uses. Machining mechanism of µEDM is presented in Figure 1.13 [Ric08]. Electron migration, ionization and electron avalanching are phenomena happening when sufficient voltage is applied between tool and workpiece. A plasma channel is then formed between the electrodes, passing high currents and heating the workpiece to the melting point. During the machining process, the tungsten electrode is rotated at a very high speed to prevent the welding of the electrode and the workpiece.

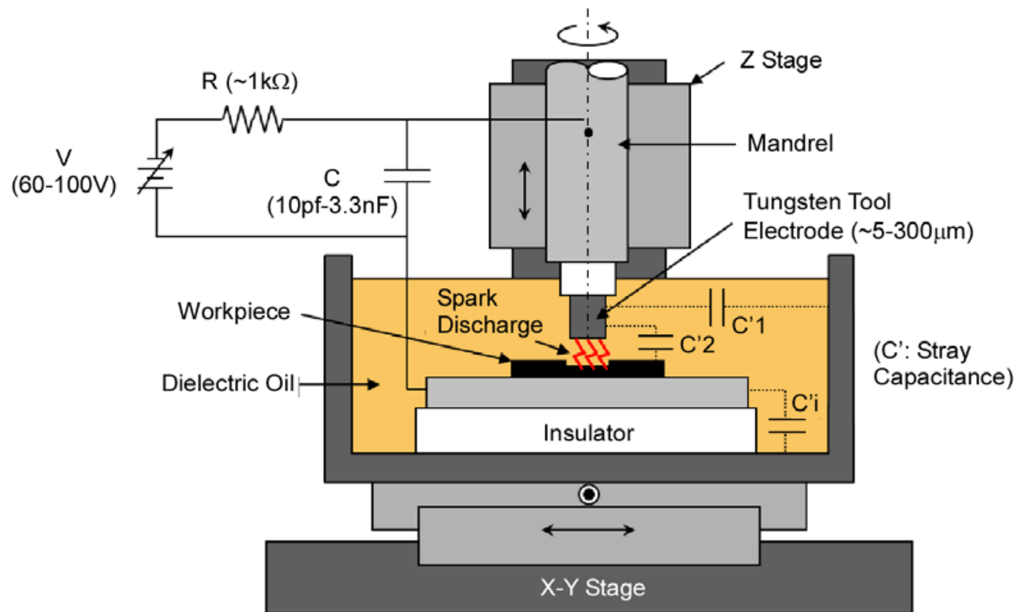

Figure 1.12: Electrical configuration and setup for µEDM adapted from [Tak05]

Batch mode µEDM is an alternative to serial µEDM for increase throughput. It uses a lithographically patterned chip – typically with electroplated Cu features on oxidized Si substrates – as a "cookie-cutter," to machine the workpiece [Tak02]. The electrode array is vibrated in a vertical axis perpendicular to the workpiece to prevent the welding of electrode and the workpiece. The schematic diagram of the setup used for batch mode µEDM is shown in Figure 1.14. This process can provide 20-30x higher throughput as compared to serial µEDM.

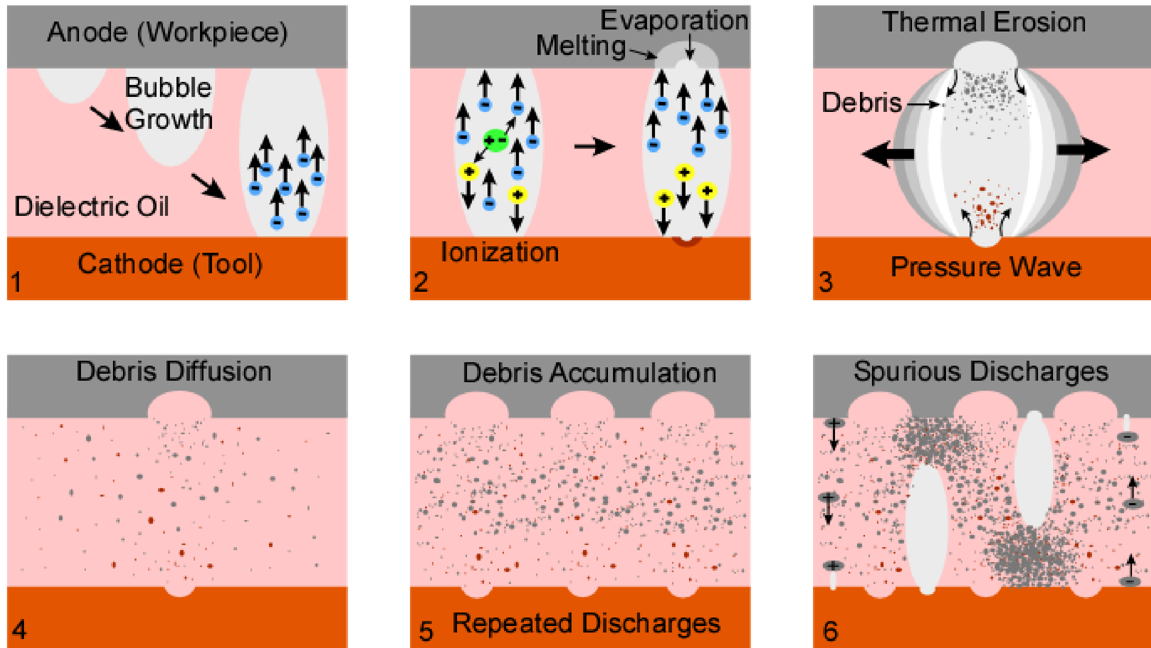

Figure 1.13: Machining mechanism of μEDM. Normal discharges are shown in Steps 1-4. In step 5, repeated discharges cause debris accumulation. Eventually, excess amounts of debris lead to discharges through debris accumulations clusters and individual debris particles shown in the middle and at the edges respectively [Ric08]

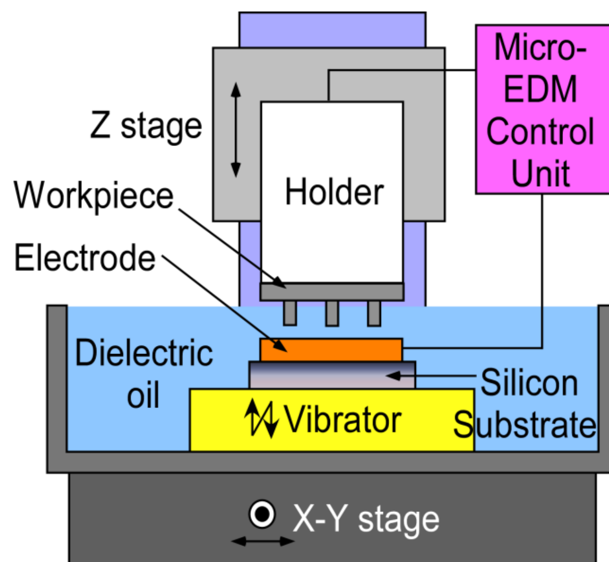

Figure 1.14: Schematic of the batch mode μEDM setup used for fabrication of microtools [Li09]

1.5. Hybrid assembly and packaging on the printed circuit boards

Although many types of micro-relays have been fabricated and shown to function individually, device integration with various functional components on the same substrate to create complete, reconfigurable and multifunctional communication systems [Bro98, Kim01, Huf06, Lee09] remains a challenging research topic.

For multifunctional and reconfigurable microsystems, most RF MEMS switches which are fabricated on Si, GaAs, Quartz, Alumina [Che09, But08, Kre05] require a system level attachment to the substrates where other components are located using interconnection techniques such as wire-bonding. The wire bonding is one of the most widely used interconnection technique for IC and MEMS packaging however at high frequencies, bonding wires are known to introduce parasitic effects and impedance mismatching [Sut01]. These effects and mismatch exhibit undesired signal losses on the RF components which deteriorate device performance. Other interconnection techniques such as flip-chip are used to achieve system level integration [Har00, Sin99] however are still susceptible to RF performance degradation due to the aforementioned effects.

Printed circuit board (PCB) technology provides substrates suitable for system level integration. PCB is a commonly used for RF applications including phase shifters and antennas [Ram05, Cet03, Sun05]. PCB offers several advantages such as wide range of substrate thickness and dielectric constants, and low loss tangent which is highly desired in reducing losses and mismatches. These properties make PCB a good substrate candidate for direct micro-relay fabrication and integration to other RF front-end system components. Past efforts on RF MEMS switch fabrication on PCB substrates [Cha05, Gho05, Ram07] focused on applications limited to very low power and did not consider

device packaging which is essential for environmental protection and increasing device reliability. Figure 1.15 shows a capacitive RF MEMS switch out of Al membrane sputtered on PCB in CPW transmission line configuration [Cha05]. The fabricated switch resulted in an insertion loss of 0.3dB, and an isolation of 23 dB at 20 GHz.

PCB also provides high DC current carrying capacity [Lin02] and can support several amperes of current.

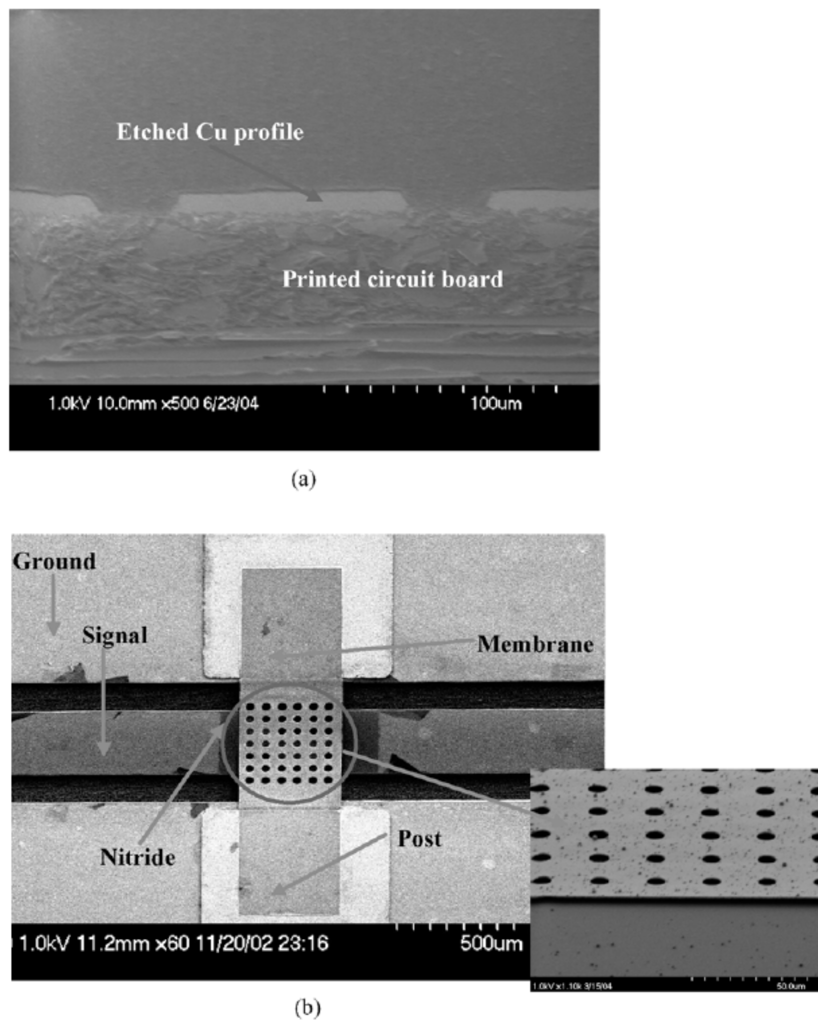

Figure 1.15: SEM image of the RF MEMS switch (a) CPW etch profile. (b) Switch with 200 µm wide Al membrane [Cha05]

1.6. Goals and approach

High power DC and RF switching (>1 A, >1 W) impose key challenges. Micro-relay failures due to thermal stiction causing alloying, softening and microwelding could be alleviated by careful design and choice of contact materials.

Micro-relays micromachined from bulk foils such as platinum-rhodium (Pt-Rh) might present an alternative for conventional high power relays and MEMS RF switches which require mechanical, electrical, chemical, and thermal integrity. The use of hard metal foils can potentially prevent adhesion problems, and can withstand high temperatures without softening, alloying or microwelding to the contact surface.

The overall objective of this work is to investigate high power switching using bulk foil Pt-Rh. The following are the goals targeted in this work.

1. Show the feasibility of Pt-Rh as a candidate contact metal for high power switching. Design a high power DC micro-relay with bulk foil Pt-Rh contacts. Investigate possibility of integrating a heat sink and an active cooling technique and the impact on maximum power. Develop multiphysics simulations to accurately model electrostatic and thermal behaviors. Fabricate the micro-relays and develop a technique for direct on printed circuit board (PCB) integration. Evaluate DC power handling through a series of electrical and thermal tests.
2. Design an RF micro-relay with bulk foil Pt-Rh contacts. Iteratively optimize RF transmission line as well as DC path for maximum RF performance. Fabricate he micro-relays and perform experiments for DC, RF and thermal characterization.
3. Develop a process for batch fabrication of at least four devices simultaneously. Implement a package directly integrated on the PCB. Fabricate the devices and

perform a set of experiments for full DC and RF characterization as well as PCB-package leakage tests.

1.7. Outline

Chapter 2 reviews failure mechanisms in MEMS switches. Chapter 3 presents an all-metal high power micro-relay with an integrated heat sink and directly assembled on a PCB. Chapter 4 describes a micro-relay for high power RF applications. A process for a batch fabricated and packaged micro-relay is presented in Chapter 5. Chapter 6 provides the conclusions and the future work.

CHAPTER 2

POWER HANDLING OF MEMS SWITCHES

Although significant attention has been devoted to the longevity of micro-relays, the focus has been primarily directed at devices handling relatively low levels of power, i.e. below 100 mA DC and 100 mW RF [Reb03]. High DC and RF power handling in micro-relays is of interest for power conversion, transmitters in satellites, earth-based communications stations and radars [Jac06, Won00, Nor99, Cae09]. Power handling of micro-relays and MEMS switches is a major concern to realize such applications. For switches that offer capacitive paths (used with RF signals), power handling is primarily affected by dielectric charging, whereas for ohmic-contact switches the microwelding of contact surfaces due to localized contact heating is the predominant failure mode. Although there have been a number of efforts to address the power handling limitations thorough design reconfigurations [Per04, Gre05, Hon04], contact failure mechanisms that define the power handling capability of the ohmic-contact micro-relays are strongly related to the nature of the contact metals [Jen05, Cou04, Lee06, McG06, Kwo07]. Therefore, a study of contact metals and contact physics is essential for the design efforts towards a high power ohmic-contact micro-relay.

This chapter details the failure mechanisms for MEMS switches. Failure mechanisms and power handling of RF MEMS switches are discussed in Section 2.1.

Section 2.2 provides a quantitative benchmarking for cross-technology and in-technology micro-relays.

2.1. Failure mechanisms and power handling of MEMS switches

Device failure due to the inability to handle high levels of power is one of the largest areas under research in the field of MEMS switches. Failure mechanisms can be investigated for MEMS capacitive and ohmic-contact switches separately.

Major reliability issues which impoverish the power handling capabilities of MEMS switches stem from the dielectric charging based stiction for devices with capacitive paths and the selection of contact materials for devices with metal-to-metal ohmic-contacts. Similarly high-power handling conditions are different for capacitive and ohmic-contact switches and should be examined separately.

2.1.1. Low-medium power failure mechanisms for MEMS capacitive switches

The stiction due to the dielectric charging between the dielectric layer and the metal layer is the predominant failure type for low-to-medium power (<1 A DC, <1 W RF) capacitive switches. This phenomenon occurs due to the large switch contact areas and charge injection which traps in the dielectric layer. This trapped charge injection causes undesirable adhesion of compliant microstructure surfaces. The adhesion becomes inevitable when mechanical restoring forces are inadequate to overcome the interfacial forces such as capillary, electrostatic, van der Waals, and Casimir forces, and other kinds of chemical forces [Mab02, Ash01, Ash01-2, Zha02a, Zha02b]. There are only few efforts investigating the cause of stiction [Zha03]. The charge accumulation in

the passivation layer, typically silicon nitride, is forced to support a large electric field and is exposed to repeated contact with the metal bridge when the actuation potentials are applied. This eventually leads to static charge build-up which eventually becomes trapped within the dielectric layer. Since the charge has no conductive path to ground, it cannot disperse. Therefore, the charge accumulates until ultimately there is enough charge to permanently hold the switch in its down-state position.

The stiction problem of MEMS switches can be divided into two categories [Kim01a]: release-related stiction and in-use stiction. Release-related stiction arises during the removal process of the sacrificial layer in fabrication, and such stiction is caused primarily by the capillary forces. The processing issues can usually be eliminated by convenient techniques with minimal difficulty, such as the inclusion of a supercritical carbon dioxide drying technique [She01, She02].

On the other hand, in-use stiction usually occurs due to the aforementioned dielectric charging. Few design level considerations have been taken to deal with the in-use stiction phenomenon [Tou08, Obe97, Per04]. Figure 2.1 shows the stiction of an RF MEMS switch to the substrate [Zha03]. Figure 2.2 exhibits a MEMS switch designed to overcome the stiction [Tou08]. The design employs two sets of electrodes; inner and outer electrodes that realizes two actuations in inverse directions to release the membrane when stiction occurs.

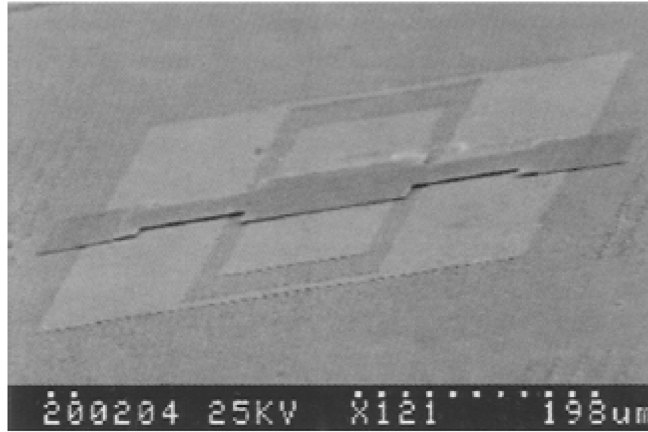

Figure 2.1: SEM image of RF-MEMS switch adhered to substrate [Zha03]

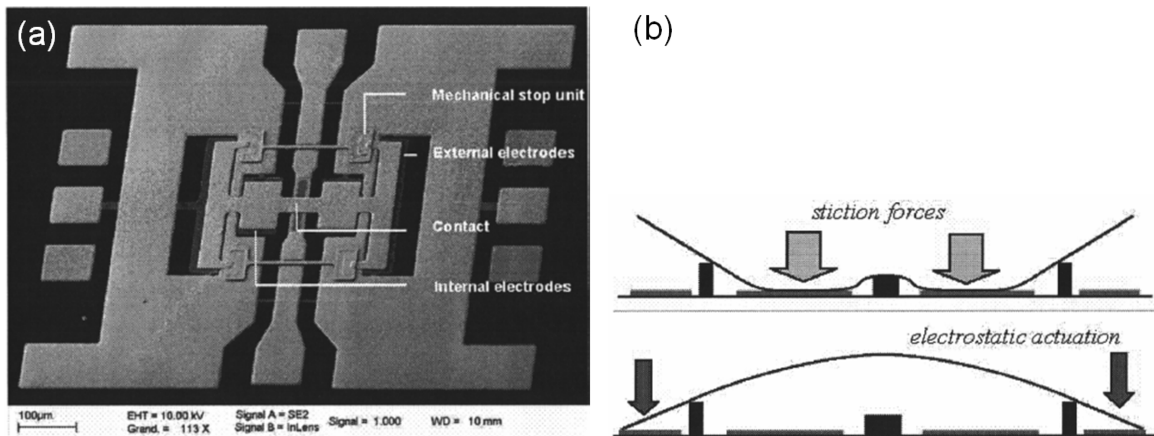

Figure 2.2: Stiction release design (a) device SEM image, (b) mechanism schematic [Tou08]

Another possible solution to the dielectric charging problem is choosing the right dielectric material. The use of silicon dioxide as dielectric layer minimizes charging problem since PECVD silicon dioxide has a much lower trap density than PECVD silicon nitride [Sze81] which results in reduced charging.

Use of bipolar actuation voltage is another technique to alleviate dielectric charging problem. As shown before, the electrostatic force on the fixed-fixed or cantilever beams is proportional to V^2, hence a bipolar voltage would result in a constant attractive force on the beam. If a square wave is applied with a frequency much higher

than the charging frequency (~5-20 kHz) in the dielectric layer, then the dielectric would not charge since the beams could not react to this abrupt change in the force [Reb03].

2.1.2. Low-medium power failure mechanisms for MEMS ohmic-contact switches

The dominant failure mechanism for low-power ohmic-contact switches is due to the mechanical damage, pitting and hardening of the metal contact area and is often a consequence of the impact forces between the top and bottom metal contacts [Reb03]. Pitting and hardening phenomena (Figure 2.3) occurs when two contact metals hit each other repeatedly over the same spot [Mih01b]. This occurrence considerably reduces the contact area and increases the contact resistance. Damage, pitting and hardening strongly depends on the contact metals used.

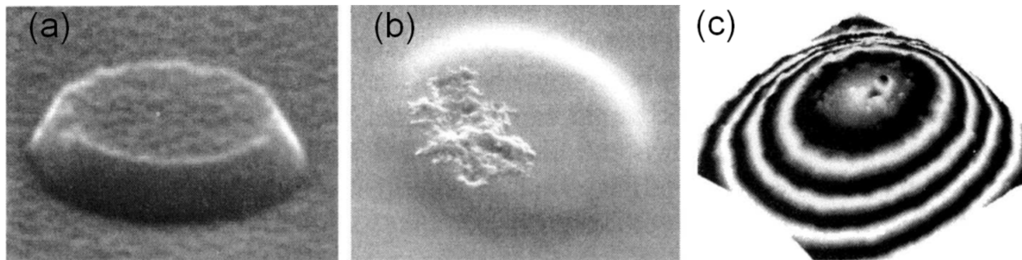

Figure 2.3: (a) Clean gold contact, (b) contact after pitting and hardening under high actuation voltages, (c) hardness measurements done using AFM probe [Mih01b]

2.1.3. High power failure mechanisms for MEMS capacitive switches

One of the dominant high power (>1 A DC, >1 W RF) failure mechanisms for capacitive switches is self-actuation or self pull-in. This phenomenon occurs when the voltage carried on the signal or transmission line generates sufficient electrostatic force to pull the beam down, shorting the line. Figure 2.4 depicts self pull-in mechanism schematically [Per03].

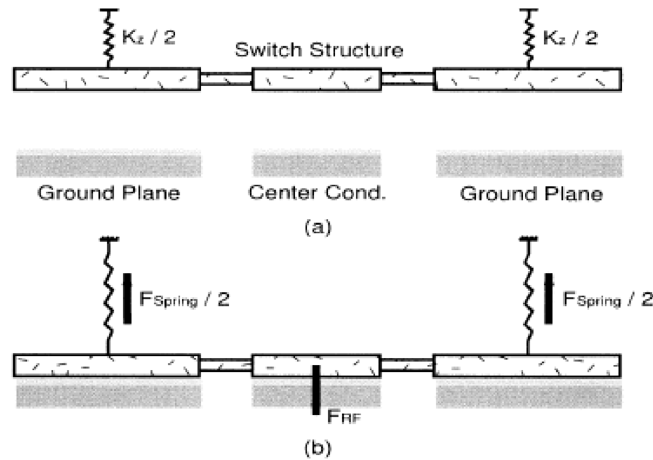

Figure 2.4: Self-actuation mechanism. (a) The switch is initially in its up-state over a CPW line. (b) RF generated force on the CPW line is higher than the pull-in force and the switch is actuated with no bias voltage present [Per03].

The dielectric breakdown between the top and bottom electrodes constitutes another high power failure mechanism for capacitive MEMS switches [Hou07]. The electric failure mechanism can be schematized as shown in Figure 2.5. The electrode with a certain amount of surface roughness may have small peaks at the surface asperities, which get closer to the top electrode in the down-state, and so the electric field intensity is locally amplified over those peaks. When the surface roughness is in the order of several tens of nanometers, the effective voltage density becomes much higher, sometimes exceeding breakdown voltage and resulting in failure.

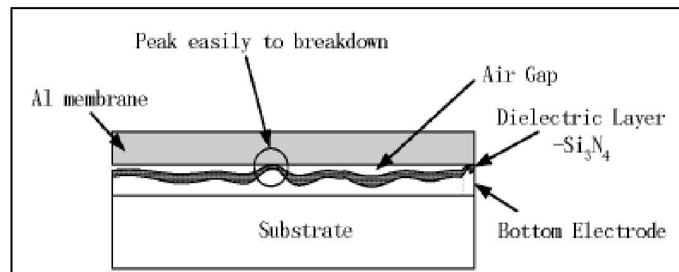

Figure 2.5: Mechanism of the breakdown due to small peak in rough dielectric layer surface [Hou07]

Figure 2.6 displays the pictures of the electrode surface after breakdown. Few breakdown spots in failure are easily seen on the figure.

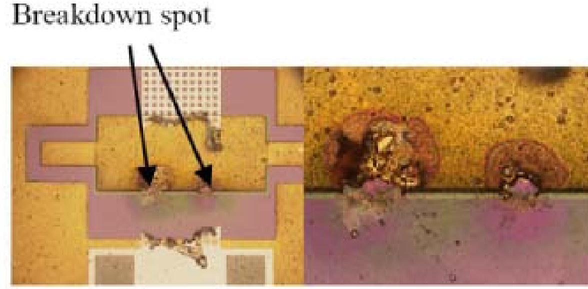

Figure 2.6: Pictures of the capacitive MEMS switch after the dielectric breakdown [Hou07]

2.1.4. High power failure mechanisms for MEMS ohmic-contact switches

Contact temperatures due to the localized heating play an important role in understanding high power failure mechanism for ohmic-contact switches. Thermal constriction conductance, G_t, is defined as the ability of a contact to dissipate heat through the contact region [Mad95, Hym99] and given by:

$$G_t = \frac{1}{R_{cd1}(1+F\left(\frac{r}{b}\right))} \tag{2.1}$$

with,

$$R_{cd1} = (4kr)^{-1}$$

$$F\left(\frac{r}{b}\right) = 1 - 1.4098\left(\frac{r}{b}\right) + 0.3441\left(\frac{r}{b}\right)^3$$

where k is the material thermal conductivity, r is the contact spot radius and b is the cathodic contact radius which is experimentally determined. The temperature increase due to joule heating effect is given by:

$$\Delta T = \frac{P}{G_t}\frac{|I_l|^2 R}{G_t} = \frac{|I_l|^2 \tau\rho}{G_t \pi r} \tag{2.2}$$

where, P is the dissipated power in the contact region, R is the contact resistance, ρ is the contact metal resistivity, r is the contact radius and τ is the temperature factor. The temperature factor can be described by:

$$\tau = \frac{R(T)}{R_0} \approx \left(1 + \frac{2}{3}\alpha T\right) \tag{2.3}$$

where R_0 is the resistance at ambient temperature, $R(T)$ is resistance at temperature T, and α is the temperature coefficient of resistance for the contact metal.

Following (2.3), typical temperature increase in gold-gold contacts can range from 10-30 ºC for only 50-100 mA of DC current and can reach few hundred ºC for >1 A. The temperature can increase higher in hard metal contacts due to higher resistivities. Excessive local heating can cause contact metal softening, alloying and microwelding where two metal contacts swap and merges atoms and transfer material.

Figure 2.7 presents a combination of contact asperities and high current condition [Jen05] and its effect on the contact resistance. Figure 2.8 shows, SEM image of a gold-gold contact which melted due to excessive current flow.

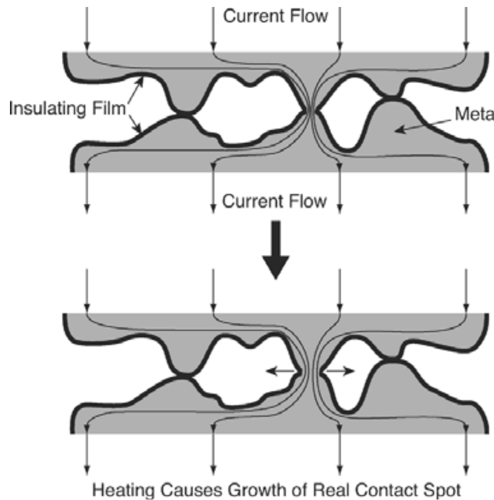

Figure 2.7: Illustration of the surface asperities and the contribution to high current induced heating. Heating due to the current flow in the contact spot leads to a resistance decrease caused by the material annealing or film breakdown [Jen05].

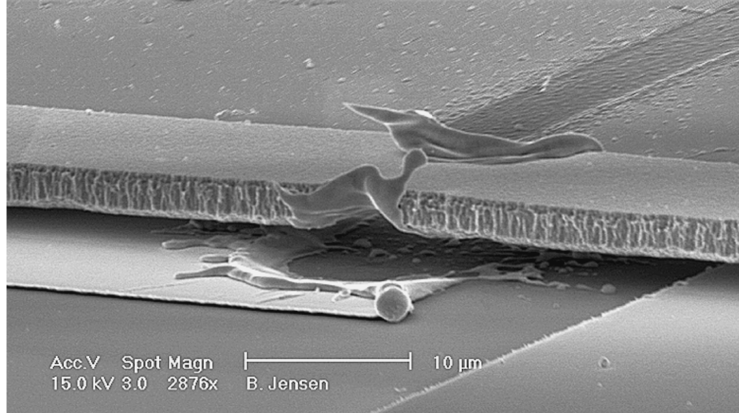

Figure 2.8: SEM image of a melted gold contact due to excessive heating [Jen05]

2.2. Quantitative benchmarking

This section covers quantitative benchmarking for high power switches. The benchmarking is done for two cases: cross-technology and in-technology. In the cross-technology comparison, various kinds of high power semiconductor switches are benchmarked whereas in the in-technology comparison, high power MEMS switches are benchmarked.

For the cross-technology comparison, various kinds of state-of-the-art semiconductor switches are presented, including both research-phase and commercial devices. These include a commercial high power thyristor [Sem09], a solid state DC relay [Aut09], an IGBT [Fai09], a high power HFET single pole single throw (SPST) switch [Ish05], a SiC Schottky diode [Cre08], and another commercial GaAs SPDT RF switch [Per08]. The comparison is presented in Table 2.1.

Table 2.1: Cross-technology comparison of various semiconductor switches

Device / **Properties**	SKKD 57/08 E G6 Thyristor [Sem09]	ADSSR 210D SS DC Relay [Aut09]	ISL9V2040S 3S IGBT [Fai09]	AlGaN/ GaN HFET [Ish05]	SiC Schottky Cree C2D10120 [Cre08]	GaAs SPDT Peregrine PE42510A [Per08]
Bandwidth	DC	DC	DC	DC–1GHz	DC	30 MHz–2 GHz
Power (W)	225	200	130	43	18–30	32
Max current (A)	45	10	10	1	10	1
Resistance (Ω)	0.005	N.A.	0.6	0.93	0.10-0.15	N.A.
Turn-on time (μs)	1	10000	2	N.A.	N.A.	45
Insertion loss (dB)	N.A.	N.A.	N.A.	0.26 @ 1 GHz	N.A.	0.40 @ 800 MHz
Isolation (dB)	N.A.	N.A.	N.A.	27 @ 1 GHz	N.A.	29 @ 800 MHz
Stand-off voltage (V)	3600	4000	430	100	600–1200	2000
Size (cm^3)	85.8	352	1.5	0.144	1.42	0.08

Table 2.2: In-technology comparison of various RF MEMS switches

Device / **Properties**	[Per04]	[Mah10]	[Cho09]	[Kwo07]	[Maj03a, Maj03b Mac04]	**This Work**
Type	Electro-static	Electro-static	Electro-thermal	Piezo-electric	Electro-static	Electrostatic
Bandwidth (GHz)	DC–40	DC–10	DC–10	DC–20	DC–4	DC-10 GHz
Power (W)	0.8	4	4.6	1.4	0.001–2	**20**
Max current (A)	N.A.	N.A.	N.A.	0.1	0.5-1	**2.8**
Resistance (Ω)	N.A.	N.A.	1.5–2	0.49–1.2	1	**1.1**
Turn-on time (ms)	N.A	≈0.005	14,000	< 5	0.005	10
Insertion loss (dB)	0.17 @ 40 GHz	0.1 @ 10 GHz	0.3 @ 10 GHz	0.5–1 @ 10 GHz	0.32 @ 2 GHz	0.25 @ 5 GHz
Isolation (dB)	15 @40 GHz	15 @10 GHz	30 @12 GHz	30 @10 GHz	33 @2 GHz	15 @ 5 GHz
Footprint (mm^2)	≈0.1	≈0.2	105	≈1	≈0.02	8.4
Switch type / contact materials	capacitive	capacitive	ohmic-contact/ Au/Au	ohmic-contact/ Au/Au, Ir/Ir, Au/Pt	ohmic-contact/ Pt-Pt	ohmic-contact/ Pt-Rh/Au

For the in-technology comparison, specifications of five MEMS switches are shown. The device reported by Peroulis et al. [Per04] was a capacitive RF switch with a large bandwidth. Micro-relay had 0.8 W power handling under hot switching conditions (where RF source is constantly kept on) and competitive footprint. Mahameed et al. recently reported a high power RF switch which can handle 4 W [Mah10]. Choi et al. introduced an ohmic-contact RF switch with 4.6 W power handling, however the footprint was considerably large for array applications. Another ohmic-contact switch employed Pt-group metals as contact material [Kwo07]. RF power handling of 1.4 W and DC current handling of 100 mA were reported. The Radant switch [Maj03a, Maj03b, Mac04] is a well-known micro-relay with DC current ratings up to 1 A and RF power handling up to 2 W. Finally, the work presented in this thesis is provided as benchmarking. The comparison is presented in Table 2.2.

CHAPTER 3

MICROMACHINED Pt-Rh AND STAINLESS STEEL RELAYS FOR HIGH POWER DC APPLICATIONS

As discussed in Chapter 1, the overall objective of this work is to investigate high power switching using bulk foil Pt-Rh. This chapter describes the evaluation of Pt-Rh as a micro-relay material using an all-metal three-terminal test structure [Ozk10a-Ozk10b]. Its performance is compared to stainless steel as a point of reference. Although the test structure is not intended for large scale production, it permits the evaluation of the alloy material and design concepts. This chapter also reports on the possibility of integrating a heat sink and an active cooling mechanism and evaluates the impact on the maximum power handling. In addition, a preliminary process for hybrid on-PCB device integration is introduced. Section 3.1 describes the micro-relay design. Section 3.2 details the fabrication and assembly processes for the device. Experimental setup and results are presented in Section 3.3. These include electrical characterization, thermal performance, and preliminary lifetime tests for the device. The discussion and conclusions are provided in Section 3.4.

3.1. Design

The micro-relay utilizes a three-terminal structure (Fig. 3.1(a)). The design has a footprint of 2.6×2.5 mm^2 and it employs vertically stacked components that are directly

assembled on a PCB which uses a 1.6 mm-thick FR-4 substrate. Interconnect traces of 90 µm thickness Cu were chosen for high current ratings (4.5 A for 400 µm wide signal lines). In such PCBs, a 4-µm thick Ni layer covers the Cu traces, and a 0.15-µm thick outer gold layer provides the contact surface. The layout has three distinct regions: a ground electrode which acts as the source; an open signal line with a break in the middle which acts as the drain; and an electrically floating anchor pad with through vias, which accommodates the alignment and the placement of components to construct the micro-relay.

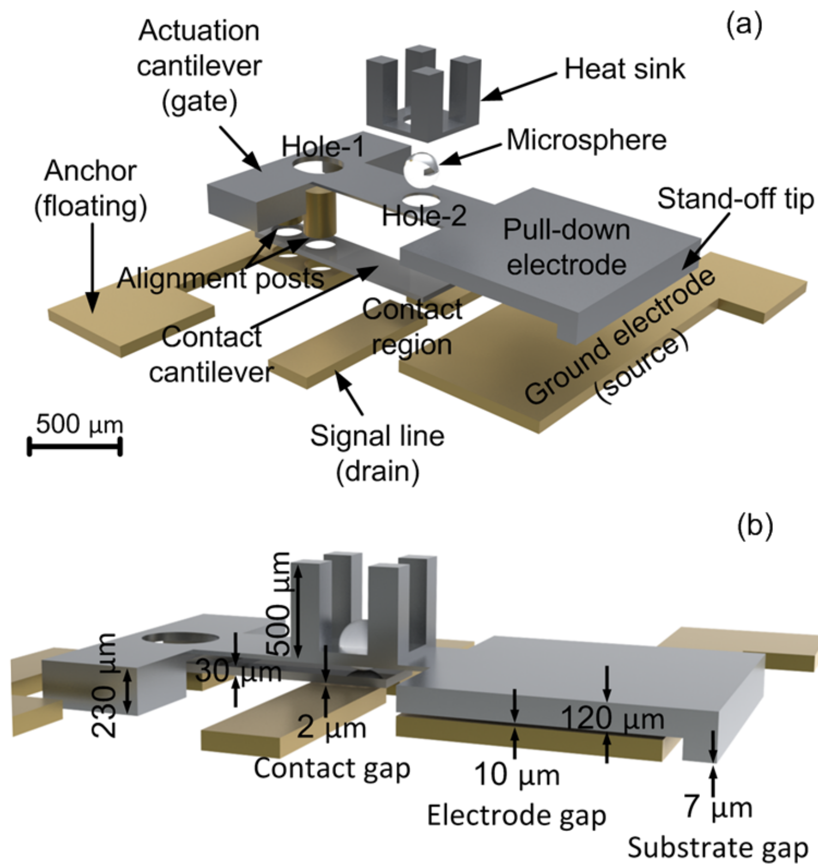

Figure 3.1: (a) Exploded view of micro-relay showing double cantilever structure. Gold posts align and hold the cantilever over gold-coated copper traces on the PCB. Recess depths are 2 µm and 100 µm on contact and actuation cantilevers respectively. The actuation cantilever is isolated from the contact cantilever and pushes it down via thermally conductive microsphere. An extension at the tip prevents pull-in. Heat sink is integrated atop. The design has an actuation area of 1.32 mm^2 as defined by the footprint of the pull-in electrode (1200×1100 µm^2). (b) Side view showing critical gaps for electrostatic actuation and pull-in prevention.

A Pt-Rh contact cantilever (400×1400×30 μm^3 including anchor; 600 μm suspended length), is located orthogonally with respect to the signal line and suspended above the break. Two alignment posts, extending from the vias, perforate the contact cantilever and fix it to the anchor on the PCB. The underside of the contact cantilever has a recessed region of 2 μm height, over the signal line, to provide with an initial gap (Fig. 3.1(b)).

An aluminum actuation cantilever (1200×2100×230 μm^3 including anchor; 1500 μm suspended length) is attached directly on the PCB substrate and suspended above the contact cantilever. A paddle shaped extension at the distal end acts as a pull-in electrode (with 1200×1100 μm^2 actuation area) and allows electrostatic actuation when biased with respect to the electrode below it. A stand-off element extends from the tip of the actuation cantilever. The gap between the stand-off tip and the substrate is designed to be 7 μm – 3 μm smaller than the electrode gap across the actuation cantilever and ground electrode – to prevent pull-in. (It is recognized that in an environment that is not clean an electrically insulating layer will be necessary to prevent inadvertent shorting of the actuation electrodes.) *Hole-1* on the actuation cantilever prevents contact with the alignment posts, whereas *hole-2* accommodates subsequent placement of a microsphere.

A thermally conductive sapphire microsphere (Edmund Optics, 300 μm diameter, 45 $W \cdot K^{-1} \cdot m^{-1}$ thermal conductivity) is used on the contact cantilever. It fits tightly in *hole-2* which has the same diameter. The microsphere mechanically couples the actuation cantilever with the contact cantilever while keeping it electrically separated. It provides a single point of contact between the actuation cantilever and the contact

cantilever, partially alleviating any assembly imperfections. In addition, it provides a thermal conduction path to dissipate heat away from the electrical contact region.

An aluminum heat sink (500×500×500 μm^3, 475 μm fin height) is located above the actuation cantilever. A through-hole at the base of the heat sink, concentric with *hole-2* on the actuation cantilever, supports the microsphere and provides a heat dissipation path from contacts to the heat sink fins. The gap between the fins is defined to allow the placement of the microsphere (Fig 3.2).

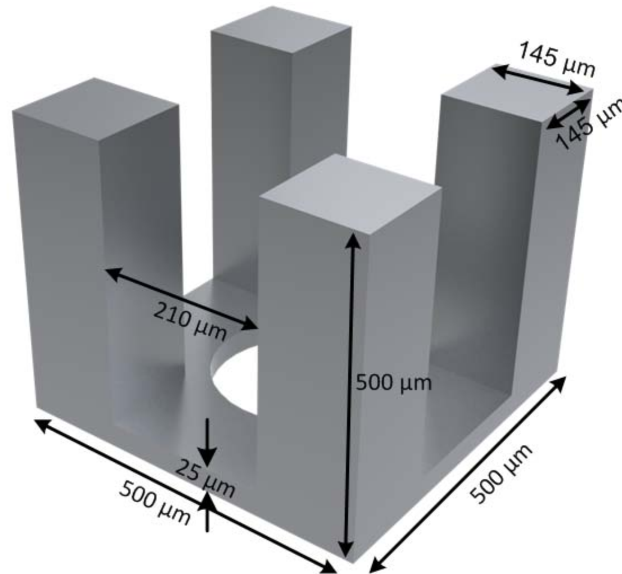

Figure 3.2: Heat sink dimensions

Two design criteria were followed for designing the heat sink fins [Cim94]: 1) heat loss limit should be larger than 1, and 2) fin efficiency should be larger than 0.75. The heat loss limit, h_l, is defined by:

$$h_l = \frac{2k}{ht} \geq 1 \tag{3.1}$$

where k is the thermal conductivity of the sink material (W·K^{-1}·m^{-1}), h is the heat transfer coefficient (W/m^2 · K) and t is the fin width (m). At room temperature (300 K),

for air ambient and a fin width of 145 μm, the heat loss limit is 4.83. Fin efficiency is defined by:

$$\eta = \frac{\tanh(ml)}{ml} \geq 0.75; \qquad m = \sqrt{\frac{2h}{kt}} \tag{3.2}$$

where l is the fin height. The efficiency of the designed fin is 0.812 for a fin height of 475 μm.

Results from the electrostatic-mechanical modeling of the micro-relay are shown in Fig. 3.3. The simulations were carried out in ANSYS. All the PCB traces were neglected. The "no-penetration" contact conditions were applied where the glass microsphere touches the contact cantilever at a single point. The "bonded contact" condition was used everywhere else. The "fixed geometry" condition was used at the anchors. The electrodes and contact gaps were set to 10 μm and 2 μm, respectively. The pull-in voltage for a 7 μm vertical tip displacement was 120 V; at this point the stand-off tip touched the substrate. The spring constant for the device with combined cantilever pair, heat sink and the microsphere, was 56 N/m. The contact force per contact region was 1.1 mN for 150 V actuation voltage; the switching time was 9.4 ms.

Thermal modeling for contact heat dissipation and forced cooling requires a good estimate of the contact resistance to account for joule heating. Holm's plastic deformation model, introduced in Section 1.3.1, was initially used to estimate the contact resistance. Since the contact pair used in the design was Pt-Rh/Au, the contact resistance in equation 1.16 was developed into [Sla99]:

$$R_C = \frac{\rho_1 + \rho_2}{4\alpha_H} \tag{3.3}$$

Here, ρ_1 and ρ_2 are the electrical resistivities of the contacting metals. Adopting the contact mechanism proposed in [Bow64], it can be assumed that contact pressures on a contacting pair of asperities are equal to the flow pressure of the softer of the two contacting materials and that the normal load is supported by plastic flow of the softer asperities of that pair. However, it is important to note that in a multilayered structure the effective hardness is affected not only by the hardness of the top layer, which is thin in this case, but also by the hardness of thicker bottom layer material. Determining an exact value for hardness in the multilayered Cu/Ni/Au patterns used for the PCB traces is nontrivial and tabulated values for specific multilayer films are not readily available. The contact resistance modeling of sputtered films with different thicknesses and its mismatch with Holm's theory has been previously reported [Rea09]. Since the thickness of the Ni layer (4 μm) is sufficiently larger than the thickness of the Au (0.15 μm), the effective hardness was chosen as that of Ni. Using equations 1.15 and 3.3, a contact resistance of 620 mΩ was found for the micro-relay design, with an estimated contact hardness of 6 GPa – the approximate Meyer hardness of Ni, unity *n*, approximate combined resistivity of 30 μΩ·cm for Pt-Rh/Cu/Ni/Au contacts, and 1.1 mN contact force per contact region (estimated by FEA for 150 V actuation voltage). The theory suggests 241 nm radius for α-spot.

To verify the theoretical model, contact resistance was also estimated empirically. The experiment followed a procedure similar to the one described in [Rea09]. It involved manually placing a μEDM'ed Pt-Rh beam, with the intended dimensions of contact cantilever, against open signal lines, and then applying a controlled contact force. The contact force was supplied by a precision force gauge (Aurora Scientific, Model 403A).

The gauge was mounted on a motorized x-y-z stage and brought into close proximity to the Pt-Rh beam. The force was applied over a 1 mm contact diameter, in 200 μN increments, up to 2.2 mN. The test current was sourced at a level of 5 mA, while contact resistance was measured using a 4-wire technique. The total series resistance was 0.8 Ω for 2.2 mN total contact force that was distributed evenly over two contact regions. The empirical method estimates an α-spot of 186 nm radius. The change of contact resistance with the contact force and its comparison to Holm's model is shown in the Fig. 3.4. The empirically estimated contact resistance was larger than the theoretical estimate by approximately 25%.

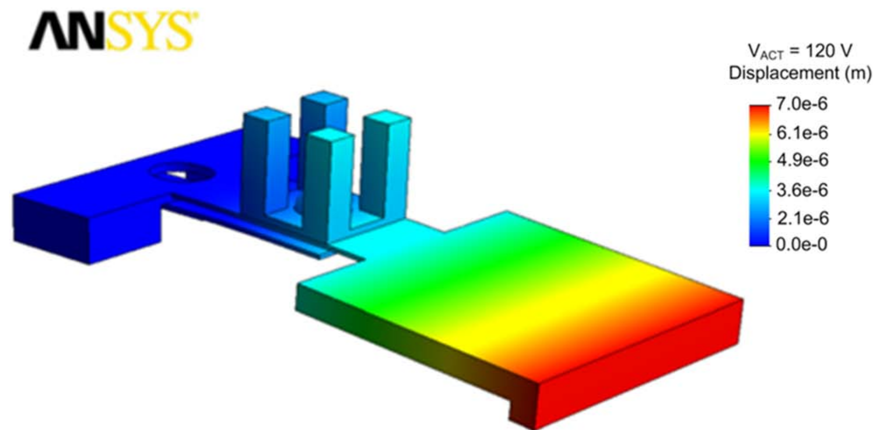

Figure 3.3: Electrostatic FEA showing displacement results for micro-relay. V_{ACT} is electrostatic actuation voltage (120 V) applied on the pull-in electrodes to cause cantilevers to travel 7 μm, before stopped by the stand-off tip. Simulated contact force and actuation time are 1.1 mN/contact region and 9.4 ms, respectively, for an increased voltage of 150 V

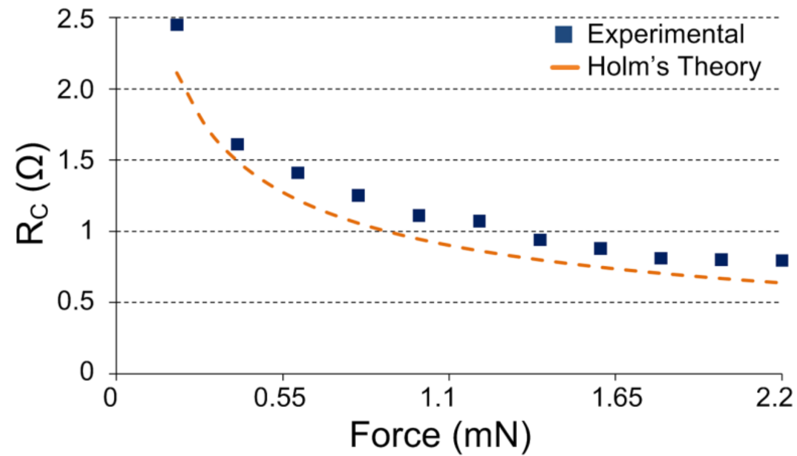

Figure 3.4: Preliminary estimation of total series contact resistance with for use in the thermal model. Experimental plot showing the change of contact resistance with increasing force supplied from a force gauge on a Pt-Rh contact cantilever. The force was supplied in 200 µN increments, up to 2.2 mN total force (to obtain 1.1 mN force equally per contact area). The data is compared with Holm's contact model. For 2.2 mN, the experimentally estimated contact resistance was 0.8 Ω whereas Holm's model predicted 0.62 Ω.

The empirically estimated contact resistance was used to determine joule heating boundary condition in the finite element model for contact heat dissipation. The adhesive between microsphere, actuation cantilever and heat sink was thermally modeled as an overlapping shell only around the microsphere with a thermal conductivity of 5 W/m·K following the specifications of commercially available epoxy (Aavid Thermalloy). To model the forced cooling via a commercially available mini-fan (Sunon-UF3A3, 0.29 W power consumption), an upward air flow of 0.22 m/s was used. The air flow velocity of the mini-fan was experimentally estimated, in air, at atmospheric pressure and room temperature, by particle image velocimetry. The mini-fan was first horizontally placed with respect to an incense stick to account for buoyancy effects. The displacement of the streamed smoke was then observed on a 30 frame-per-second camera (Fig. 3.5).

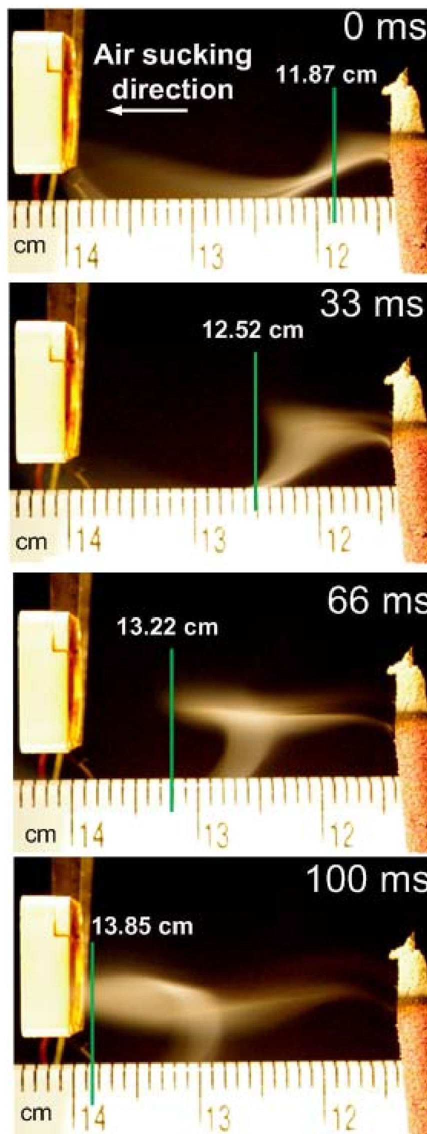

Figure 3.5: Particle image velocimetry experiment showing the smoke displacement every frame (33 ms).

Figure 3.6 shows air flow rate of a twelve-run experiment. The average rate was 0.22 m/s. To verify the flow rate near the heat sink the mini-fan was placed 1 mm above the micro-relay and the smoke was fed horizontally through a 100 μm diameter glass capillary (Fig. 3.7). The flow rate was then determined similarly using particle image velocimetry. Extracted flow rate of 0.22 m/s was in good agreement with the larger scale experiment in Fig. 3.5

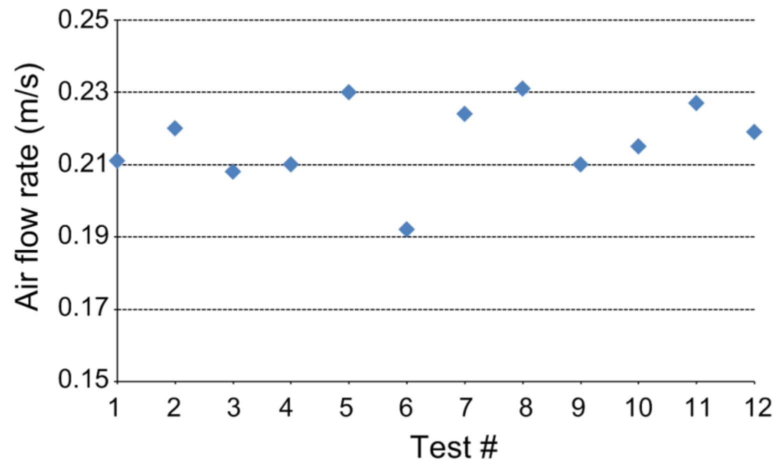

Figure 3.6: Air flow rate as a result of a twelve-run test. The test was done in air, at atmospheric pressure and room temperature.

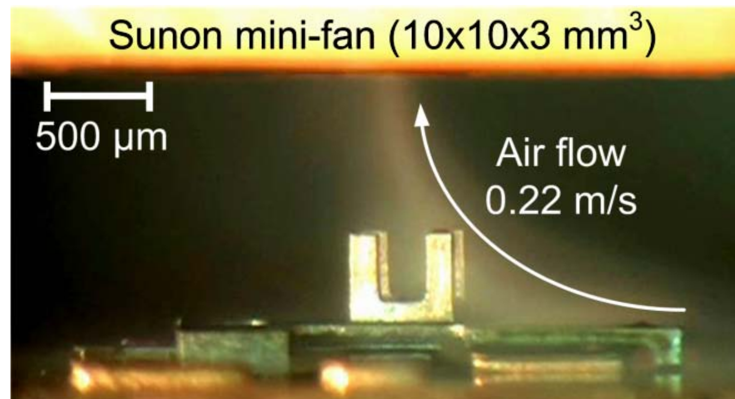

Figure 3.7: Smoke flow near the heat sink fins on micro-relay. Mini-fan (Sunon UF3A3) was placed 1 mm away from the switch and smoke was fed horizontally from the right side through a glass capillary of 100 µm diameter. Air flow velocity of 0.22 m/s was extracted from recorded images.

The modeled flow was constrained in a cylindrical box of 1.5 mm height and 1 mm diameter enclosing the contact area and the heat sink. Thermal finite-element analysis was performed in ANSYS. For both unforced and forced cooling, the temperature distribution was estimated at 1 s into the on-state. Figure 3.8 shows the temperature distribution obtained for unforced and forced cooling for 2.5 A line current, 0.8 Ω estimated contact resistance and 300 K ambient temperature. Forced cooling decreases the maximum temperature in the contact area by approximately 25 K.

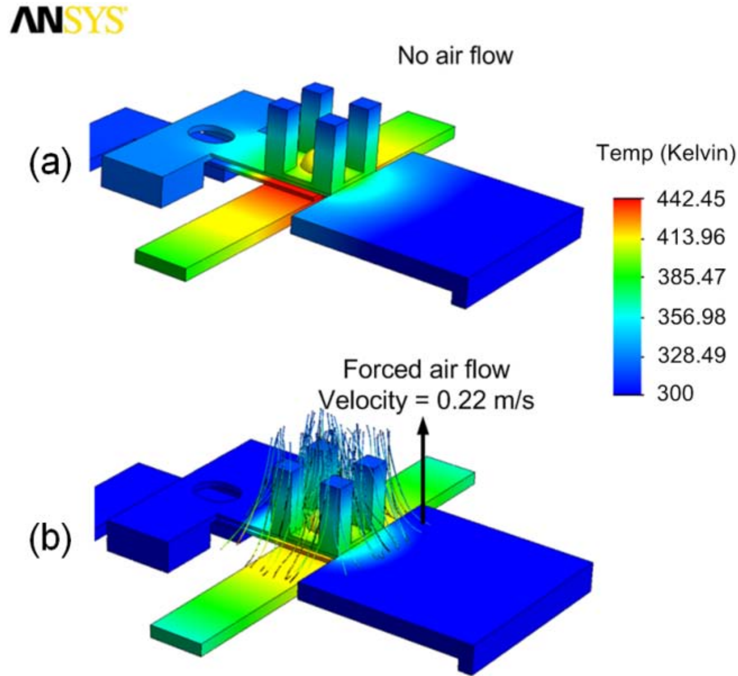

Figure 3.8: FEA results at 1 s into the on-state time with 0.22 m/s upward air flow. Temperature distribution results for (a) unforced (b) forced cooling (Pt-Rh contact cantilever, 0.8 Ω estimated total series contact resistance, 2.5 A line current, 300 K ambient temperature). Compared to unforced cooling, forced cooling suppresses temperature at contact region by around 25 K.

3.2. Fabrication and assembly

Contact cantilevers were serially fabricated using µEDM from both Pt-Rh (80:20) and SS316L alloys using 50-µm thick stock metal foils (Alfa Aesar Corp.). They are micromachined down to 30 µm thickness on anchors and 28 µm thickness over contact regions to allow for the 2 µm contact gap. Two perforations of 300 µm were located in anchor regions for attachment to the PCB via alignment posts. The lowest available discharge energy of 24.5 nJ was used for cantilever contact regions to ensure smooth surface finish. The surface roughness of the bottom side of both Pt-Rh and SS316L contact cantilevers was measured using Zygo NewView 5000 interferometer. Average roughness R_a was approximately 45 nm for both cantilevers. In comparison, the virgin

material had average roughness R_a 25 nm. SEM image of a fabricated contact cantilever is shown in Figure 3.9.

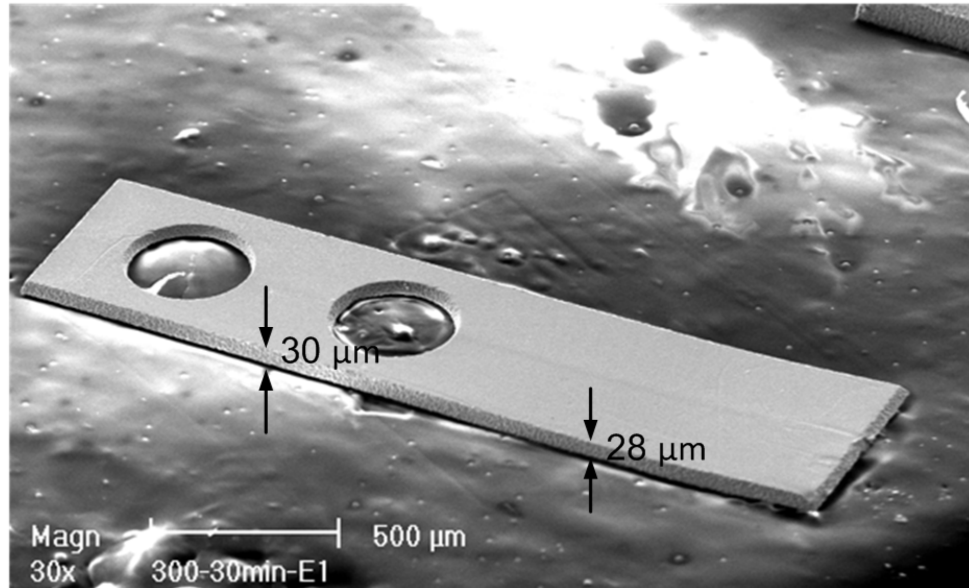

Figure 3.9: Contact cantilever SEM image showing machined recess for contact gap

The actuation cantilevers were also fabricated using µEDM from hardened Al alloy 3003, using 250-µm thick stock foil. Lower purity (99%) Al alloy was used in order to minimize cost. Compared to stainless steel, the higher thermal conductivity of Al can help dissipate heat. Initially, these cantilevers were machined down to 230 µm thickness. The pull-in electrode, and mid-section, where *hole-2* is located, were further reduced in thicknesses down to 120 µm and 30 µm, respectively. The perforations, *hole-1* and *hole-2* were then machined, similar to the perforations on the contact cantilevers. The heat sinks were fabricated using µEDM from 500-µm thick Al alloy 3003 foil. The gap between the fins was defined not only by the diameter of the serial tool but also by that of microsphere. Figure 3.10 and Figure 3.11 show SEM images of fabricated actuation cantilever and heat sink, respectively.

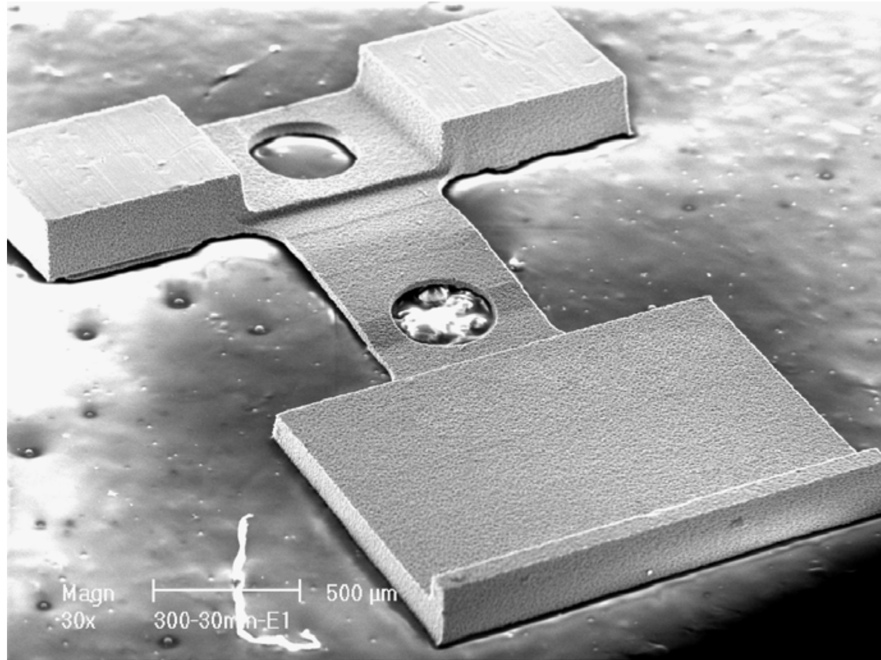

Figure 3.10: SEM image of the actuation cantilever standing upside down

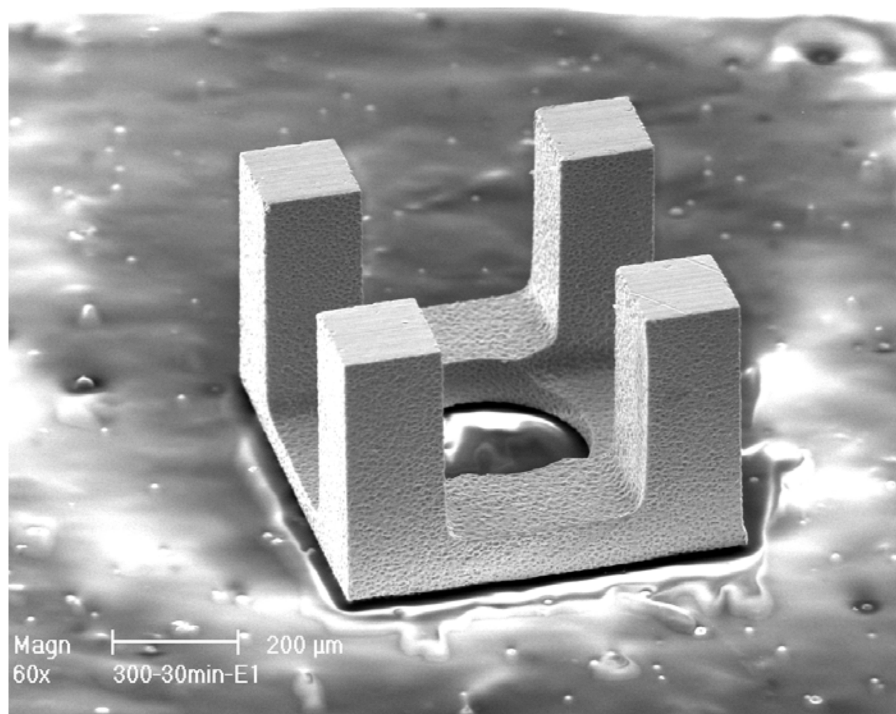

Figure 3.11: SEM image of the heat sink

For the device assembly, gold wire alignment posts (1750 μm height; 300 μm diameter), were fitted into the PCB vias (Fig. 3.12(a)). Conical tip shapes allowed easy

insertion and assembly. The length of the posts was designed to extend above the PCB trace by approximately 60 μm, to precisely accommodate the cantilevers. For the attachment of the contact cantilever to the electrically floating anchor pad, thermally conductive epoxy was manually applied through a syringe around the alignment posts to ease heat dissipation through the posts (Fig. 3.12(b)). Subsequently the actuation cantilever was assembled on top of the contact cantilever and attached to the substrate using high temperature epoxy (Cotronics Duralco 4703, 650 K rated) (Fig. 3.12(c)). The sapphire microsphere was inserted through *hole-2* on the actuation cantilever and attached to the contact cantilever underneath with thermally conductive epoxy (Fig. 3.12(d)). The heat sink was placed on top of actuation cantilever, surrounding the microsphere, and was secured by thermally conductive epoxy (Fig. 3.12(e)). The flatness of the cantilevers was maintained during the assembly process by monitoring the tip height by a high resolution laser displacement sensor (Keyence LK-G32, 50 nm resolution) and adjusting to ensure that the cantilever tip was at the desired height from the ground electrode during epoxy curing. It is envisioned that in the long term, this process can be replaced by a precision pick-and-place process, or eliminated entirely by a lithographic manufacturing method.

A total of nine devices were fabricated and assembled. The distribution is as follows: four devices (two with SS316L contact cantilever and two with Pt-Rh contact cantilever) were used for electrical characterization; two devices (both with Pt-Rh contact cantilevers) were used for thermal characterization; two devices (one with SS316L contact cantilever and one with Pt-Rh contact cantilever) were used for energy dispersive

X-ray spectroscopy (EDX); and one device (with Pt-Rh contact cantilever) was used for a preliminary measurement of hysteresis and lifetime.

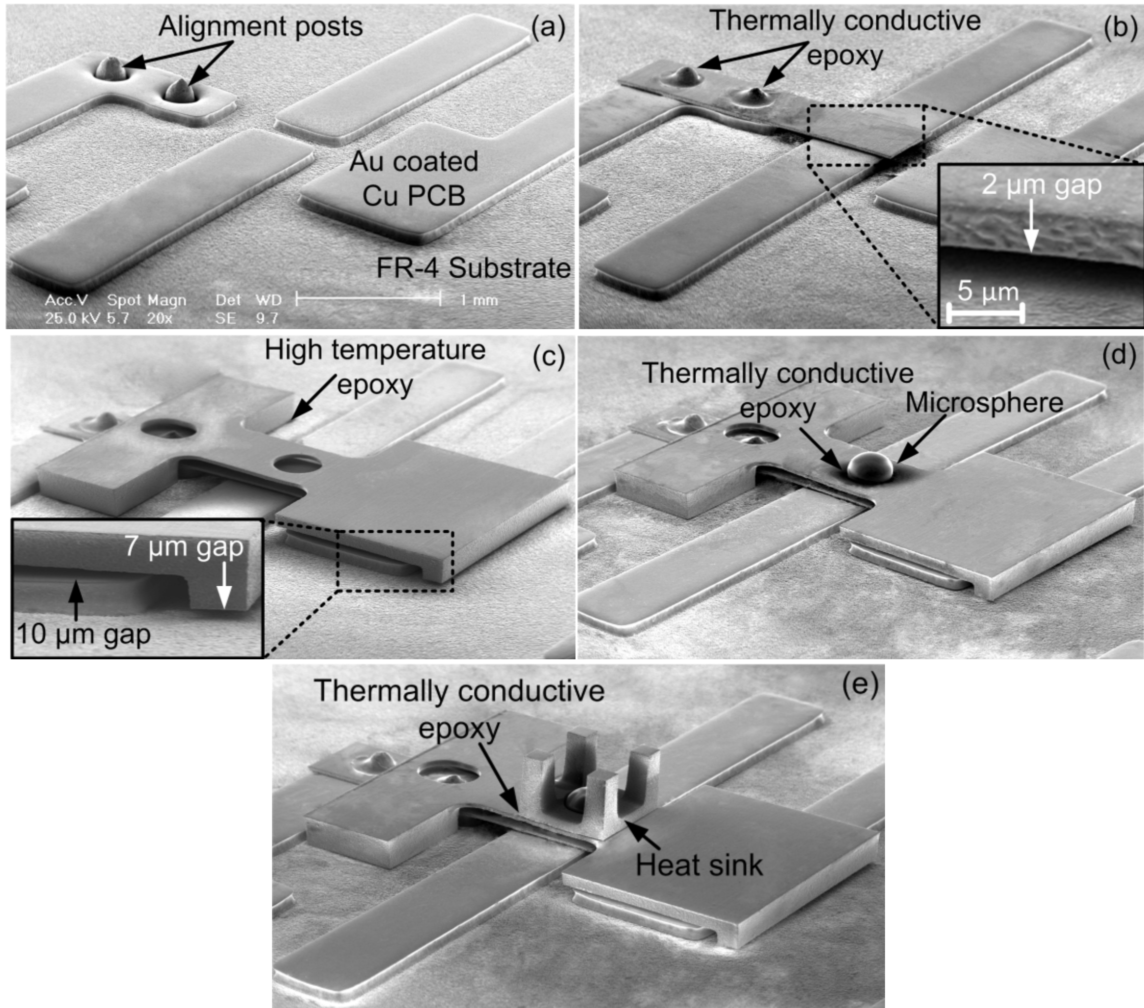

Figure 3.12: SEM micrographs of assembly sequence for all-metal micro-relays showing: (a) floating anchor with alignment posts inserted. (b) Contact cantilever (Pt-Rh or SS316L) aligned on top of the posts through perforations and anchored with thermally conductive epoxy. Contact gap of 2 µm is shown. (c) Actuation cantilever directly placed on PCB substrate. Stand-off tip prevents electrostatic pull-in. (d) Microsphere inserted into the hole-2, secured with thermally conductive epoxy. (e) Heat sink placed by aligning the center hole around the microsphere, fixed with epoxy.

3.3. Experimental evaluation

3.3.1. Electrical testing

The test circuit and the actuation concept for the micro-relay are shown in Fig. 3.13(a). The inputs include the actuation voltage (V_G), the electrical ground, and the line current (I_{ON}), which is separately supplied by a current source (limited to 10 V compliance). In the figure, framed voltages represent indicators. The isolation of the actuation cantilever is monitored by V_{ISO}. Under normal operation there is no current flow across isolation resistor, R_{ISO} (20 kΩ), which is placed between V_G, the cantilever actuation voltage supply, and the actuation cantilever. Therefore, in the absence of a short circuit, V_G and V_{ISO} are normally the same (Fig. 3.13(b)). If the actuation cantilever is shorted to the contact cantilever or to the ground electrode, a leakage current will generate a voltage drop across R_{ISO}, hence result in a V_{ISO} lower than V_G. Similarly, V_{FLOAT} is monitored for voltage fluctuations in the floating anchor pad. V_S is used to extract the total series on-state resistance, R_{ON}. When the micro-relay is off, V_S is 10 V due to the current source limit (and is denoted by V_{S-OFF}). When the device is turned on, V_S is reduced sharply (and is denoted by V_{S-ON}). R_{ON} can be extracted from V_{S_ON} by dividing it by I_{ON}. R_{ON} is a sum of the contact resistance, cantilever resistance and resistance of the signal lead transfer points at the anchor regions.

The tests were conducted in nitrogen ambient (50.7 KPa vacuum) and repeated for both Pt-Rh and SS316L devices. The electrical tests were intended primarily at determining the maximum allowed by the materials and structure.

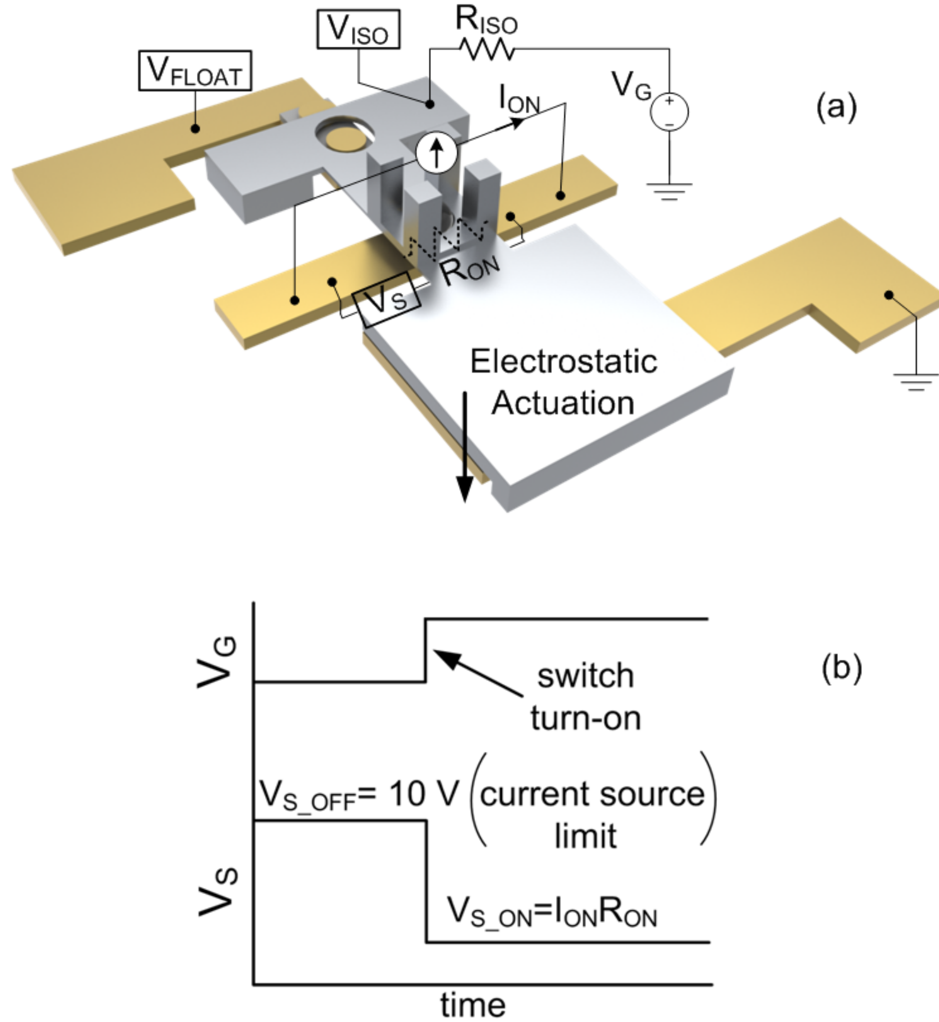

Figure 3.13: (a) Circuitry for device testing, using actuation voltage (V_G) and line current (I_{ON}) inputs. (b) Actuation concept showing $V_{S\text{–}OFF}$ and $V_{S\text{–}ON}$ conditions. V_{FLOAT} is always near 0, whereas V_{ISO} is equal to V_G.

Vertical displacement at the tip of the actuation cantilever was recorded using Keyence LK-G32 laser displacement sensor. The voltage was swept from 0 V to 170 V and back to 0 V to observe the hysteresis (Fig. 3.14). The typical pull-in voltage was around 130 V, slightly larger than the designed value of 120 V. The switching times were approximately 14-15 ms. The turn-off voltage was typically 60 V; this was used to determine the device spring constant. During the release, electrostatic force and mechanical restoring force are equal in magnitude, assuming adhesion and van der Waals

adhesion forces are neglected and there is no self-actuation. The spring constant can then be extracted using following equation [Reb03]:

$$F_{el} = F_k \Rightarrow k = \frac{1}{2}\frac{\varepsilon_0 W w V_{off}^{\ 2}}{g^2 x} \qquad (3.4)$$

where ε_0 is the vacuum permittivity ($8.85\text{x}10^{-12}$), W and w are length (1200 µm) and width (1100 µm) of the pull-in electrode, respectively. V_{off} is the turn-off voltage (60 V), g is the electrode gap at pull-in (typically 3-5 µm) and x is the displacement $\approx$ 6-8 µm). The resulting spring constant was 70.8 N/m. This value was somewhat larger than the simulated spring constant of 56 N/m. Actuation force and recoil forces are extracted as 6 mN and 3.5 mN from (3.4).

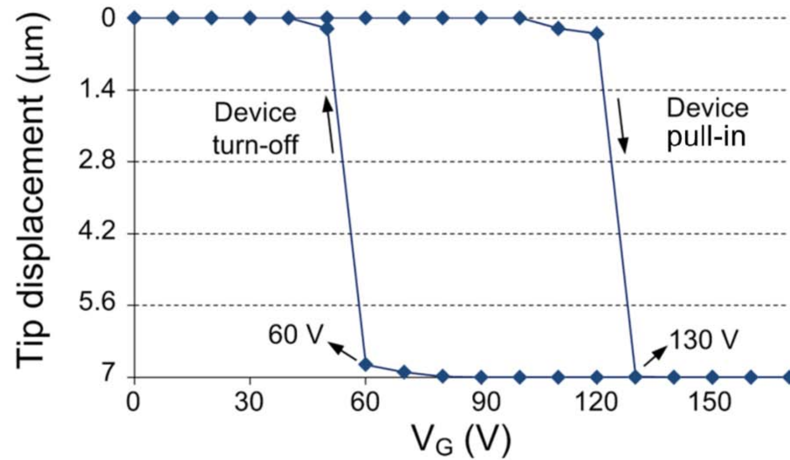

Figure 3.14: Switching sequence showing the hysteresis. Vertical displacement at the tip of the actuation cantilever was recorded using a laser displacement sensor with 0V–170V–0V actuation voltage sweep. Device pull-in and turn-off voltages were 130 V and 60 V respectively. The combined stiffness of pair of cantilevers, heat sink and the microsphere, extracted from these measurements, was 70.8 N/m.

The change of on-state resistance, R_{ON}, with actuation voltage is shown in Fig. 3.15. Increasing V_G increased the actuation force and reduced on-state resistance, *e.g.* 1.4 Ω at 140 V, for Pt-Rh contacts, reduced to 1.25 Ω at 160 V. On-state resistance did not decrease significantly past 160 V. Overall, Pt-Rh devices exhibited lower on-state

resistances than stainless steel devices, probably due to lower electrical resistivity of the Pt-Rh (≈23 μOhm·cm) compared to SS316L (74 μOhm·cm). The on-state resistances of devices with the same contact metal exhibited only minimal variations (on the order of 10 mOhm) from device-to-device. On-state resistances were also monitored with changing line current (Fig. 3.16). For this, V_G was kept constant at 150 V and I_{ON} was increased in 100 mA increments to the point of failure. The R_{ON} did not display major change up to 1.2 A line current for SS316L and 1.5 A line current for Pt-Rh devices. Past these points, resistances for both devices sharply increased. Device failures associated with microwelding occurred at 1.8 A and 2.6 A for SS316L and Pt-Rh contacts, respectively.

3.3.2. Thermal testing

Thermal tests included evaluation of Pt-Rh micro-relays under unforced and forced air cooling conditions. A preliminary assessment of the thermal conditions for the Pt-Rh micro-relay was performed by measuring the contact temperature at the end of each 1 s actuation time period during which varying levels of current were maintained. Tests were performed in 50.7 KPa nitrogen for both unforced and forced cooling cases. A constant actuation voltage, V_G, of 150 V was applied during the tests.

The measurements were performed with the T type Perfluoroalkoxy (PFA) insulated thermocouple (OMEGA Inc., 15 cm length, 70 μm exposed tip diameter); the manufacturer-specified thermocouple tolerance was ±0.5 K. For measurements, the tip of the thermocouple wire was brought in close proximity to the contact area and pressed against the signal line. The room temperature was 300 K during these tests. For forced cooling experiments the mini-fan was located approximately 1 mm above the device.

The flow was forced upward from the device. (The flow rate was not experimentally verified at the operating pressure of 50.7 KPa. As noted previously, the flow velocity at atmospheric pressure was 0.22 m/s.)

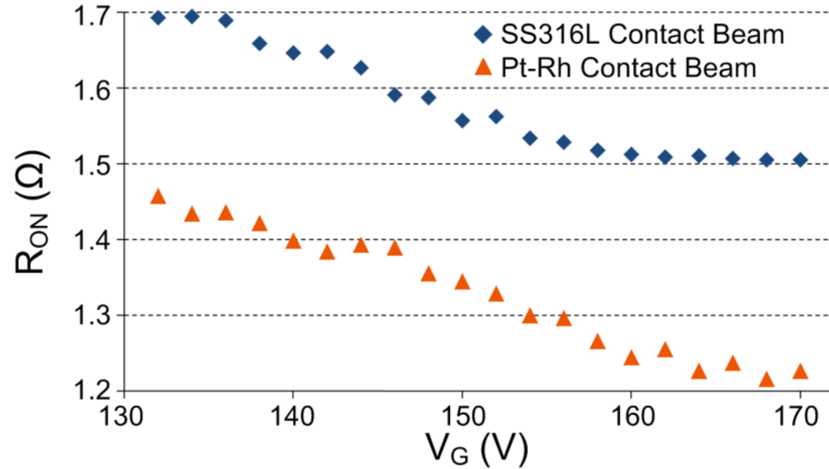

Figure 3.15: Experimental results showing change of on-state resistance with actuation voltage. Line current I_{ON} was kept constant at 1 A. Increase of V_G yielded higher contact force on signal line hence lower on-state resistance. Pt-Rh devices accommodated lower on-state resistance.

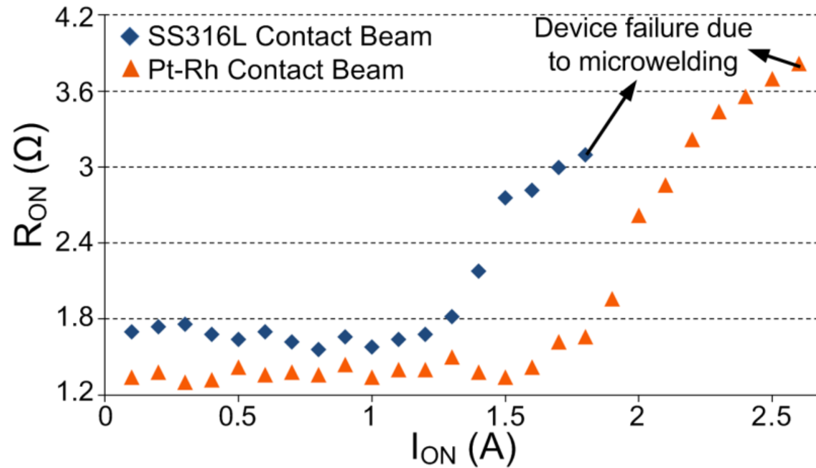

Figure 3.16: On-state resistance derived from I-V curve. R_{ON} is shown for a contact line current up to 2.6 A (in 50.7 KPa nitrogen, unforced cooling). Actuation voltage V_G was maintained constant at 150 V. Resistances augmented sharply past 1.2 A and 1.5 A of I_{ON} for SS316L and Pt-Rh contacts respectively due to softening at contact asperities. Microwelding failures due to localized heating occurred at 1.8 A and 2.6 A for SS316L and Pt-Rh devices, respectively.

Typical measurements for contact area temperatures (following 1 s into the on-

state) of the Pt-Rh micro-relay are shown in Fig. 3.17. The impact of forced cooling is evident: e.g., for 2 A line current, unforced cooling on the micro-relay resulted in 408 K contact temperature, whereas forced cooling suppressed contact temperature rise by at least 20 K. Devices with forced cooling exhibited higher current handling (2.8 A).

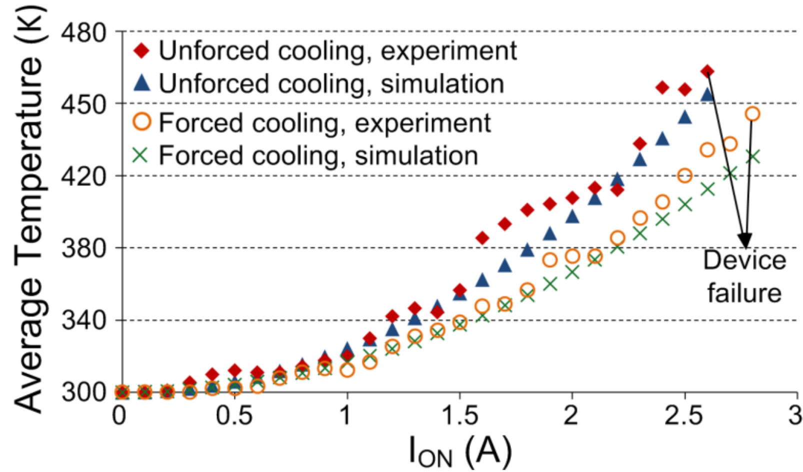

Figure 3.17: Contact temperature for the Pt-Rh micro-relays subjected to unforced and forced cooling in vacuum nitrogen (50.7 KPa) after 1 s on-state operation at varying current levels. Experimental data was compared with simulations. Device failure due to microwelding occurred at 2.6 A and 2.8 A for unforced and forced cooling respectively. Heat management with upward forced cooling (compatible with Sunon UF3A3 mini fan, 10x10x3 mm^3 size, 0.22 m/s air flow) yielded lowest temperature.

Micro-relays were disassembled after failure and contact cantilevers surfaces were observed (Fig. 3.17(a)-(b)). Pt-Rh and SS316L cantilevers were microwelded on Au-Ni-Cu layers of PCB due to excessive heating at the contact asperities. Surface material conditions for another pair of contact cantilevers were observed using EDX after only 50 operation cycles at 1 A electrical current, well before failure (Fig. 3.17(c)-(d)). For averaged EDX spectroscopy, regions of interests were chosen as boxes (75 µm x 150 µm) over contact areas. Both SS316L and Pt-Rh contact cantilevers displayed small traces of gold, indicating material transfer in the initial cycles, even at lower powers (Fig. 3.17(e)-(f)).

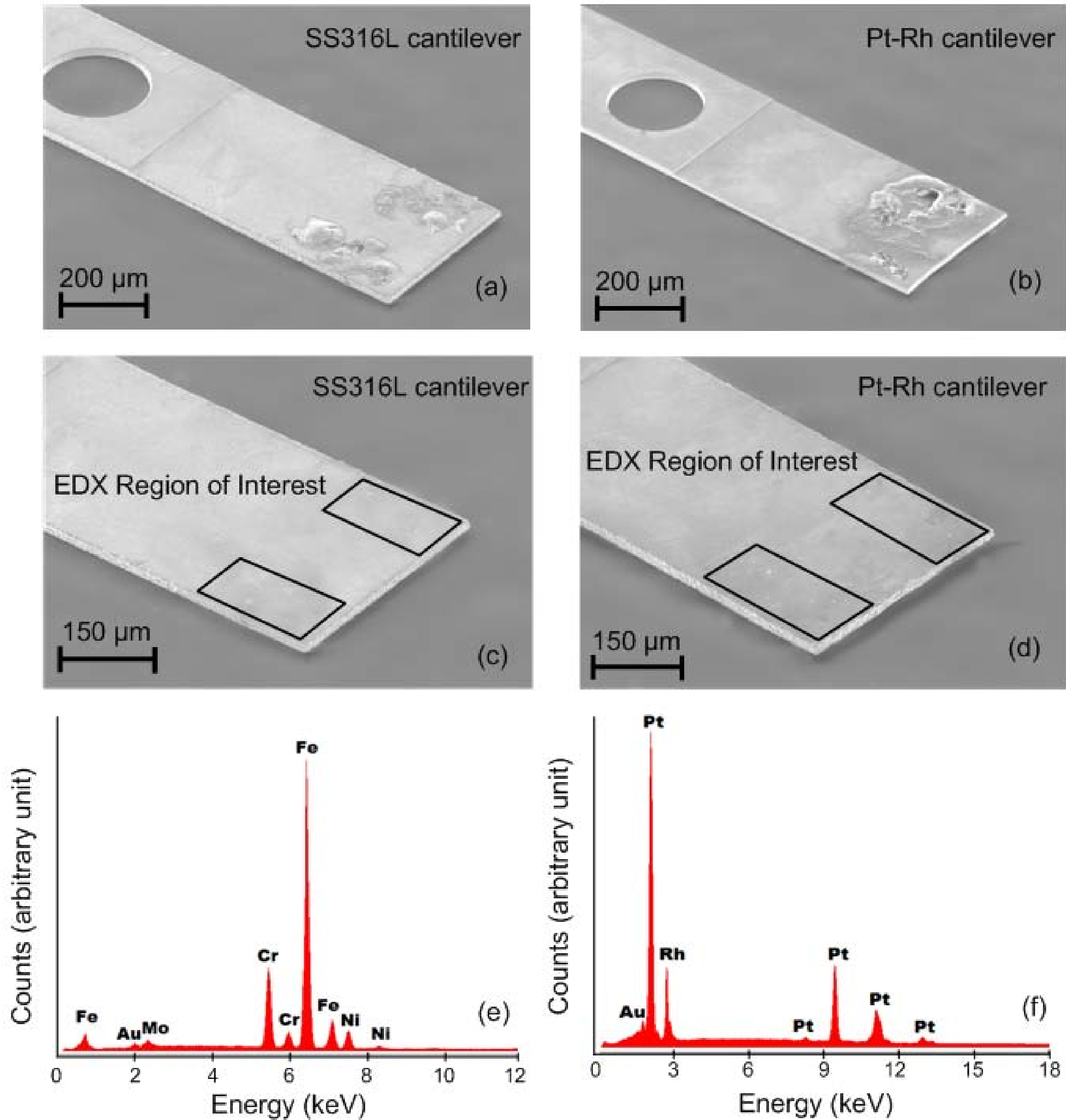

Figure 3.18: SEM micrographs of failed contact cantilevers after disassembly (view from below). Excessive local heating due to high current yielded metal transfer of PCB material on (a) stainless steel and (b) Pt-Rh contacts at 1.8 A and 2.6 A of line current, respectively, and in 50.7 KPa vacuum nitrogen. Energy dispersive X-ray spectroscopy (EDX) was performed on contact cantilevers after 50 operation cycles at 1 A current. The regions of interest for averaged EDX spectroscopy were 75 x 150 µm^2 and enclosed the particles shown on SEM micrographs (c)-(d). EDX spectra for (e) stainless steel and (f) Pt-Rh contacts showed presence of gold.

3.3.3. Lifetime testing

A preliminary evaluation of lifetime of the Pt-Rh micro-relays was performed under hot switching conditions. An electrical line current of 1 A was used and an actuation voltage of 160 V was maintained for the test. The micro-relay was operated at 0.5 Hz frequency with 50% duty cycle. The test was done in nitrogen (50.7 KPa) with the mini-fan kept on all the time. The on state resistance, R_{ON}, was recorded until the device failure occurred. Contact temperatures were also recorded as described in the previous section.

Lifetime test results are shown in Fig. 3.19. The micro-relay operated 2226 cycles before failure. Since the devices were actuated a few tens of times for assembly check purpose before the actual lifetime test, R_{ON} did not exhibit a change for the initial cycles and was constant at 1.2-1.4 Ω for approximately 1900 cycles. A drastic increase in the on-state resistance was observed past 1900 cycles and R_{ON} was approximately 15 Ω at failure. The figure also shows the contact temperature, which remained stable below 2000 cycles, but sharply increased past 440 K near the point of failure.

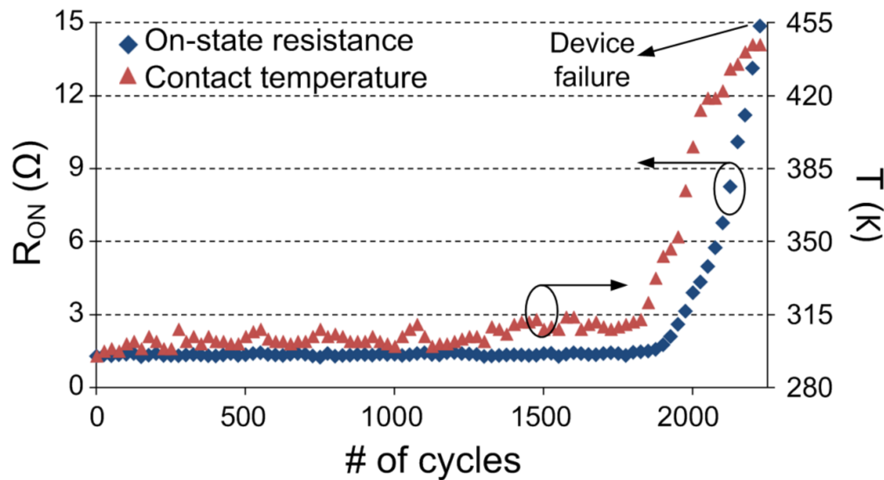

Figure 3.19: Lifetime characterization of the micro-relay. Hot switching test was run in nitrogen (50.7 KPa) with 1 A line current and 160 V actuation voltage. The frequency was 0.5 Hz and duty cycle was 50%. A drastic change in on-state resistance was observed past 1900 cycles leading to failure in the 2226th cycle. The corresponding contact temperatures are also shown. At device failure the contact temperature recorded was 443 K.

3.4. Discussion and conclusions

Electrostatically actuated micro-relay test structures for high power DC applications were evaluated in this paper. Pt-Rh alloy bulk foil was evaluated as the structural contact material for its inert nature and its resistance to softening and wear. The contact metal to mate with Pt-Rh was Au because of its widespread use in PCB manufacturing. A contact pair solely based on Pt-group metals is expected to be susceptible to frictional polymerization, i.e. the formation of a contaminant film due to absorption of organic vapor from the air under fretting conditions with shear or normal force [Rea09, Abb78]. The use of Au with Pt-group metals is known to alleviate the effects of this phenomenon significantly [Ant82]. EDX spectroscopy suggests that some portion of Au top layer is transferred onto contact cantilevers after 50 operation cycles with 1 A electrical current. This phenomenon indicates that contacting SS316L/Pt-Rh and Au pairs potentially contributes to the net reduction of contact resistance.

The micro-relay contact resistance was estimated both theoretically using Holm's permanent deformation model and empirically via a force gauge experiment. For 2.2 mN total contact force and Pt-Rh contact cantilevers, Holm's method suggested 620 mΩ contact resistance with an α-spot of 241 nm radius. This α-spot represents multiple spots that are actually present over the large nominal contact area. The empirical measurement, on the other hand, resulted in a contact resistance of 0.8 Ω which estimates 186 nm radius α-spot. The difference between theoretical and empirical estimates can be attributed to the surface conditions of the machined cantilever.

In normal operation, the on-state resistance, R_{ON}, was a sum of the contact resistance, cantilever resistance and resistance of the signal lead transfer points at the

anchor regions. At high currents (>1 A), the measured on-state resistances were approximately 1.5 Ω and 1.25 Ω for SS316L and Pt-Rh micro-relays, respectively. Measured on-state resistances were higher than empirically estimated 0.8 Ω (for Pt-Rh micro-relays). This is likely due to the parasitic resistances contributed by the cantilever and transfer points, as noted above. Overall, the on-state resistance of the micro-relays was higher when compared to DC relays intended for low power handling. In one case, a 1-Ω contact resistance was reported for an 80 mA current [Li00]; in another case a 35-mΩ contact resistance was reported for 20 mA [Won00].

Failures due to localized heating occurred at 1.8 A and 2.6 A for SS316L and Pt-Rh devices, respectively. The early failure of SS316L micro-relays compared to Pt-Rh micro-relays has two potential reasons. First, the larger electrical resistivity of SS316L leads to greater joule heating, which, in turn, increases the temperature that contributes to failure. Second, the thermal conductivity of SS316L is about 16 W/m·K whereas that of Pt-Rh is approximately 35 W/m·K [Pre60]. Therefore, the contact temperature for SS316L micro-relays will be higher than for Pt-Rh micro-relays, which, in turn, increases the on-state resistance and contributes to an earlier failure. Experimentally measured contact temperatures were overall in good agreement with simulations. Measured temperatures are likely to be higher than simulated ones because of the higher on-state resistance. Pt-Rh devices with forced cooling exhibited a current rating of 2.8 A in 50.7 KPa nitrogen. The use of forced cooling suppressed contact temperature rise by approximately 20 K.

An unpackaged Pt-Rh micro-relay operated for 2226 cycles under hot switching conditions of 1 A line current. This is approximately 10× greater than other high current

DC micro-relays tested at about 100 mA [Kim08]. It is expected that device packaging can further extend the device lifetime.

The test structures evaluated in this study were relatively compact compared to the packaged solid state relays. The current handling was 2-3 times higher than that reported for other DC micro-relays of similar size [Tay98, Won00]. However, on-state resistances were high and actuation times were slow (Table 3.1).

Table 3.1: Device performance summary. Fabricated devices provide small footprint and high current handling.

Property	**Contact Metal**	
	SS316L	**Pt-Rh**
Footprint (mm^2)	6.5 (2.6×2.5)	
Actuation area (mm^2)	1.32 (1.2×1.1)	
Maximum current (A)	1.8	2.8
On resistance (Ω)	1.5	1.2
Actuation time (ms)	10-15	

The main goal of this effort has been to evaluate the power limits of such relays. This chapter has demonstrated the efficacy of bulk metal foils as possible candidates for high power contact relays. Micromachined elements fabricated from stainless steel and Pt-Rh foils are both shown to work; the former may offer a lower cost options whereas the latter offers higher performance.

CHAPTER 4

AN ALL-METAL MICRO-RELAY WITH BULK FOIL Pt-Rh CONTACTS FOR HIGH POWER RF APPLICATIONS

This chapter describes the performance of electrostatically actuated, three-terminal high power RF micro-relays that utilize a cantilever, a contact bridge, and an on-device heat sink [Ozk11]. The design of RF micro-relays requires substantial considerations and extensive modeling which differ from DC micro-relay design considerations. For the micro-relay presented in this chapter, the RF design goals included DC-10 GHz operation bandwidth with down-state insertion loss and up-state isolation better than -0.4 dB and -15 dB, respectively. Minimizing RF coupling and fringing through an iterative optimization study as well as reducing the up-state capacitance and the parasitic inductances, constituted major challenges in this chapter[1]. Section 4.1 describes the micro-relay design, and Section 4.2 details the fabrication and assembly processes for the device. Experimental evaluation is presented in Section 4.3. These include DC, small-signal and high power RF characterization, thermal performance and lifetime test for the device. Section 4.4 provides discussion and conclusions.

[1]RF design and testing for the device presented in this chapter were carried out with the help of Mr. Sangjo Choi, under the guidance of Prof. Kamal Sarabandi.

4.1. Design

The micro-relay has a three-terminal structure (Fig. 4.1). The design has a footprint of 6.4 mm^2 and it is composed of vertically stacked components directly located and assembled on a printed circuit board (PCB). The PCB uses a Rogers 4003 substrate with Cu/Ni/Au traces for reduced loss at microwave frequencies. The PCB traces have four regions. The first region includes two transmission line segments with 50 Ω characteristic impedance and provides input and output paths for the RF signal. At the end of each line, the terminals accommodate contact regions (200×200 μm^2 each). The second region includes the DC ground. Two types of vias are defined on the DC ground: isolated vias provide the locations for anchoring and assembly purposes, and plated vias short DC and RF grounds. The third region includes an L-shaped electrode for the placement of a DC-blocking capacitor. It also acts as a shield to further reduce the RF signal coupling from the transmission line. The fourth region includes the pull-in electrode; it is used to electrostatically actuate the cantilever. The PCB design is obtained through iterative optimization and sensitivity studies to provide the desired switching RF performance. The simulations are described toward the end of this section.

The stainless steel cantilever is positioned orthogonally with respect to the transmission line and suspended above a break. It defines the device footprint (2000×3200 μm^2, including anchor; 2700 μm suspended length; 50-μm thick). The cantilever is elevated above the pull-in electrode on the PCB by a cantilever spacer (2000×400×110 μm^3). Two identical ground spacers (4000×2350×50 μm^3 each) are stacked on the ground electrode. For electrostatic actuation, an interelectrode gap of 10 μm is maintained between the bottom surface of the cantilever and the top surface of the ground

spacer stack. The actuation electrode size is defined by the trapezoidal overlap area between ground spacers and the cantilever (1.8 mm^2). A pair of gold alignment posts (400 µm height, 300 µm diameter each) perforates and anchors the cantilever spacer and the cantilever to the pull-in electrode and the PCB substrate through tightly fitting into the isolated vias. Another pair of alignment posts with same diameter similarly anchors ground spacers to the ground electrode.

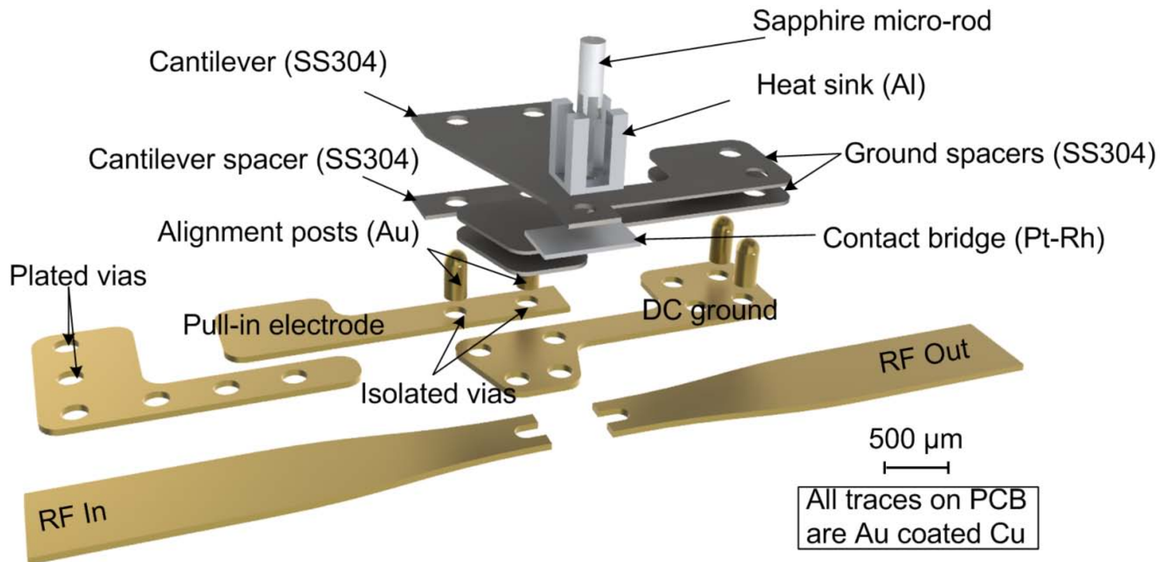

Figure 4.1: Exploded view of the three-terminal micro-relay. Four regions of the PCB are shown. Cantilever and ground spacers, both from stainless steel, are placed to elevate the cantilever above the signal line to define the actuation and the contact gaps. Gold posts align and hold the spacers and the cantilever over the gold-coated copper traces on the PCB. Cantilever pushes the Pt-Rh contact bridge, located at the distal end, via a micro-rod which couples both components. An Al heat sink is integrated atop the point of contact. Device footprint (as defined by the footprint of the cantilever) is 6.4 mm^2.

At the distal end of the cantilever is a multi-level vertically stacked structure. A Pt-Rh contact bridge (600×1000×30 μm^3), provides an ohmic-contact between two open ends of the microstrip underneath. A thermally conductive sapphire micro-rod (700 µm height, 250 µm diameter, 50 $W \cdot K^{-1} \cdot m^{-1}$ thermal conductivity, Meller Optics Inc.) is used to mechanically couple the contact bridge with the cantilever and electrically separate them.

It also performs as a thermal conductor to take the heat away from the contact regions. The micro-rod rests on a 5 µm deep blind hole at the center of the contact bridge and centers the stacked components by perforating the concentric holes on them. The gap between the cantilever and the contact bridge is designed so that the latter stands 12 µm above the transmission line.

A micromachined aluminum heat sink (600×600×1000 μm^3) with 4 fins (each 150x150 μm^2 and 950 µm tall) is used to dissipate local contact heating through active cooling when combined with a commercially available mini-fan (Sunon-UF3A3) placed 1.5 mm above the transmission line. The gap between the fins is defined to allow the location of the micro-rod. Heat sink design follows the principles detailed in [Cim94] and is similar to the one described in Chapter 3. At room temperature (300 K), in air ambient, and for a fin width of 150 µm, the heat loss limit is 4.91. For a fin height of 950 µm, the fin efficiency is 0.876.

Electrostatic modeling of the RF micro-relay was performed in the ANSYS Workbench Finite Element Analysis (FEA) environment. Figure 4.2 shows the displacement and the stress distribution. The model consisted only of the micro-relay and the transmission line. Other electrodes on the PCB were neglected. The “bonded contact” boundary conditions were used for touching surfaces. The “fixed geometry” boundary condition was applied around the alignment posts on the anchor points. For a 12 µm vertical tip displacement, pull-in voltage was 85 V. The finite element analysis results show that the displacement across the 10 µm interelectrode gap over the ground electrode was approximately 4 µm when the contact occurs, therefore pull-in was prevented. The stiffness of the entire micro-relay including the cantilever, the heat sink,

the contact bridge and the micro-rod was 142 N/m. The contact force per contact region was 0.36 mN (with 1.44 mN evenly distributed over four contact regions) for an increased actuation voltage of 130 V. The switching time was 16 ms.

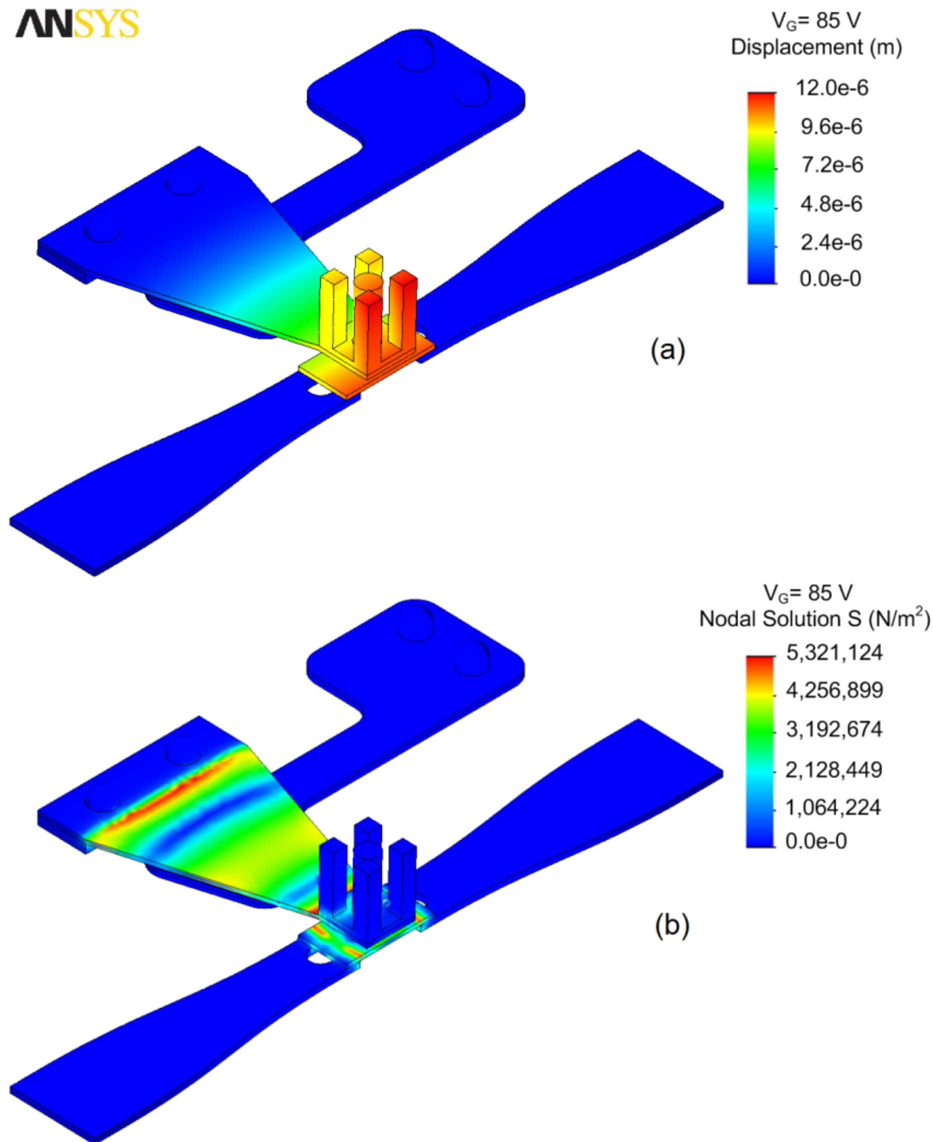

Figure 4.2: Electrostatic FEA for RF micro-relay. (a) Tip displacement was 12 µm as a result of 85 V pull-in voltage. (b) Von Mises stress distribution after the contact. All four contact points had the same stress. Simulated total contact force and actuation time were 1.44 mN (evenly distributed over four contact regions) and 16 ms for 130 V actuation voltage, respectively.

An estimate of the contact resistance is required for two reasons: for accurately modeling S-parameters in High Frequency Structure Simulator (HFSS), and for use as a boundary condition in the thermal model to account for high power joule heating. The contact resistance model is based on Holm's plastic deformation theory, introduced in the previous chapter [Hol68]. The approach for using this model parallels to Chapter 3 so the details are omitted here. A total series contact resistance of 1.09 Ω was analytically estimated for the RF micro-relay, assuming a contact hardness of 6 GPa – the approximate Meyer hardness of Ni, an estimated total resistivity of 30 μΩ·cm for Pt-Rh/Cu/Ni/Au stacked contacts, and 0.36 mN contact force per contact region as noted above. The resulting radius for Holm's α-spot, i.e. single contact spot representing a cluster of multiple small contact spots was 137 nm.

For experimental validation, same technique described in Section 3.1 is used: Pt-Rh beam with the same dimensions as in the proposed design was pressed against the open signal lines on the PCB A precision force gauge (Aurora Scientific, Model 403A) which was mounted on a motorized x-y-z stage, supplied the contact force. The force was applied in 80 μN increments, up to 1.44 mN, over a 1 mm contact diameter. Contact resistance was measured using a 4-wire technique with a 5 mA test current. The total series resistance was 1.34 Ω for 1.44 mN total contact force. The experimentally estimated radius of the α-spot was 111 nm. The empirical contact resistance with changing contact force was compared to the theoretical estimate (Fig. 4.3). The former was larger than the latter by approximately 20%.

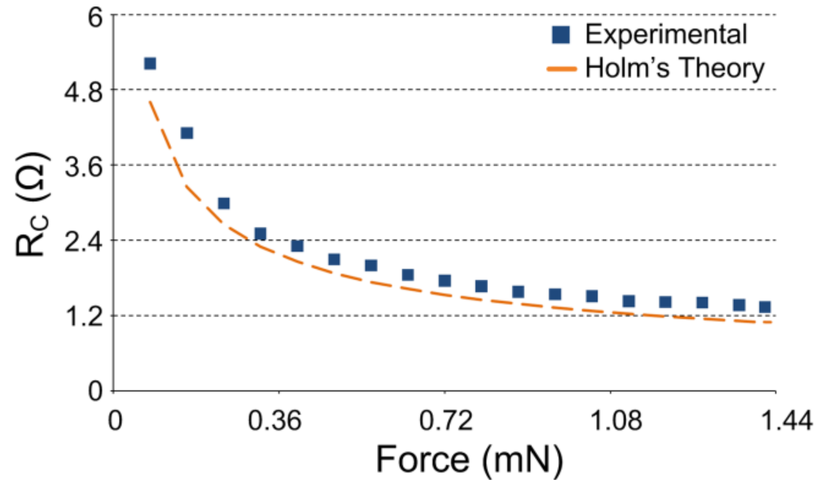

Figure 4.3: Preliminary contact resistance (R_C) estimate for use in the thermal model and in HFSS. Experimental plot showing the change of contact resistance with an increasing force supplied from a force gauge. The force was supplied in 80 μN increments, up to 1.44 mN, distributed evenly on four contacts. The data compared with Holm's contact model. At 1.44 mN total contact force, the experimentally estimated contact resistance was 1.34 Ω whereas Holm's model predicted 1.09 Ω.

The transmission line and the DC electrodes were refined to reduce the RF coupling and the fringing which commonly appear in high frequency RF devices. Geometric optimization involved iterative RF full-wave simulations in HFSS. The simulations were performed for the micro-relay in both the down-state and in up-state. In the down-state, the contact resistance of 1.34 Ω was used as a lumped element. The electric field distribution at 10 GHz guided the geometric modifications depicted in three configurations (Fig. 4.4). In Configuration-1, the DC ground and the pull-in electrode had only isolated vias for anchoring the structural elements; hence, significant coupling was observed between the transmission line, the pull-in electrode, and the DC ground both in the up-state and in the down-state. In Configuration-2, the DC ground electrode was shunted to the RF ground through the conductive plated vias. In addition, the contact pad for the pull-in electrode was flipped horizontally to face away from the input transmission line, and all the electrode corners were rounded to reduce the level of

fringing fields. Although the coupling between the transmission line and the DC ground electrode was reduced significantly, the electric field was not completely suppressed on the pull-in electrode. Configuration-3 was the final layout geometry and included i) the L-shaped electrode which acted as a shield to reduce the coupling from the input transmission line, ii) the fork-shaped open ends which reduced the up-state capacitance and dissipation through the contact bridge and iii) smooth variation of line width for reduced reflection. A 1 pF capacitor was chosen to short-circuit the RF path on the pull-in electrode and acted as a DC-block. The coupling was considerably suppressed both in the down-state and in the up-state.

Figure 4.5 shows the S-parameters for each configuration in the down-state and in the up-state. In the down-state, Configuration-3 resulted in overall better insertion loss and return loss compared to the other configurations at higher frequencies. Similarly, in the up-state, Configuration-3 has return loss better -0.4 dB at 10 GHz whereas the isolation is best throughout the bandwidth.

Thermal modeling of the micro-relay involved the extraction of the electric field distribution at 3 GHz and 30 W of RF power. The contact resistance was included in the model. The solution was then imported into the ANSYS Multiphysics solver to serve as the boundary condition. These values were chosen due to the experimental limits. The thermal adhesive between micro-rod, cantilever and heat sink was modeled as shell with a thermal conductivity of 5 W/m·K following the specifications of commercially available epoxy (Aavid Thermalloy). Contact temperature modeling considered two on-state times: 1 s and 20 s. Forced cooling was assumed in the model; previously determined upward air flow rate of 0.22 m/s was assumed to exist in an imaginary tube

enclosing the contact bridge and heat sink (1.5 mm height, 1 mm diameter). Figure 4.6 shows a temperature increase of approximately 185 K on contacts for 30 W of RF power that was continuously transmitted for 1 s in an unforced cooling setup. The simulation showed that forced cooling reduces the contact temperatures by approximately 25 K.

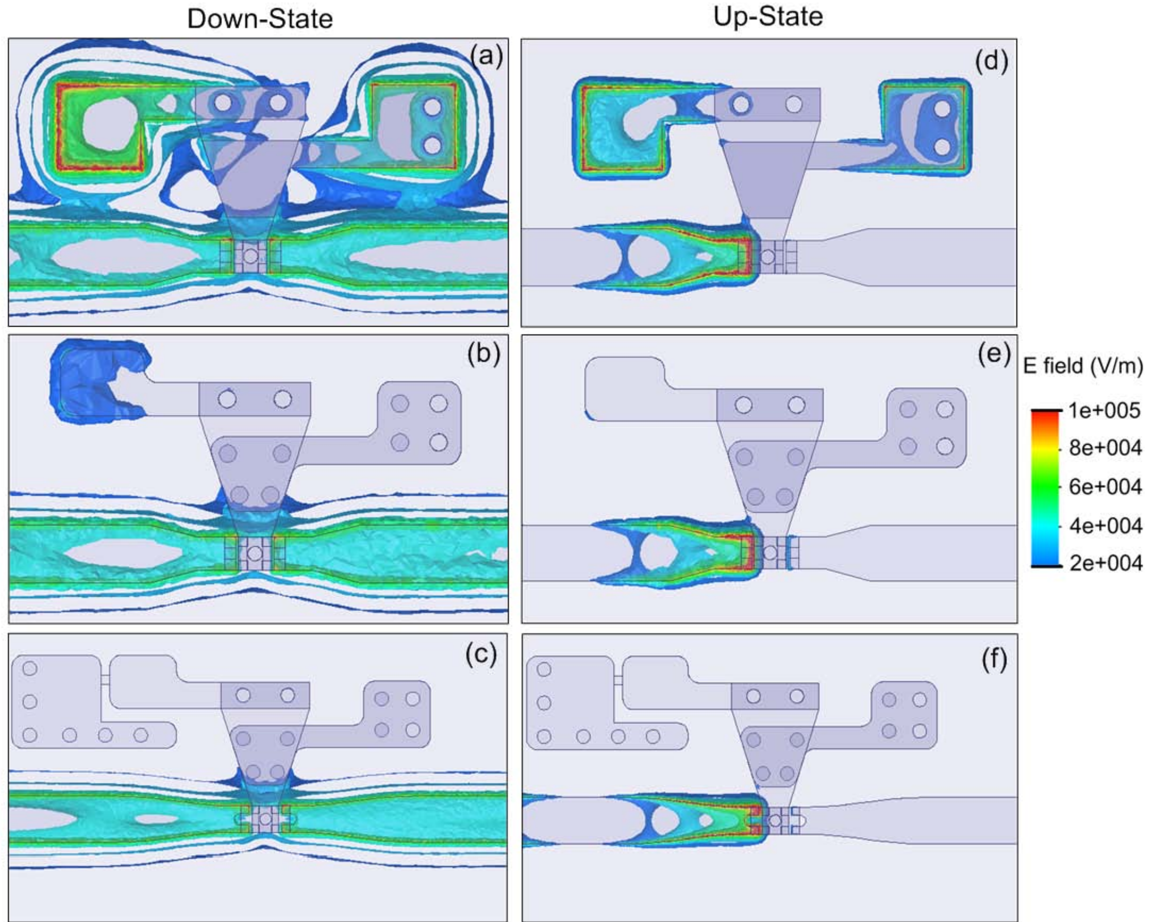

Figure 4.4: Electric field distribution at 10 GHz for three configurations in (a-c) the down-state and in (d-f) the up-state. (a,d) In Configuration-1, the DC ground electrode had no plated vias. (b,e) In Configuration-2, the DC ground electrode had plated vias shunted to RF ground. In addition, the corners of the electrodes were rounded and the contact pad for the pull-in was flipped away from the transmission line. (c,f) In Configuration-3, the L-shaped electrode was placed next to the pull-in electrode and shunted to the RF ground through plated vias. A 1 pF DC-blocking capacitor was assumed. The transmission line was designed to have smooth variation of width. In addition, it had fork-shaped open ends to reduce the capacitance with the contact bridge and the dissipation through it. Configuration-3 provided an electric field distribution with minimized coupling to DC ground and pull-in electrode.

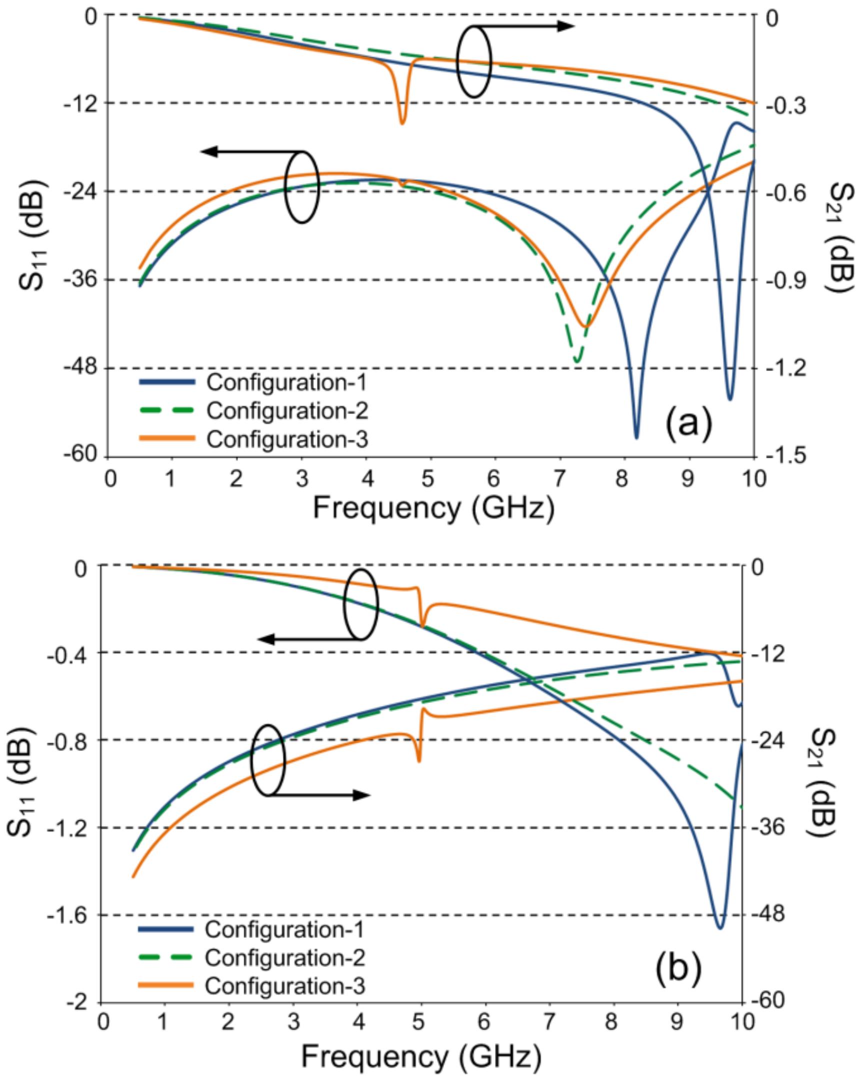

Figure 4.5: Full-wave HFSS simulation results showing S-parameters for three-configurations. (a) In the down-state, Configuration-3 provides the best insertion loss and return loss at higher frequencies. (b) In the up-state, Configuration-3 presents return loss better than -0.4 dB at 10 GHz. The isolation is also better than the other configurations by about 4 dB over the bandwidth.

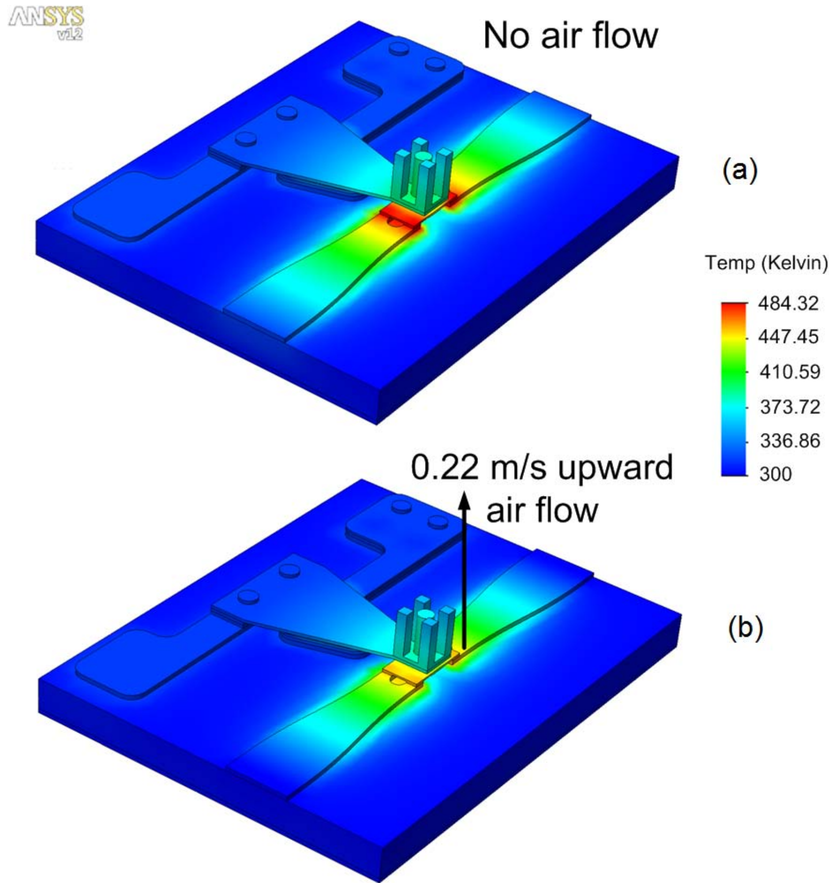

Figure 4.6: Multiphysics electrothermal FEA results for 1 s into the on-state. The HFSS high power electric field distribution was imported to ANSYS as a boundary condition for joule heating. Contact area temperature distribution for (a) unforced (b) forced cooling (3 GHz, 30 W incident RF power, 1.34 Ω modeled contact resistance, 300 K ambient temperature, 0.22 m/s upward flow).

4.2. Fabrication and assembly

For the micro-relay, the contact bridges were serially fabricated using μEDM in high purity Pt-Rh (Alfa Aesar Corp., 80:20 concentration, 99.99% purity) down to 30 μm final thickness using 50-μm thick stock metal foils. The lowest available discharge energy of 24.5 nJ was used at contact bridges to ensure smooth surface finish. Surface roughness on the bottom, unmachined, side of the contact bridges was measured using Zygo NewView 5000 interferometer. Average roughness R_a was approximately 25 nm.

The heat sinks were also fabricated using µEDM from 1 mm-thick Al 3003 alloy foil (99% purity). The discharge energy was increased to 16.5 µJ for faster machining of the fins. A through hole of 250 µm diameter was machined at the base of the heat sink for the subsequent assembly of the micro-rod and the contact bridge.

The cantilever spacer was also fabricated using µEDM down to 110 µm thickness from 125 µm-thick stainless-steel (SS304) stock foil. For each micro-relay, two perforations of 300 µm diameter were positioned on the cantilever spacers to allocate the alignment posts for the attachment to the cantilever, and to the pull-in electrode below.

The cantilever and the ground spacers were photochemically machined from 50 µm-thick SS304 foils (Kemac Technology Inc., CA). Two perforations of 300 µm diameter were located on the cantilever for the assembly over the cantilever spacer and the PCB, whereas another perforation of 250 µm diameter was situated towards the tip of the cantilever for subsequent assembly of the contact bridge, the micro-rod and the heat sink. Similarly two perforations of 300 µm diameter were positioned on the ground spacers for the attachment to the ground electrode.

A 500 µm-thick Rogers 4003 was used as the substrate for the RF transmission line (Advanced Circuits Inc., CO). Cu traces (70 µm-thick) provided the bias electrodes and the surface microstrip. In such PCBs, 4 µm-thick Ni was used as an adhesion layer on the Cu base, and 0.15 µm-thick outer gold layer provided a low resistivity electrical contact. Cu/Ni/Au metal tracing with the same thicknesses was used on the plated vias whereas isolated vias were left unplated.

Alignment posts were fabricated using µEDM from 300 µm diameter gold wire, and tightly fitted into the isolated vias on the PCB (Fig. 4.7(a)). Conical wire tips

facilitated the alignment and the insertion of the perforated components. The cantilever spacers and the ground spacers were assembled over the posts (Fig. 4.7(b)) and fixed by applying an electrically conductive epoxy (Creative Materials, volume resistivity: 300 μΩ-cm). The assembly of the cantilever and the heat sink followed this (Fig. 4.7(c)). The heat sink was attached onto the cantilever by aligning the perforation at its base to the one on the cantilever tip, and securing with high temperature epoxy (Cotronics Duralco 4703, 645 K maximum temperature). The flatness of the cantilever as well as the electrode gap of 10 μm was maintained during the assembly process with the help of a high resolution laser displacement sensor (Keyence LK-G32) raster scanning over the region and giving continuous feedback. The contact bridge was aligned and placed on the transmission line. The sapphire micro-rod was then tightly fitted into the overlapping perforations on the heat sink and the cantilever. It rested on the blind hole at the center of the contact bridge, further aligning it for a precise contact. High temperature epoxy was applied to fix the parts (Fig. 4.7(d)).

A total of five devices were fabricated and assembled. The distribution of those devices is as follows: one device for DC on-state resistance characterization and hysteresis study; one device for small-signal characterization; two devices for high power testing and for thermal characterization; and one device for lifetime characterization.

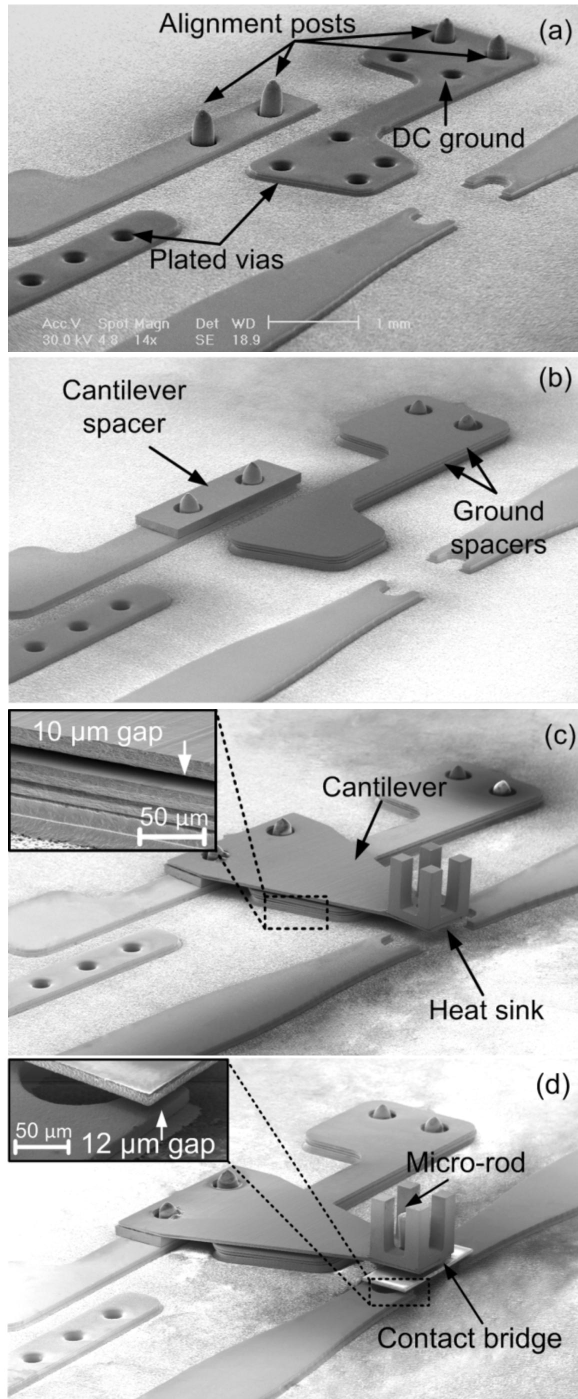

Figure 4.7: Assembly sequence for the RF micro-relay: (a) alignment posts inserted. (b) Cantilever and ground spacers (SS304) aligned on top of the posts through the perforations and anchored with electrically conductive epoxy. (c) The cantilever and the heat sink placed on top. Interelectrode gap of 10 μm and stacked PCB-spacer-cantilever structure are shown in the inset. (d) The contact bridge placed on the signal line and coupled with the cantilever through an embedded micro-rod fixed with epoxy in the mid-section of the heat sink, ensuring uniform contact when actuated. Contact gap is shown in the inset.

4.3. Experimental evaluation

4.3.1. Electrical testing

Electrical testing of the micro-relay consisted of DC, small-signal RF and high power RF characterizations. The actuation concept and the test circuit for the micro-relay are shown in Fig. 4.8(a). The inputs are the actuation voltage (V_G), the electrical ground, and two-port RF in and RF out which were applied on the pull-in electrode, the DC ground electrode, and on the transmission line through SMA type connectors, respectively. RF signal was replaced with a line current (limited to 10 V compliance) for DC ohmic-contact characterization. The cantilever isolation is monitored by voltage V_{ISO}. Under normal operation no current flow across the isolation resistor, R_{ISO} (1 MΩ), is expected. Therefore, V_G and V_{ISO} are normally the same. The leakage current will cause a voltage drop across R_{ISO} if the cantilever is shorted to the DC ground electrode, and result in a V_{ISO} lower than V_G. DC ground was applied on the ground electrode with a 20 kΩ resistor. Testing circuitry also included a 1 pF DC blocking capacitor that was surface mounted between the pull-in electrode and the DC blocking electrode. All the tests were run in air ambient at atmospheric pressure with unpackaged devices.

The on-state resistance of the micro-relay, R_{ON}, was characterized in DC by an I-V sweep. The components of R_{ON} included contact resistance, contact bridge resistance, and the parasitics due to assembly imperfections. The pull-in voltage for the micro-relay was 90 V and the corresponding on-state resistance for tested devices was approximately 11 Ω. R_{ON} was reduced to 1.8 Ω for an actuation voltage of 130 V. Past this point, R_{ON} did not decrease significantly (Fig. 4.9). Turn-on times were approximately 12-13 ms.

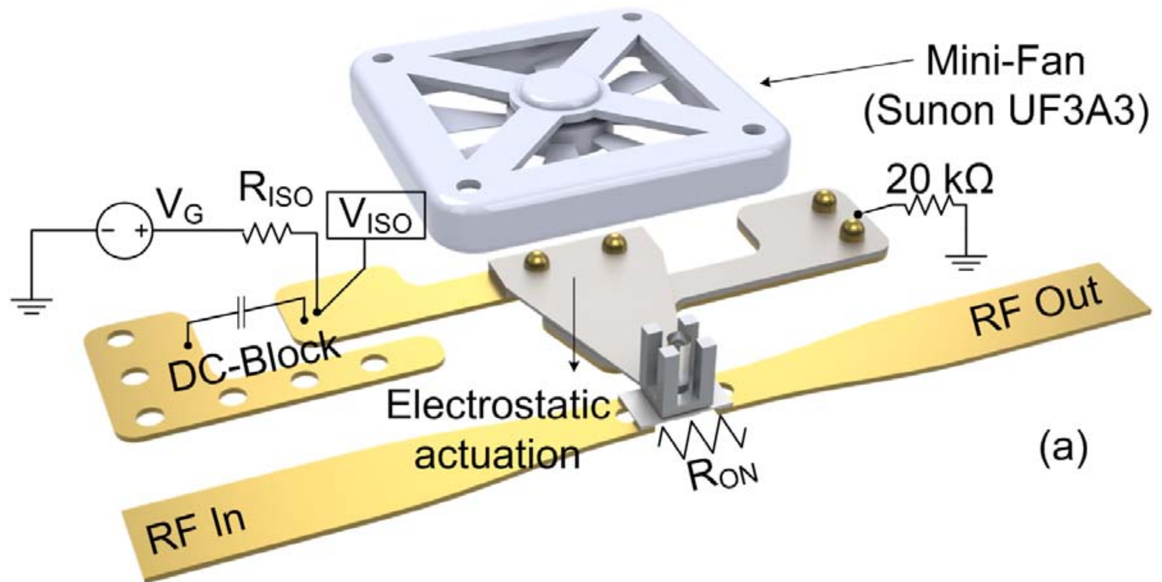

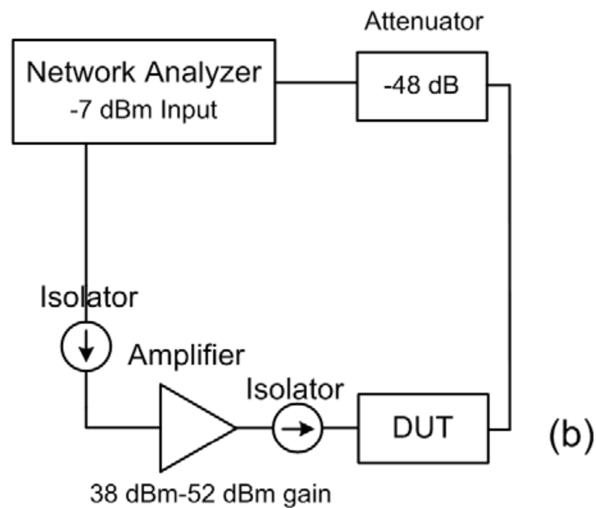

Figure 4.8: (a) Circuitry for testing of three-terminal RF micro-relay. Actuation voltage, V_G was used for the electrostatic actuation. V_{ISO} was monitored to detect any leakage with a 1 MΩ resistor, R_{ISO}, and was always equal to V_G. R_{ON} was the on-state resistance and included the contact resistance, the bridge resistance and the parasitics. A 1 pF surface mount capacitor was used for DC blocking. RF input and outputs were realized via SMA coaxial connectors. (b) High power RF test setup (limited to 30 W of maximum RF power at 3 GHz).

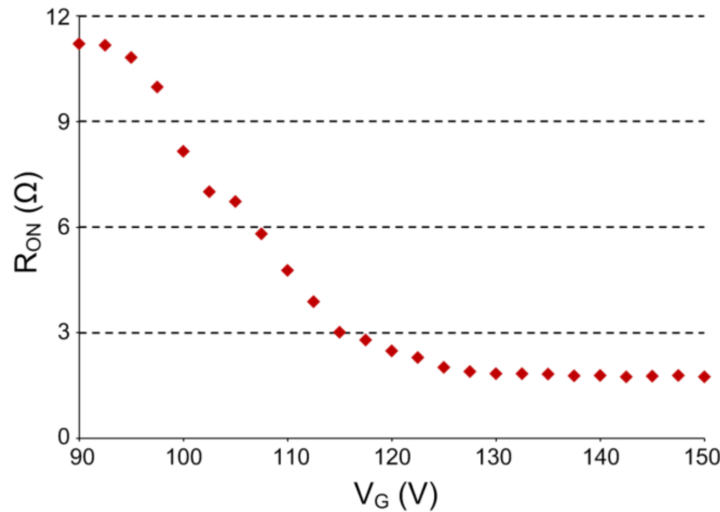

Figure 4.9: Experimental results for micro-relay showing the change of on-state resistance with actuation voltage after a four probe DC I-V test. Pull-in occurred at 90 V. Further increase of V_G yielded higher contact force on signal line hence lower on-state resistance. Contact resistance was approximately 1.8 Ω and did not vary significantly past 130 V.

Figure 4.10 shows the tip displacement of the cantilever under hysteresis condition. The displacement was recorded using the laser displacement sensor. For hysteresis, the voltage was swept from 0 V to 150 V and back to 0 V. The pull-in voltage was around 90 V, in good agreement with 85 V design value. The turn-off voltage was approximately 62 V, indicating that the mechanical spring constant was 159 N/m following equation 3.4. This is slightly larger than the simulated value of 142 N/m, possibly due to structural assembly flaws. Actuation force and recoil forces are extracted as 4.5 mN and 3 mN from (3.4).

Small-signal RF analysis involved experimental characterization of S-parameters at 32 μW power, and comparison to previously performed small-signal analysis for the Configuration-3. In the down-state, characteristic impedance of the contact bridge was 64 Ω (Fig. 4.11(a)). The down-state insertion loss was better than -0.2 dB and -0.4 dB for up to 5 GHz and 10 GHz, respectively (Fig. 4.11(b)). In the up-state, 110 fF

capacitance was extracted from the simulations (Fig. 4.12(a)). The isolation was better than -25 dB and -13 dB up to 5 GHz and 10 GHz, respectively (Fig. 4.12(b)). Overall, experimental data was in good agreement with HFSS.

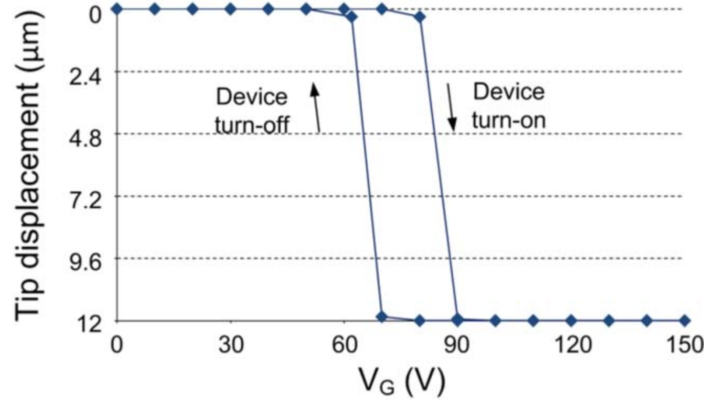

Figure 4.10: Switching hysteresis. Vertical displacement at the tip of the cantilever was recorded using a laser displacement sensor with 0V–150V–0V actuation voltage sweep. Device pull-in and turn-off voltages were 90 V and 62 V, respectively. Device stiffness of 159 N/m was extracted.

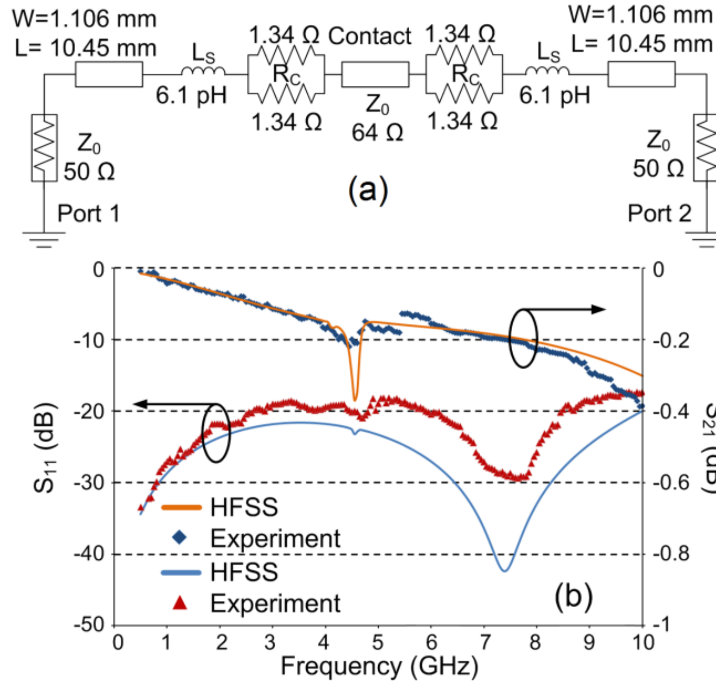

Figure 4.11: (a) Equivalent circuit for the switch in the down-state. An actuation voltage of 130 V was maintained. Characteristic impedance of the contact bridge was 64 Ω. (b) Down-state small-signal analysis for 500 MHz–10 GHz with 32 μW power. Experimental data compared with HFSS. The down-state insertion loss was below -0.2 dB for up to 5 GHz.

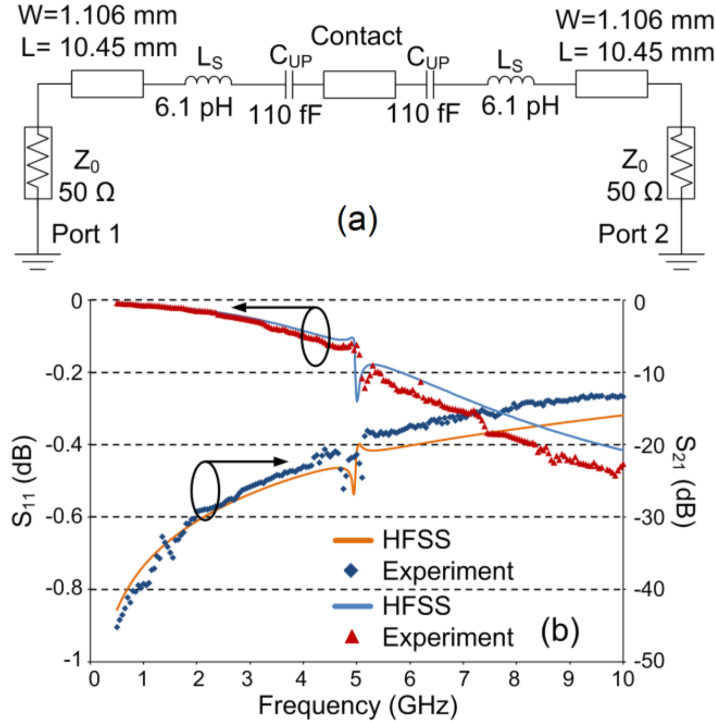

Figure 4.12: (a) Equivalent circuit for the switch in the up-state. Up-state capacitance of 110 fF was extracted from the full-wave simulations. (b) Up-state small-signal analysis for 500 MHz–10 GH with 32 μW power. Experimental data compared with HFSS. The isolation was better than -25 dB up to 5 GHz.

The high power testing setup is shown in Fig. 4.8(b). The test consisted of discrete power sweep through 11 gain levels up to 30 W of incident RF power at 3 GHz which was the amplifier limit (Amplifier Research 30W1000B). Changes in the down-state insertion loss and the up-state isolation were observed under hot switching conditions for two on-state times; 1 s and 20 s. For down-state, V_G was maintained constant at 130 V. During the tests, heat management with upward forced cooling (0.22 m/s air flow) was used by suspending the mini-fan above the device. The effect of prolonged on-state times on S_{21} was observed. For 1 s on-state times, insertion loss in the down-state was better than -0.25 dB for up to 10 W of RF power and it decayed down pass -0.4 dB at around 18.5 W where the device failed due to microwelding. The up-state

isolation was approximately -26 dB over the power sweep range. Only minimal fluctuations were present and self-actuation was not observed (Fig. 4.13(a)). For 20 s on-state times, insertion loss in the down-state degraded noticeably faster to near -0.4 dB at 7 W at which point the device failed. S_{21} similarly remained around -26 dB for up to 30 W and no self-actuation was observed (Fig. 4.13(b)).

4.3.2. Thermal testing

The characterization of the micro-relay contact temperatures was performed with 1 s and 20 s on-state times under the forced air cooling conditions. A preliminary assessment of the thermal conditions was done by measuring the contact temperature at the end of each 1 s and 20 s actuation time periods during which varying levels of RF power were maintained. The thermal and high power testing described previously were carried out simultaneously on the same devices. The measurements were performed using an infrared thermometer (Optris LaserSight, 1 mm laser diameter). The ambient temperature was 300 K. The laser was directed at the contact regions and average contact temperature was measured at the end of each actuation cycle. The experimental results were compared with the thermal model.

Figure 4.14 shows the average contact temperatures. Failures associated with microwelding at 18.5 W and 7 W occurred past 400 K for devices with 1 s and 20 s on-state times, respectively. The experimental results and the thermal model overall agreed well.

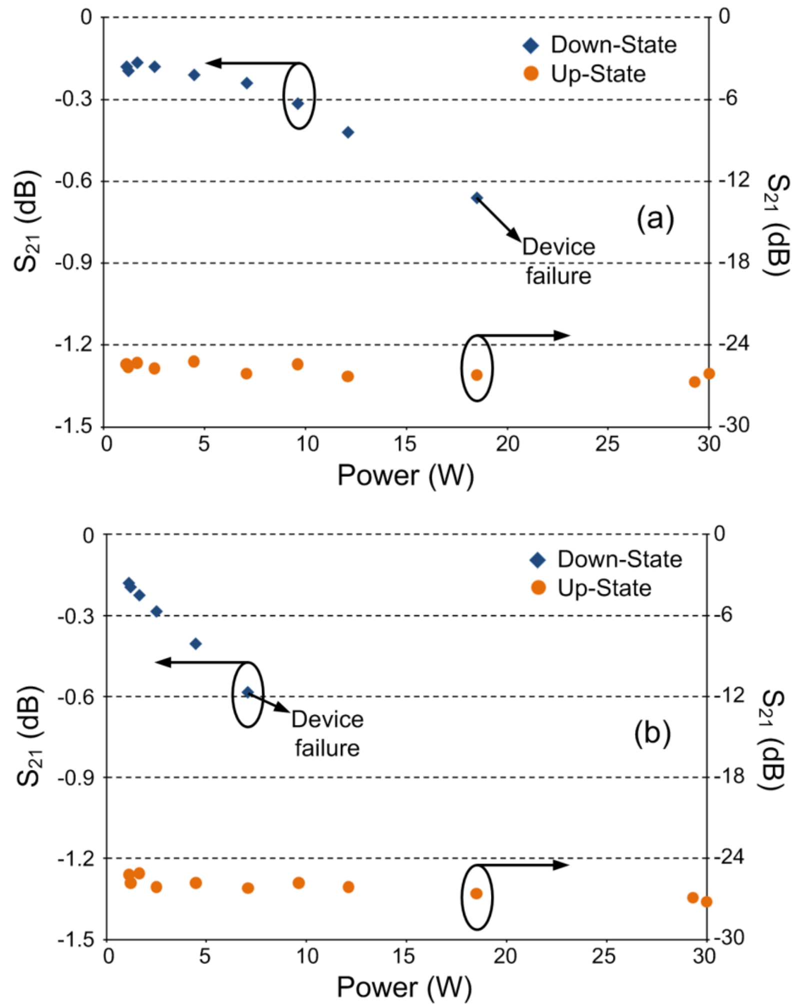

Figure 4.13: High power testing for the RF micro-relay. Tests were realized at 3 GHz and up to 30 W of RF power (test setup limit), at 130 V actuation voltage and in air ambient. Heat management was used throughout the testing with upward forced cooling (compatible with Sunon UF3A3 mini fan, 10x10x3 mm^3 size, 0.22 m/s air flow). (a) Testing with 1 s on-state times. Insertion loss in the down-state was below -0.25 dB for up to 10 W and decayed down pass -0.4 dB at around 18.5 W where the device failure occurred due to microwelding. The up-state isolation was around -26 dB throughout and self-actuation was not observed. (b) Testing with 20 s on-state times. The down-state insertion loss decayed significantly faster down to approximately -0.4 dB at 7 W where microwelding occurred. The up-state isolation was around -26 dB up to 30 W and no failures were observed.

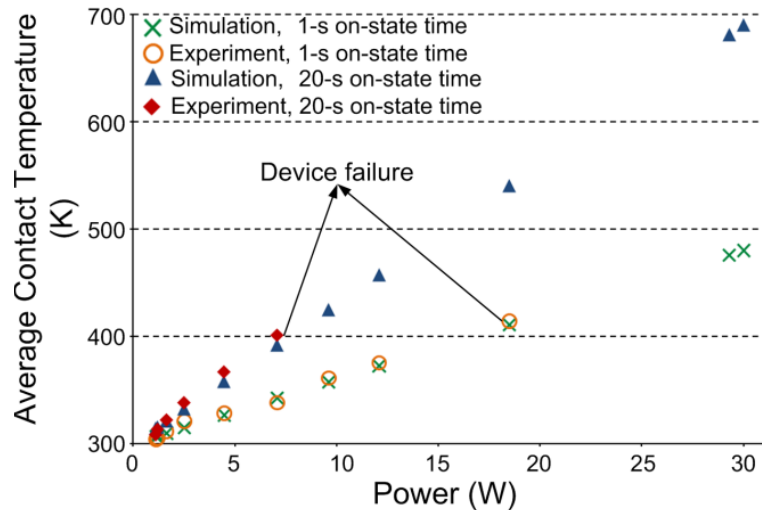

Figure 4.14: Average contact temperature for 1 s and 20 s on-state times in air ambient with the forced cooling. Contact temperatures were measured using an infrared thermometer. Experimental data was compared with the thermal model. The device with 1 s and 20 s on-state times failed at 18.5 W and 7 W, respectively.

4.3.3. Lifetime testing

The lifetime characterization of the micro-relay was realized under the hot switching conditions. Continuous RF power of 1 W was applied at 3 GHz. The micro-relay was operated at 0.5 Hz frequency with 50% duty cycle following 1 s on-state times. Actuation voltage, V_G was maintained at 130 V during the on-state. The test was carried out in air ambient with forced cooling. S_{21} for both the up-state and the down-state was recorded up to the point of device failure. The down-state insertion loss was near constant below -0.2 dB and increased notably past 2800 cycles (Fig. 4.15). The device failure occurred in the down-state at the 3074th cycle with -1dB insertion loss. The up-state isolation was degraded slightly from -26 dB and it was recorded -22.5 dB at the point of failure.

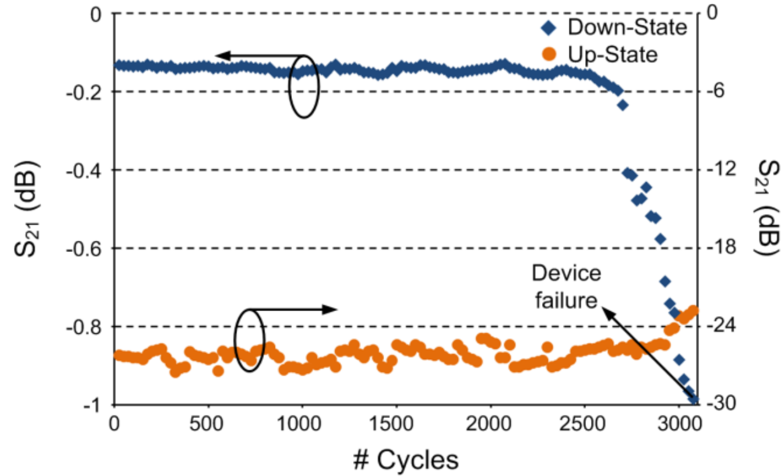

Figure 4.15: Lifetime characterization of the micro-relay. The test was run under the hot switching conditions in air ambient with forced air cooling. Test conditions included 1 W of RF power at 3 GHz and 130 V actuation voltage. The switching frequency was 0.5 Hz and duty cycle was 50%. A drastic increase in the down-state insertion loss was observed past 2800 cycles leading to failure in the 3074th cycle at nearly -1 dB. Isolation was reduced slightly to -22.5 dB at the point of failure.

4.4. Discussion and conclusions

Electrostatically actuated micro-relays with Pt-Rh contacts were directly assembled on a PCB iteratively optimized for RF performance. Unpackaged test structures with 6.4 mm^2 footprints and 90 V pull-in voltage, were tested for small-signal performance and high power handling capability in an air ambient. For small-signal, the down-state insertion loss and the up-state isolation were better than -0.2 dB and -25 dB up to 5 GHz, respectively. Experimental data was in good agreement with HFSS. High power testing was performed for up to 30 W at 3 GHz for both 1 s and 20 s on-state times. Heat management was employed through forced air cooling using a commercially available mini-fan placed above the devices. Elongated on-state times lead to an early device failure. Microwelding occurred in the down-state at 18.5 W and 7 W for 1 s and 20 s on-state times, respectively. No self-actuation was observed in the up-state. It is

envisioned that shorter on-state times can potentially provide higher peak power handling.

The lifetime of an unpackaged micro-relay operating in air was 3074 cycles under the hot switching conditions of 1 W RF power. One of the potential contributors degrading device lifetime is the frictional polymerization introduced in the previous chapter. Device packaging is essential to potentially eliminate this phenomenon and to elongate the device lifetime.

The test structures evaluated in this study were comparable in size with the packaged RF MEMS devices. The power handling was 4×-5× higher than that reported for other RF MEMS relays of similar size [Cou04, Shi07]. Conversely, on-state resistances were relatively high.

The main goal of this effort has been to investigate the RF power handling limits of micro-relays with bulk foil contact elements. Based on the performance of the RF micro-relays described in this chapter, the use of chemically inert and mechanically robust bulk foil alloys such as Pt-Rh appears promising for high power applications.

CHAPTER 5

BATCH FABRICATED HIGH POWER RF MICRO-RELAYS WITH DIRECT ON-PCB PACKAGES

This chapter describes a process for batch mode manufacturing, assembly and packaging of RF micro-relays directly on PCB substrates. A multi-layer PCB design allows for the use of subsurface metal layers to transmit the RF signal into and out of the sealed encapsulation. Challenges addressed in this chapter include the demonstration of batch manufacturing process, device encapsulation, and design optimization of the transmission line to minimize losses due to multi-layer structure[1]. Section 5.1 addresses the micro-relay design. Section 5.2 describes the batch fabrication and assembly process for the device whereas Section 5.3 presents experimental evaluation for DC, small-signal, high power and lifetime characterization. Discussion and conclusions are provided in Section 5.4.

5.1. Design

The packaged batch micro-relays are designed in 4×1 array structures (Fig. 5.1). Individual Pt-Rh contact bridges, detailed later in this section, are located on a Parylene coated 50 μm-thick SS304 cantilever frame which carries four cantilevers. Four gold posts (1 mm height, 500 μm diameter each) align and firmly hold the cantilever frame over

[1]RF design and testing for the device presented in this chapter were carried out with the help of Mr. Sangjo Choi, under the guidance of Prof. Kamal Sarabandi.

cantilever frame support traces on a multi-layer PCB. A liquid crystal polymer (LCP) based lid is used to package the device directly onto the PCB.

The individual micro-relay which is singulated from 4×1 array structures is shown in Figure 5.2. The device footprint, defined by the footprint of the cantilever, is 8.4 mm^2. The cantilever has three distinct regions which are shown in Figure 5.3. The first region includes a slot (1 mm × 250 μm) located towards the anchoring edge which facilitates the fixing of the beam on the PCB. The second region constitutes a recess area of 2.23 mm^2 and 4 μm depth in the middle of the cantilever for the actuation gap, whereas the third region has a recess of 28 μm depth at the distal end, for the placement of the Pt-Rh contact bridge. Parylene deposition is preferred for the electrical isolation of the cantilever from the RF path, due to its excellent insulation properties [Vps11]. A Parylene thickness of 3 μm is chosen. A Parylene-free opening is located on the cantilever to allow for the electrical connection.

A 25 μm-thick rectangular Pt-Rh contact bridge is located inside the 28 μm-deep recess below the tip of the cantilever for the electrical contact. Parylene coating on the cantilever isolates the contact bridge from the DC path. The contact bridge has a through hole of 300 μm diameter in the center for epoxy application during the assembly to the cantilever. Four contact dimples of 40 μm diameter are defined on the contact bridge to electrically short the open ends of the transmission line underneath it. The height of the dimples is designed 10 μm to reduce the capacitance between the transmission line and the contact bridge, hence increase the up-state isolation. The bottom of the contact bridge levels with the cantilever and allows for 3 μm contact gap

as per the Parylene thickness. Figure 5.4 shows A–A’ cross section as noted in Figure 5.2.

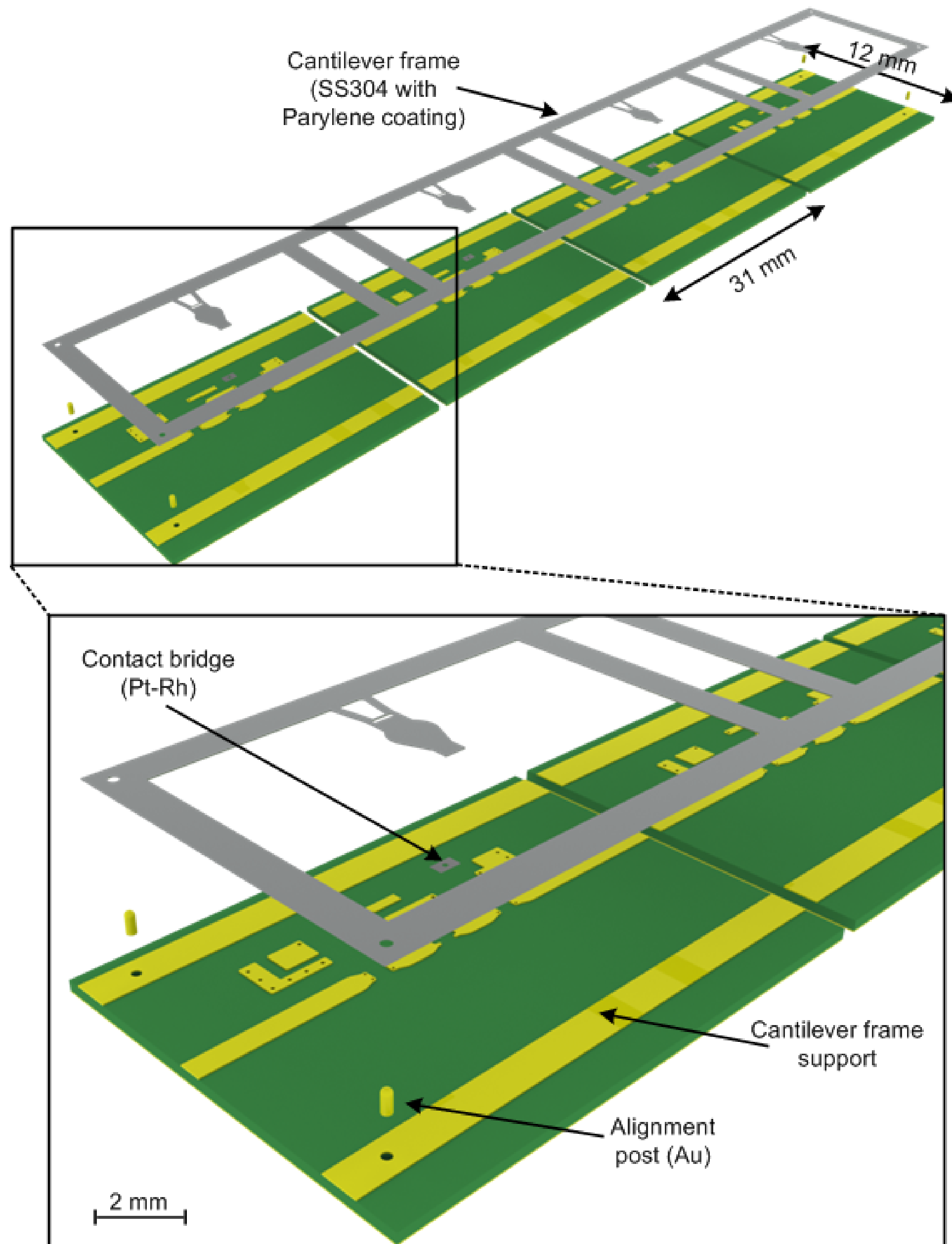

Figure 5.1: Exploded view of the 4×1 array batch micro-relays. Individual Pt-Rh contact bridges are placed on a Parylene coated steel cantilever frame which carries four cantilevers. Gold posts align and hold the cantilever frame on a multi-layer PCB.

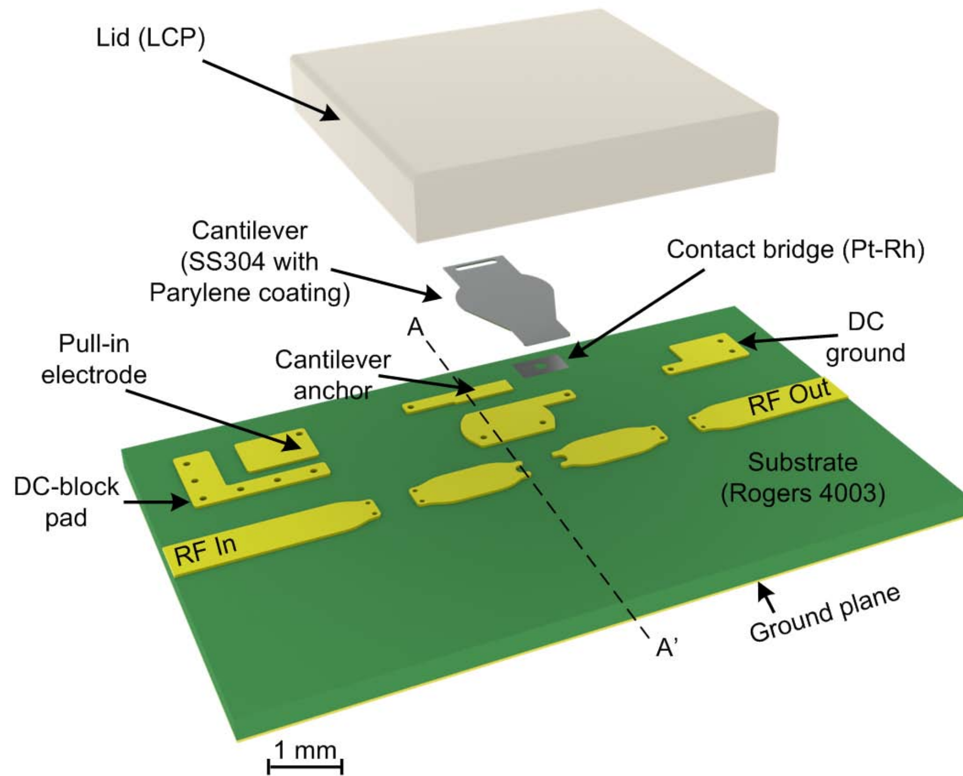

Figure 5.2: Exploded view of the single packaged micro-relay. Pt-Rh contact bridge is placed at the tip of the Parylene coated steel cantilever. The assembly is then mounted on a three-layer PCB. An LCP based lid completes the package. Device footprint (as defined by the footprint of the cantilever) is 8.4 mm^2. A–A' cross section is shown in Figure 5.4.

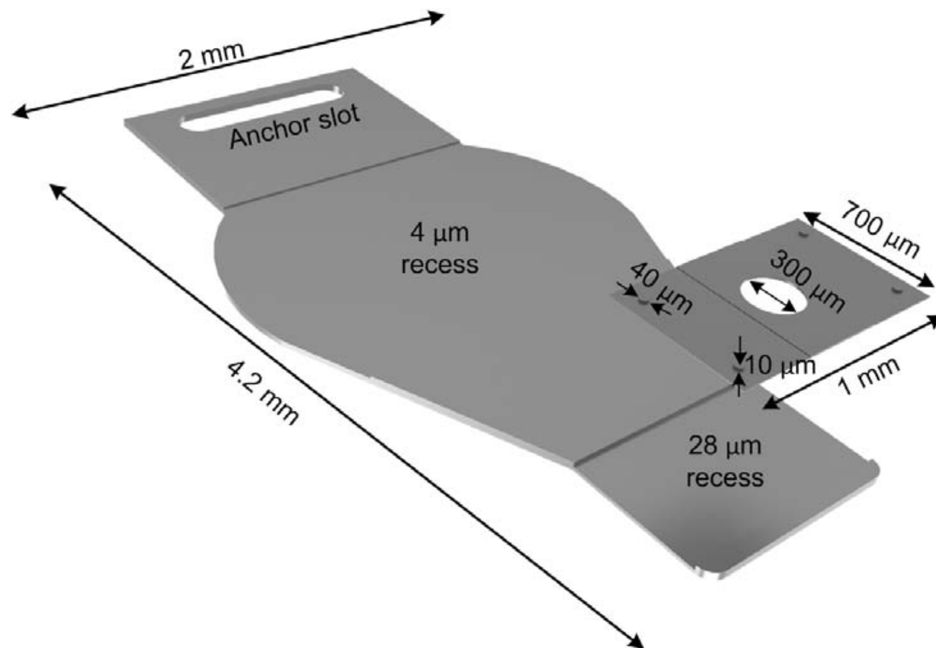

Figure 5.3: Dimensions for the cantilever and the contact bridge

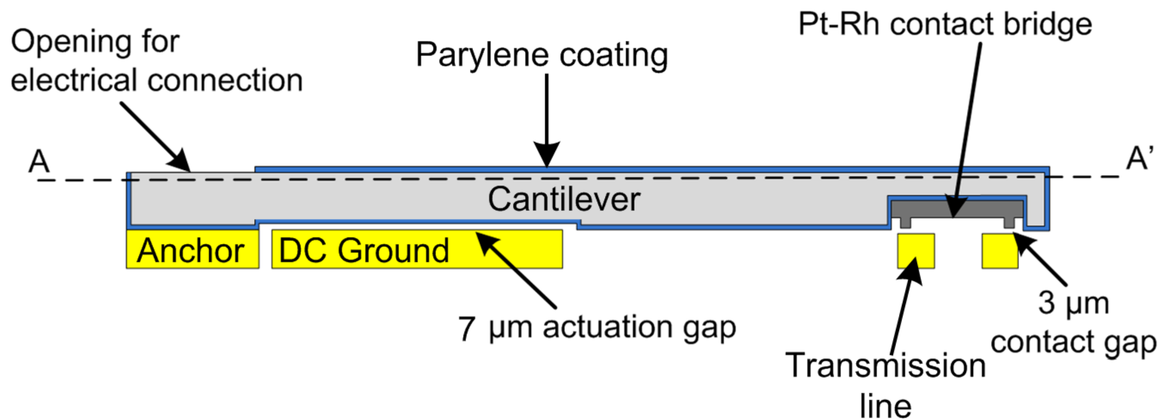

Figure 5.4: A–A' cross section as noted in Figure 5.2. PCB substrate is neglected. The actuation gap is 7 µm as a result of 4 µm of machined recess and 3 µm Parylene thickness. The contact gap is defined by the Parylene thickness alone and is 3 µm.

The cantilever-contact bridge assembly is positioned on a multi-layer PCB orthogonally with respect to the transmission line. The PCB uses a 600 µm-thick Rogers 4003 substrate with Cu/Ni/Au traces and provides a reduced loss at microwave frequencies. The substrate is composed of three layers (each 200 µm thick) to accommodate multi-layer tracing. The PCB traces are otherwise similar to the optimized ones described in the previous chapter and can be divided into four regions. The first region includes two transmission line segments with 50 Ω characteristic impedance and provides input and output paths for the RF signal. At the end of open lines, the terminals fork out to accommodate regions for contact dimples (150 µm × 150 µm each). The transmission line segments are located on two layers: the top-layer and the layer-2 which is at 200 µm depth from the substrate surface (Fig. 5.5). This design approach is used to enable the location of a package lid on top of the device which would directly sit on the PCB substrate. Blind vias of 150 µm diameter connect the top layer with the layer-2 transmission line. The vias are plated with Cu/Ni/Au traces.

The second region includes the DC ground electrode. The ground layer across the cantilever is designed on the top layer of metal in the PCB. The DC signal is transferred on to layer-2 through blind vias of 250 μm diameter. DC ground is shunted to the RF ground plane through plated vias. The connection is provided by 250 μm diameter through vias.

The third region includes the pull-in electrode which is used to electrostatically actuate the cantilever. It is also placed onto both top layer and the layer-2 to allow for the package lid. The fourth region includes an L-shaped electrode, similar to the one described in Chapter 4, which allows for the placement of a DC-blocking capacitor and also acts as a shield to minimize RF signal coupling from the transmission line. In this design, the multi-layer transmission line is one of the major contributors to high RF signal reflection. The current transmission line design is obtained through an iterative optimization study to enhance RF switching performance. The simulations are described toward the end of this section.

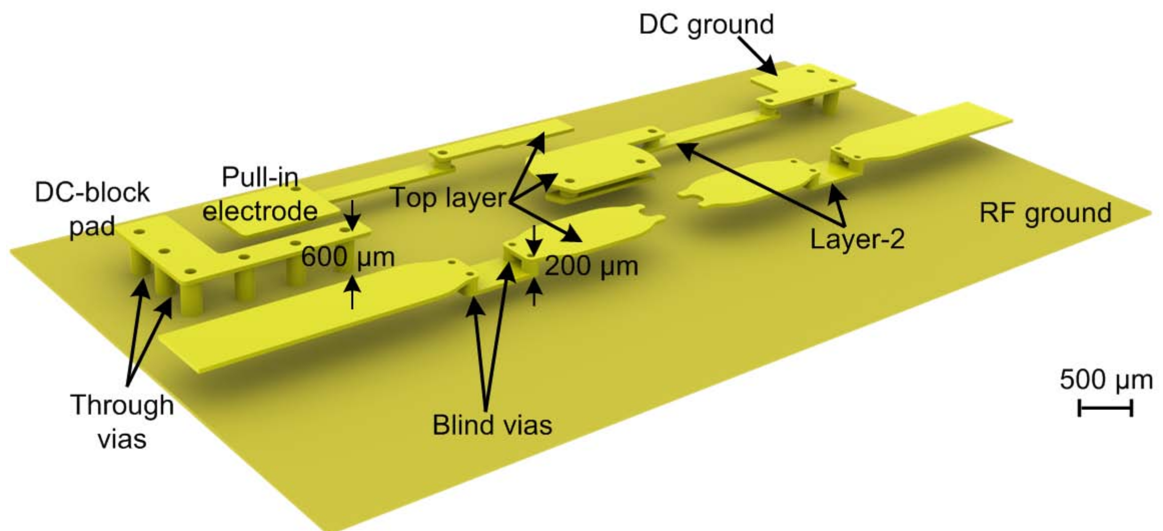

Figure 5.5: DC and RF lines shown in separation from the PCB substrate. All the vias are plated with Cu/Ni/Au traces. Through vias connect the top layer to the bottom layer whereas blind vias connect the top layer to the layer-2.

A 1 mm-tall lid (Stratedge Corp.) with 0.5 mm wall thickness is preferred to package the device. LCP based Vectra A130 was preferred to eliminate RF signal coupling due to its low loss tangent of 0.002 and very high electrical resistivity (10^{15} Ω·cm) [Pro11]. Nitrogen was chosen as encapsulated gas. The edges of the lid contain an epoxy preform with a wavy profile, allowing the gas intake prior to curing, after which it levels with the substrate and seals the device. Figure 5.6 shows the dimensions of the package lid whereas Figure 5.7 shows the drawing of an assembled and packaged device.

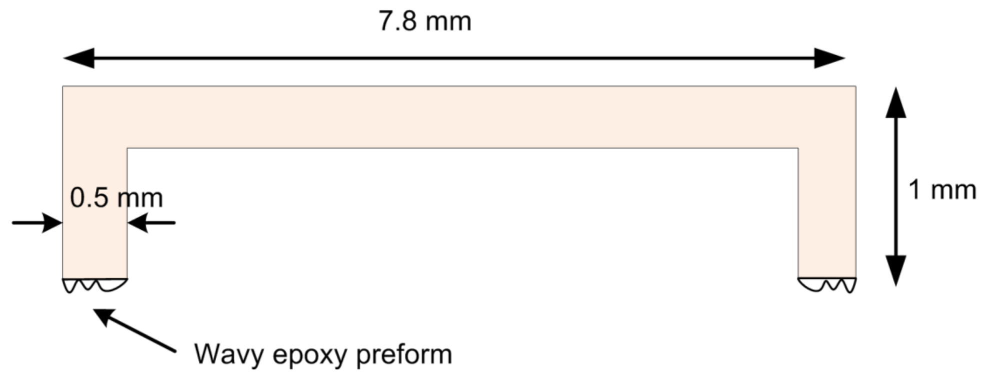

Figure 5.6: Package lid dimensions. Wavy epoxy preform allows gas intake.

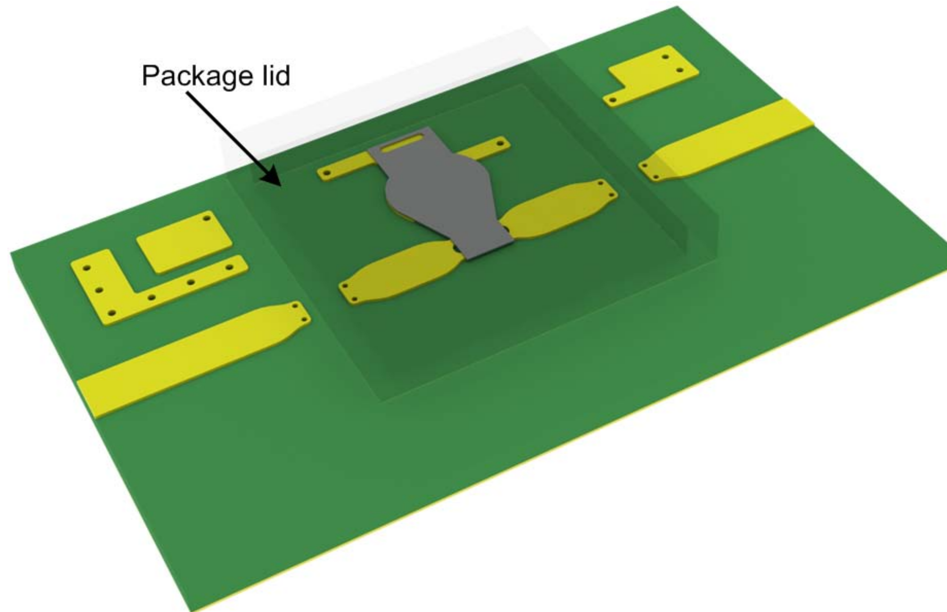

Figure 5.7: Assembled, singulated and packaged micro-relay. The package lid is shown in transparent.

ANSYS Workbench Finite Element Analysis was used to perform the electrostatic modeling for the RF micro-relay. The displacement and the stress distribution are shown in Figure 5.8(a) and (b), respectively. The model consisted only of the micro-relay and partial transmission line. All other components were neglected. The "fixed geometry" boundary condition was applied around the anchor slot on the cantilever. The Parylene coating was modeled as a 3 µm-thick solid body enveloping the cantilever. The "bonded contact" boundary conditions were used between the cantilever and the contact bridge, and the transmission line. Extracted pull-in voltage for 3 µm tip displacement was 72 V. Uniform tip displacement is shown in the Figure. The displacement above the ground electrode was less than 2 µm. This suggested that the pull-in would be prevented. The stiffness of the micro-relay including the Parylene coated cantilever and the contact bridge was 110 N/m. Figure 5.8(b) shows the same stress distribution over four contact dimples. The contact force per contact region was 0.55 mN (with 2.2 mN evenly distributed over four contact regions) for an increased actuation voltage of 100 V. The extracted turn-on time from dynamic analysis was 9 ms.

The multi-layer transmission line was optimized to reduce the fringing and the RF coupling. Geometric refinement considered a thru-line optimization. All the traces on the PCB as well as the package were included in the model however the cantilever and the contact bridge were excluded. Iterative RF simulations were performed in HFSS and S_{11} was monitored. A total of 41 transmission line configurations were studied however only 5 configurations are presented here since the remaining configurations presented only a minimal geometric variation.

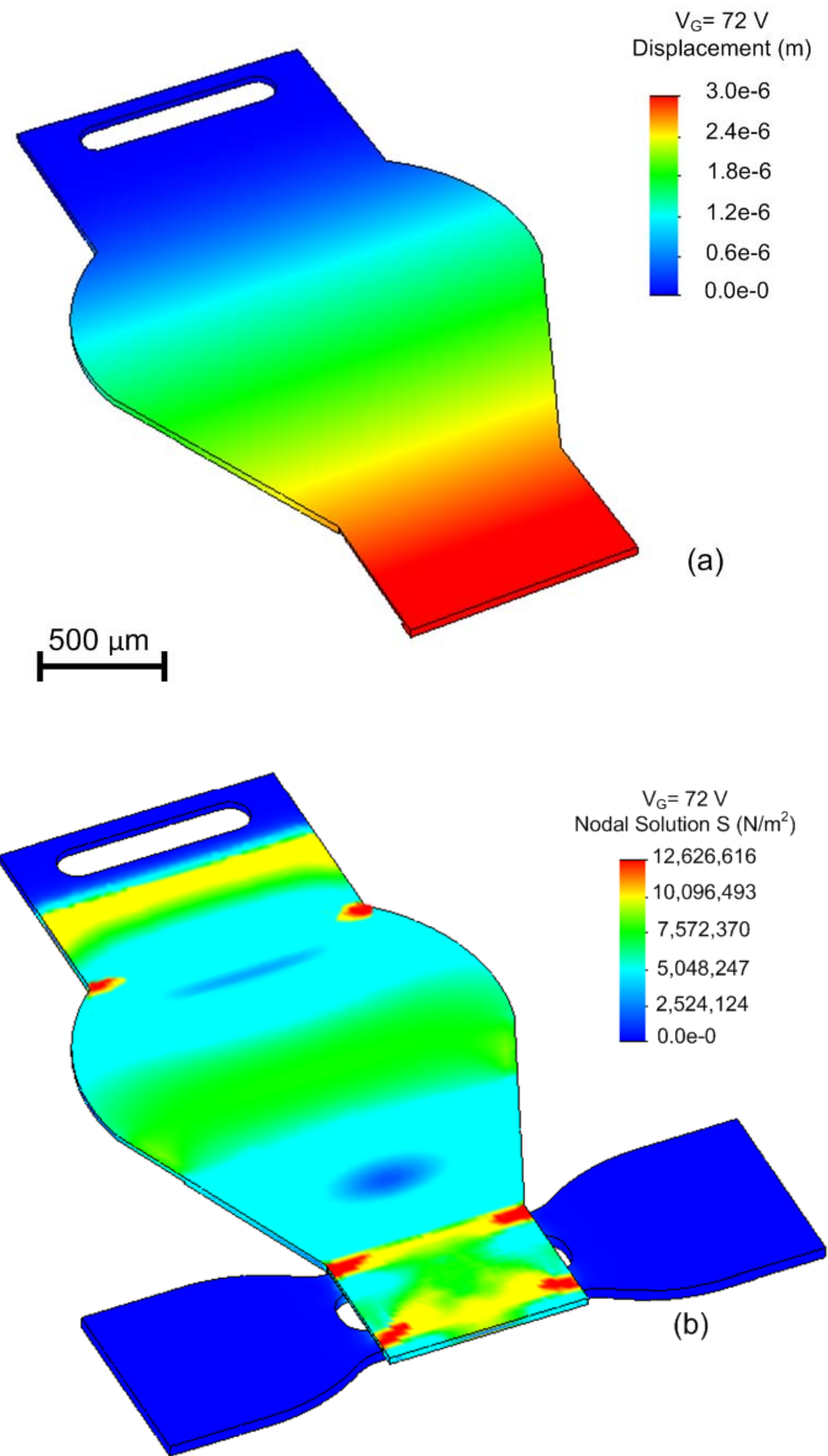

Figure 5.8: Electrostatic FEA for the micro-relay. (a) Tip displacement was 3 µm for 72 V pull-in voltage. (b)Post-contact stress distribution. All four contact points had the same stress. Simulated total contact force was 2.2 mN (evenly distributed over four contact regions) for an increased actuation voltage of 100 V.

Figure 5.9 shows the thru line configurations. All the lines were matched to 50 Ω characteristic impedance. Geometric considerations included mainly design limitations imposed by the PCB manufacturing process. Two main limitations were the minimum via diameter of 125 µm and the minimum layer thickness of 100 µm which defined the minimum via height. Table 5.1 summarizes via dimensions and configurations. Configuration-1 used a single point connection between the top layer and the layer-2, by a single via with a 400 µm diameter. The length of the line segment on the layer-2 was designed as 4.2 mm to match with the line segment length at the top layer. Configuration-2 employed a via array in a 4×1 configuration, each via with 250 µm diameter whereas Configuration-3 has six vias of 225 µm diameter in 3x2 configuration. Layer-2 line segments for Configuration-4 were shorter than Configurations 1-3. Two vias of 200 µm diameter were placed side by side. Configuration-5 was the final layout geometry in a thru line configuration. The length of the layer-2 line segment was shortened to 1.1 mm, wide enough for the placement of the package lid. Via diameter was reduced to 175 µm and via height was increased to 200 µm as per to follow available dielectric layer thickness.

Table 5.1: Via dimensions and configurations for the thru line optimization

Configuration	Via count	Via diameter (µm)	Via height (µm)	Via configuration	Layer-2 line length (mm)
1	1	400	150	Single via	4.2
2	4	250	150	4×1 inline	3.8
3	6	225	100	3x2	4
4	2	200	150	2x1	2
5	2	175	200	2x1	1.1

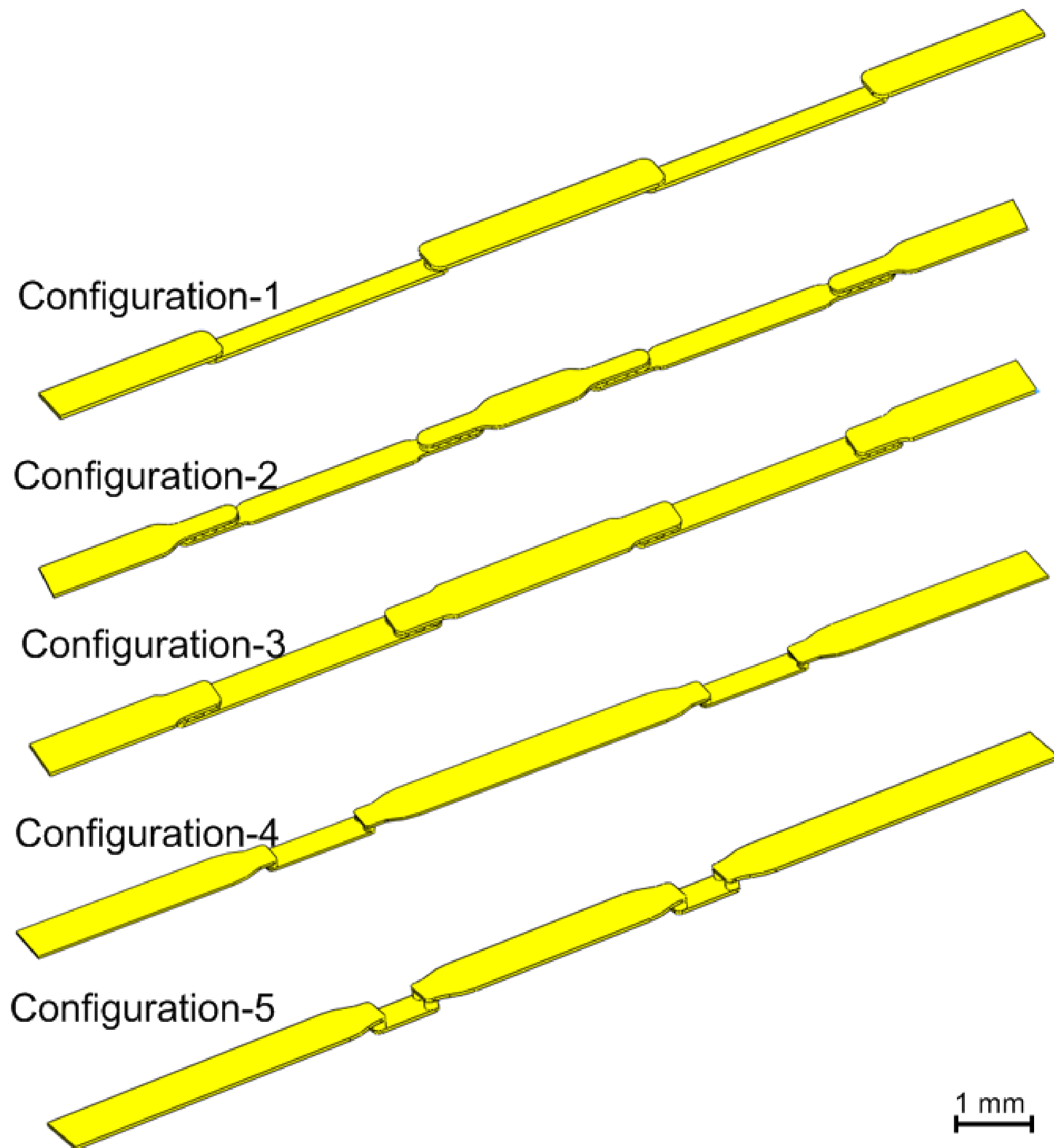

Figure 5.9: Geometric configurations for the thru transmission lines used in RF optimization study.

Figure 5.10 shows the S_{11} for 10 GHz bandwidth for each thru line configuration. Configuration-5 resulted in smallest reflection with approximately -28 dB at 10 GHz. The resonance which occurred around 7 GHz was eliminated with the use of an external capacitor which is described in the testing section.

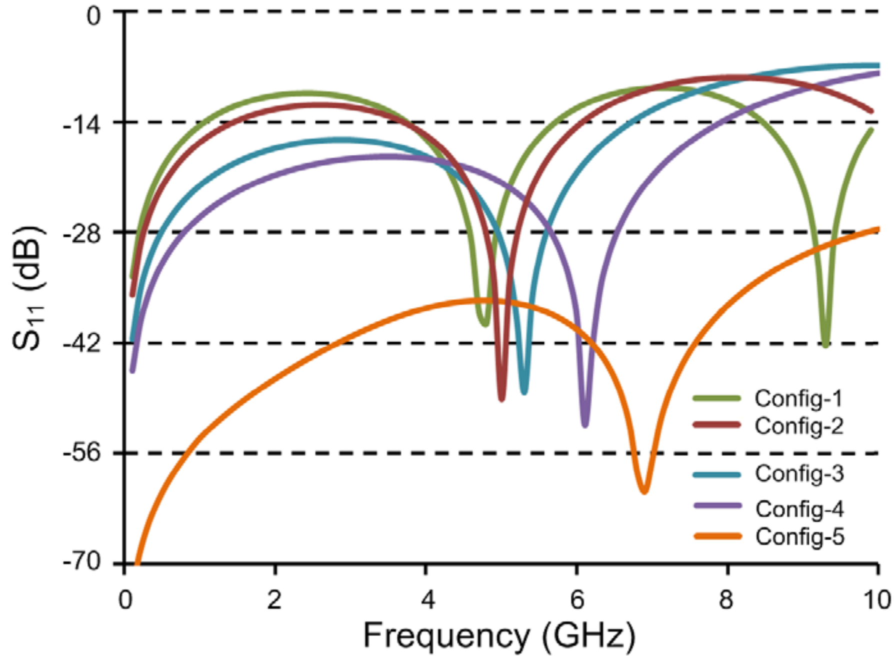

Figure 5.10: Full-wave HFSS simulation results showing S_{11} for five configurations. The cantilever and the contact bridge were discarded in simulations. Configuration-5 provides the smallest reflection with nearly -28 dB at 10 GHz.

5.2. Fabrication and assembly

The contact bridges for the micro-relay were serially fabricated using μEDM in 80:20 Pt-Rh (Alfa Aesar Corp., 99.99% purity). The thickness of the stock metal foils was 25 μm. Initially a through hole of 300 μm diameter was created in the center of the structure. This was followed by 10 μm recesses to define the 40 μm diameter contact dimples. Since the height of the dimples was not modified, surface roughness of the contact dimples was same as the surface roughness of the virgin stock foil. The roughness was measured using Zygo NewView 5000 interferometer. Average roughness R_a was approximately 26 nm.

The cantilever frame was photochemically etched from 50 μm-thick SS304 foils (Kemac Technology Inc., CA). Perforations of 500 μm diameter were located on the four

corners of the frame for batch assembly onto the PCB. In addition, slots of 250 μm diameter and 1 mm length were located on the individual cantilevers for the assembly over the PCB.

Etched cantilever frames were then serially machined using μEDM to create recesses of 4 μm and 28 μm, in the middle and at the tip of the cantilevers, respectively. Lowest available discharge energy of 18 nJ was used for minimized stress on the cantilevers. The cantilever frames were thoroughly cleaned in an ultrasonic tank with kerosene based EDM oil, acetone, IPA and de-ionized water, in specified order. Following this, the cantilever frames were deposited with 3 μm-thick C-type Parylene.

A three-layer 600 μm-thick Rogers 4003 was used as the substrate dielectric (Circuit Express, AZ). On all three layers, Cu traces (70 μm-thick) provided the bias electrodes, the transmission line segments, and blind and through vias. A 4 μm-thick Ni was used as an adhesion layer on the Cu base, and 0.15 μm-thick outer gold layer provided high conductivity electrical contacts. All the individual components are shown in Figure 5.11(a).

For the device assembly, the contact bridges were placed inside the recessed regions at the tip of the cantilevers and fixed by applying high temperature epoxy (Cotronics Duralco 4703, 645 K maximum temperature) around the through hole (Fig. 5.11(b)).

To batch assemble the cantilever frame and the PCB, alignment posts were fabricated using μEDM from 500 μm diameter gold wire, and tightly fitted into the vias on the PCB. The cantilever frame with mounted contact bridges were assembled over the posts (Fig. 5.11(c)) and epoxy was applied around the posts to fix the frame. In addition,

epoxy was applied on the cantilever frame support traces for added mechanical strength during device singulation process. Part of the Parylene was manually removed with tweezers from the top of the cantilever to create a location for the electrical connection. The individual cantilevers were fixed onto the PCB by applying electrically conductive epoxy (Creative Materials, volume resistivity: 300 μΩ-cm) around the slots. Device singulation cutting lines are shown in the Figure 5.11(c) inset. A linear shear blade was used to cut along the lines and singulate the devices. Residual connection tab parts on the cantilevers were deburred using a dremel tool.

For device packaging, Vectra A130 lid was aligned onto the single devices and press fitted using a mini spring clamp with 4.5 N pressing force. The device was then placed in a vacuum oven. The pressure inside the oven was first reduced to approximately 5 Pa at room temperature. Following this, the vacuum was choked and the nitrogen was leaked inside the oven up to the atmosphere pressure. The oven temperature was then adjusted to 160 ° C and the package lids were cured for 1 hour. After the curing, the spring clamps were removed. Figure 5.11(d) shows packaged devices.

A total of 5 devices were fabricated and assembled. The distribution of those devices is as follows: two devices for DC on-state resistance characterization, hysteresis study, and for small-signal characterization with and without the package; one device for high power testing, and two devices for the lifetime characterization at 1 W and 10 W.

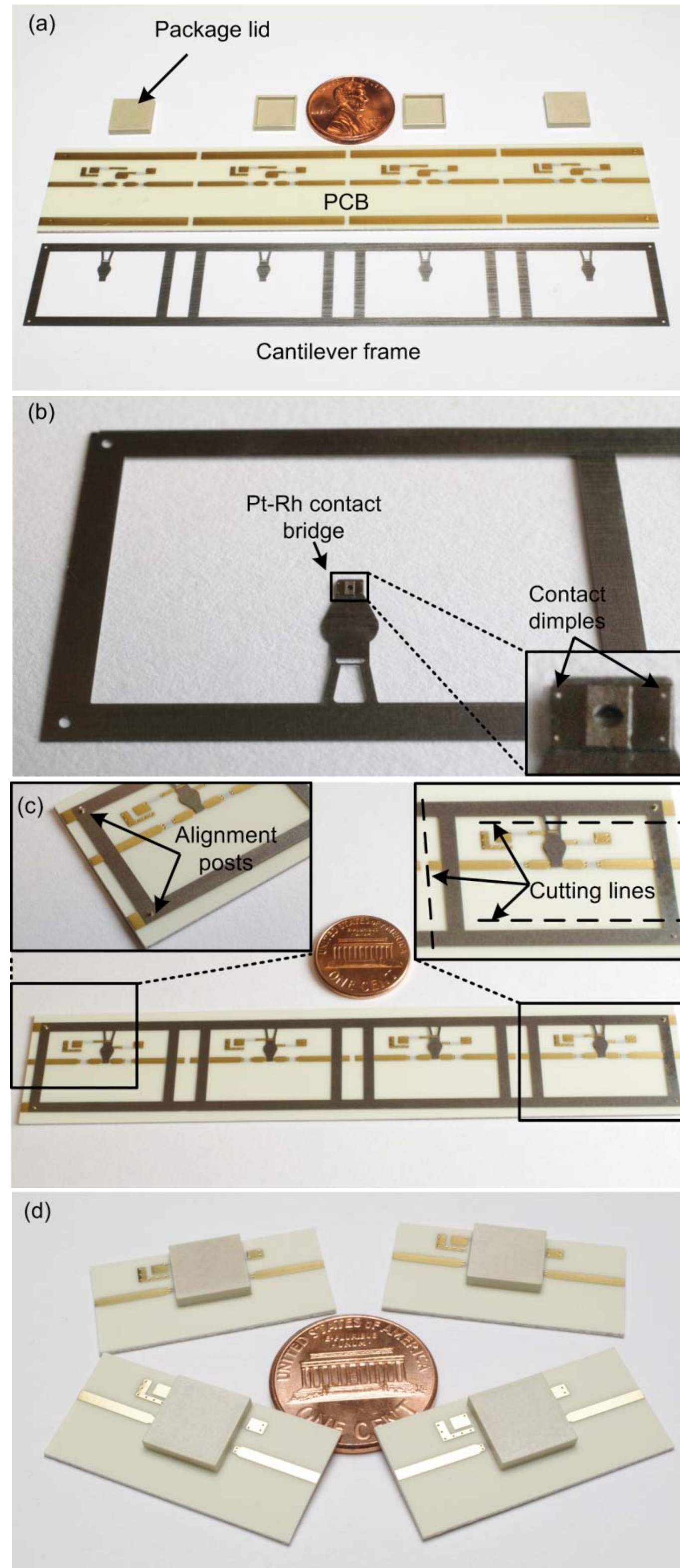

Figure 5.11: Assembly sequence for the batch RF micro-relay. (a) Individual components are shown. (b) Cantilever frames deposited with Parylene and assembled with contact bridges. (c) Cantilever frame-PCB assembly. (d) Packaged single devices.

5.3. Experimental evaluation

5.3.1. Electrical testing

Electrical testing of the batch fabricated micro-relay consisted of DC, and RF characterizations in both small-signal and high power. RF test circuit for the micro-relay is similar to the circuit presented in the previous chapter. Testing circuitry and the actuation concept are shown in Fig. 5.12(a). Small-signal two-port RF in and out were supplied on the transmission line from a network analyzer through SMA type coaxial connectors. Small-signal power was 32 μW. For electrostatic actuation, an actuation voltage (V_G) was applied on the pull-in electrode. A solder joint was created between the Parylene-free opening on top of the cantilever and the pull-in electrode. DC ground was applied on the ground electrode with a 20 kΩ resistor. For contact resistance characterization, a line current replaced the RF signal for a four probe I-V test. The current source was limited to 10 V compliance. Although the bottom of cantilever is fully coated with Parylene, the cantilever isolation was monitored by the voltage V_{ISO} with an isolation resistor R_{ISO} (1 MΩ). A surface mount DC blocking capacitor was placed between the pull-in electrode and the DC-block pad. A 10 pF capacitor was chosen to eliminate the resonance shown in Figure 5.10.

The tip displacement hysteresis of the micro-relay is shown in Figure 5.13. The displacement was recorded using the laser displacement sensor (Keyence LK-G32, 50 nm resolution). The actuation voltage was swept from 0 V to 120 V and back to 0 V. The pull-in and turn-off voltages were 78 V and 40 V, respectively. Total device stiffness of 125 N/m was extracted following equation 3.4 . Actuation force and recoil forces are extracted as 6 mN and 3.4 mN.

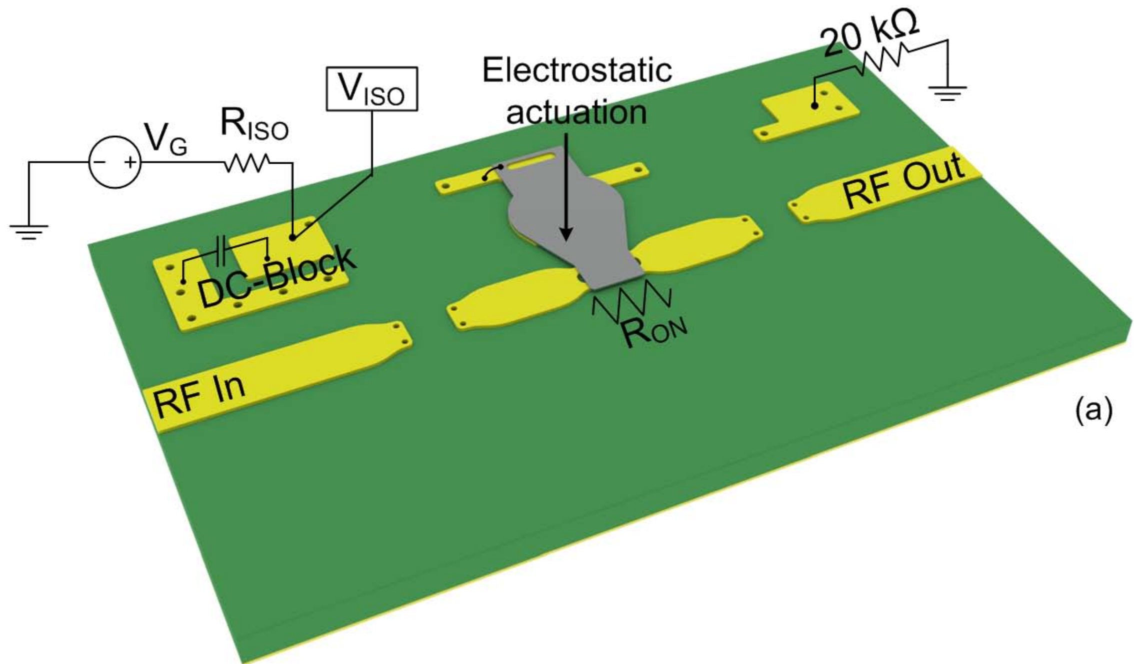

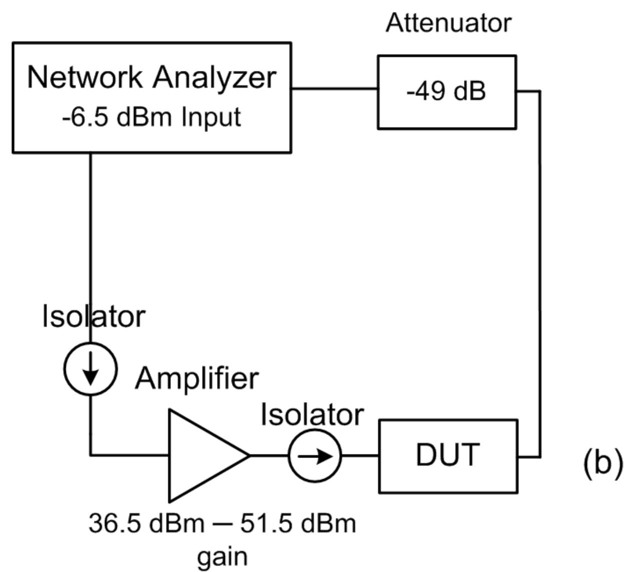

Figure 5.12: (a) Testing circuitry for batch fabricated RF micro-relay. Actuation voltage, V_G was used for the electrostatic actuation. V_{ISO} was monitored to detect any leakage with a 1 MΩ resistor. On-state resistance R_{ON} included the contact resistance, the bridge resistance and the parasitics. A 10 pF surface mount capacitor was used for DC blocking. (b) High power RF test setup (limited to 30 W at 3 GHz).

The on-state resistance, R_{ON} included the contact resistance, the contact bridge resistance, and the parasitics. Figure 5.14 shows the experimental results. The total series on-state resistance at 78 V pull-in was approximately 15 Ω. As the actuation

voltage was increased, R_{ON} was reduced sharply and saturated around 1.1 Ω for 115 V. Past this voltage, no significant change was observed. Measured turn-on times were approximately 10 ms.

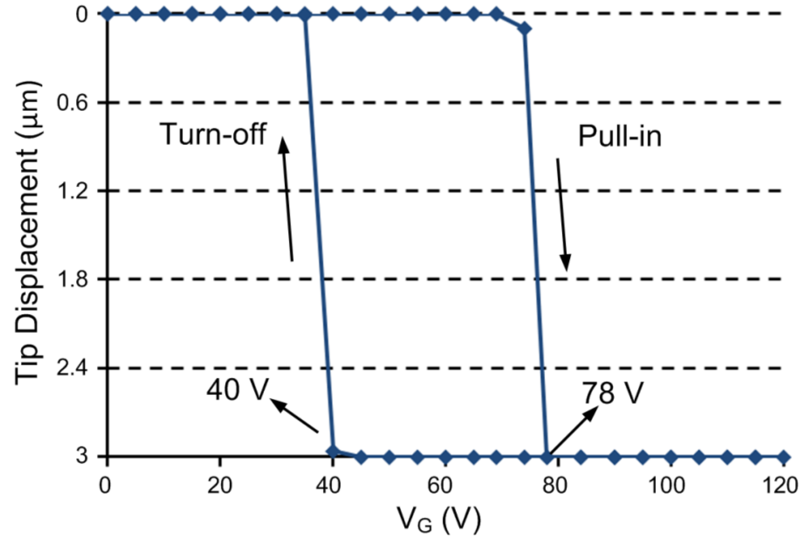

Figure 5.13: Displacement hysteresis for the micro-relay. Actuation voltage was swept 0V–120V–0V. Device pull-in and turn-off voltages were 78 V and 40 V respectively. Combined stiffness of Parylene coated cantilever and the contact bridge was 125 N/m.

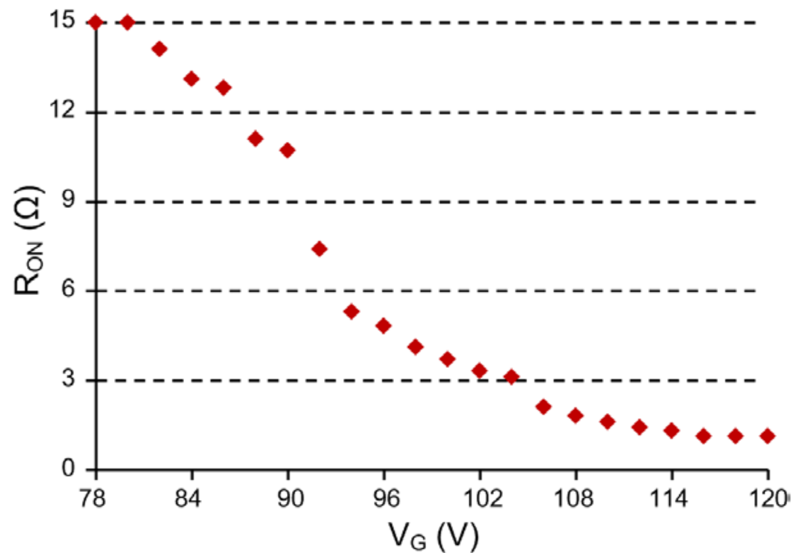

Figure 5.14: Experimental results showing the change of total series on-state resistance with increasing actuation voltage. Test was run on packaged devices with nitrogen at atmospheric pressure. On-state resistance at pull-in was 15 Ω. Further increase of actuation voltage resulted in a lower resistance due to larger contact forces. On-state resistance saturated past 115 V and was approximately 1.1 Ω.

For small-signal RF analysis, S-parameters were characterized in the down-state and in the up-state with 32 μW of RF power and experiments were compared to the simulations. Small-signal tests were run on both unpackaged devices in air ambient and on packaged devices in nitrogen both at atmospheric pressures. The effect of the package lid on RF performance was observed. Figure 5.15 and Figure 5.16 show the RF performance for the unpackaged and packaged devices, respectively.

For the unpackaged micro-relay, the down-state insertion loss was better than -0.2 dB and -0.65 dB for up to 5 GHz and 10 GHz, respectively (Fig. 5.15(a)). In the up-state, the isolation was better than -18 dB and -12 dB up to 5 GHz and 10 GHz, respectively (Fig. 5.15(b)). Overall, experimental data was in good agreement with HFSS.

For the packaged micro-relay, down-state insertion loss was better than -0.25 dB at 5 GHz whereas it reduced to past -0.6 dB at 10 GHz (Fig. 5.16(a)). Up-state isolation was better than -15 dB at 5 GHz and -12 dB at 10 GHz (Fig. 5.16(b)). Experimental data, overall agreed well with the simulations.

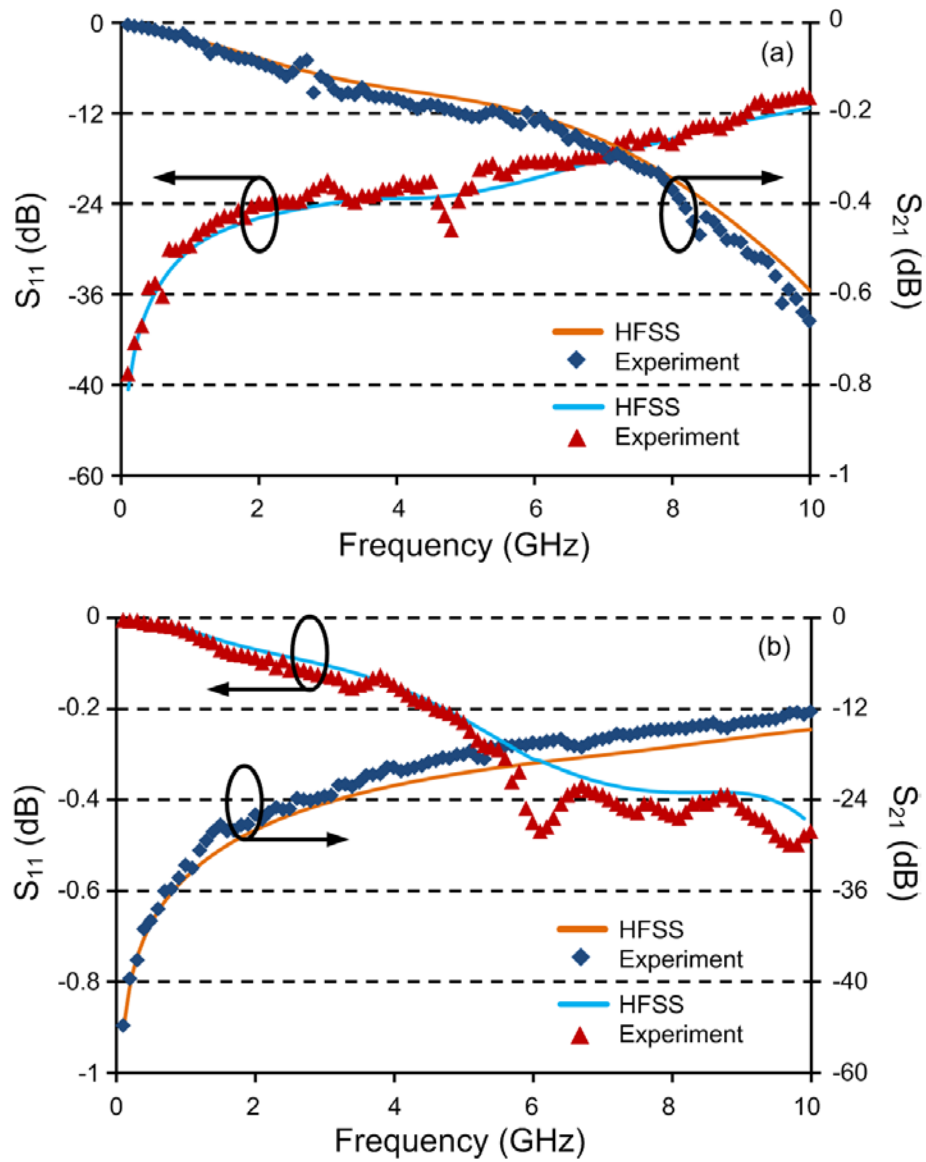

Figure 5.15: Small-signal analysis with 32 μW for the unpackaged micro-relay in air ambient at atmospheric pressure. Experimental data compared with HFSS. (a) In the down-state, the insertion loss was better than -0.2 dB for up to 5 GHz. (b) Up-state isolation was better than -18 dB up at 5 GHz.

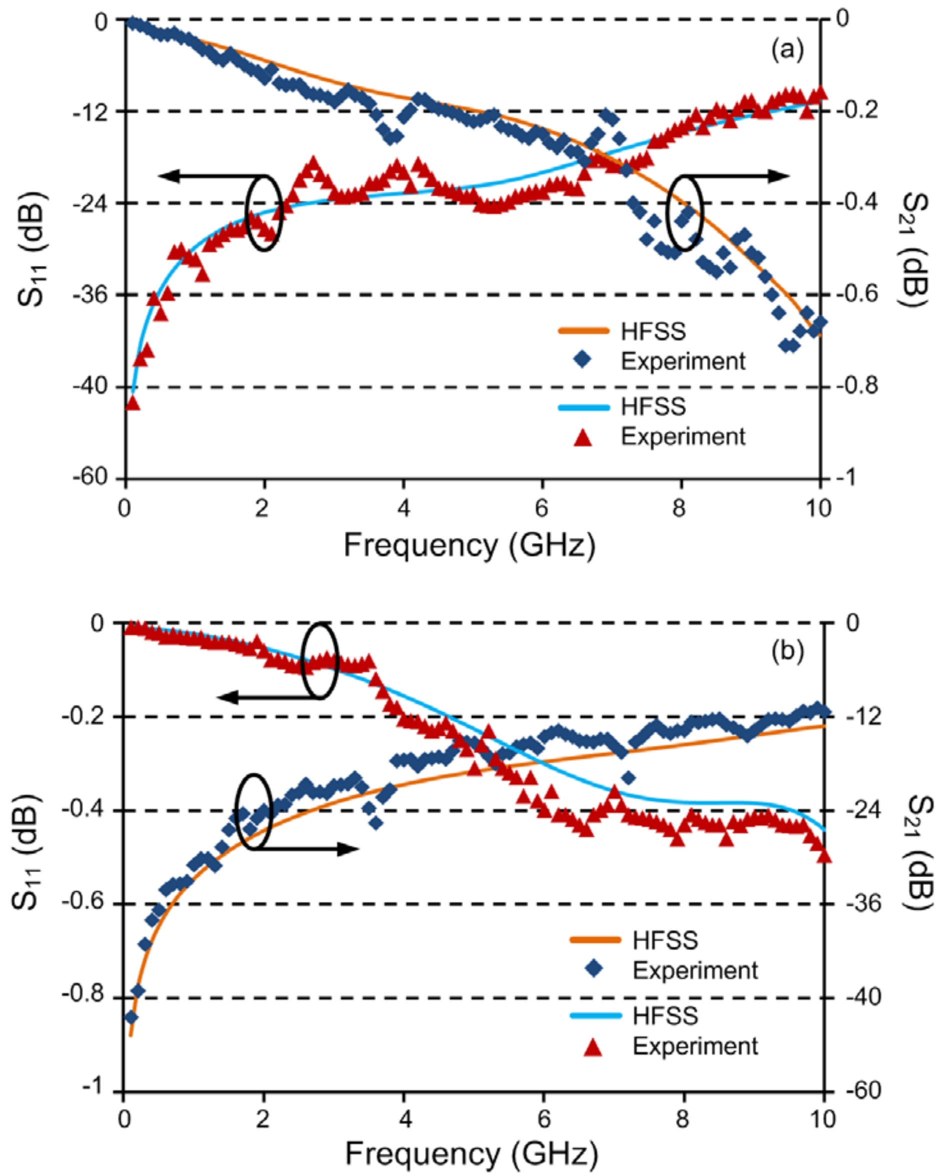

Figure 5.16: Small-signal analysis with 32 μW for the packaged micro-relay in nitrogen at atmospheric pressure. Experimental data compared with HFSS. (a) Down-state insertion loss was better than -0.25 dB at 5 GHz. (b) In the up-state, isolation was better than -15 dB for up to 5 GHz.

Figure 5.17 shows small-signal analysis for another packaged micro-relay fabricated in a separate batch. RF performance is consistent with the device characterized in Figure 5.16 both in the down-state and in the up-state.

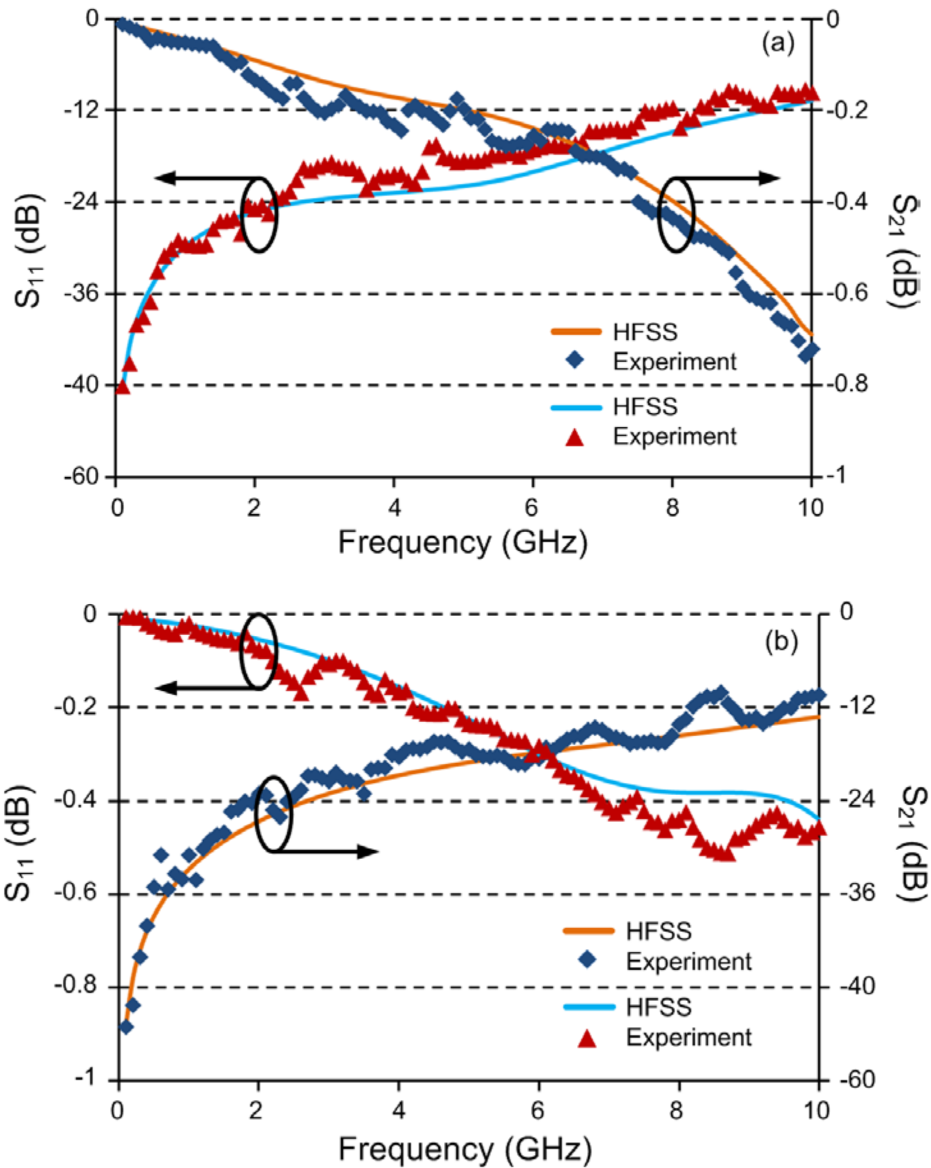

Figure 5.17: Small-signal analysis with 32 μW for another packaged micro-relay to show consistency among fabricated devices. Experimental result and HFSS data for the device (a) in the down-state and (b) in the up-state.

The setup for the high power handling test is shown in Fig. 5.12(b). A discrete power sweep was performed through 12 gain levels from 1 W up to 30 W of RF power at 3 GHz which was the testing setup limit (Amplifier Research 30W1000B). Only S_{21} was monitored in the down-state and in the up-state due to non-reciprocal nature of the power amplifier. Test was performed on the packaged micro-relay. Hot switching conditions

were followed with continuous RF power and 1 s on-state times. The actuation voltage was set to 120 V for minimum on-state resistance. Figure 5.18 shows the experimental results. In the down-state, insertion loss was better than -0.2 dB for up to 5 W of RF power. Past this point, insertion loss deteriorated continuously down to -0.9 dB, and the micro-relay failed due to contact microwelding at 20 W. The up-state isolation was approximately constant at -21 dB over the power sweep range. Maximum variation was below 1 dB and self-actuation was not observed.

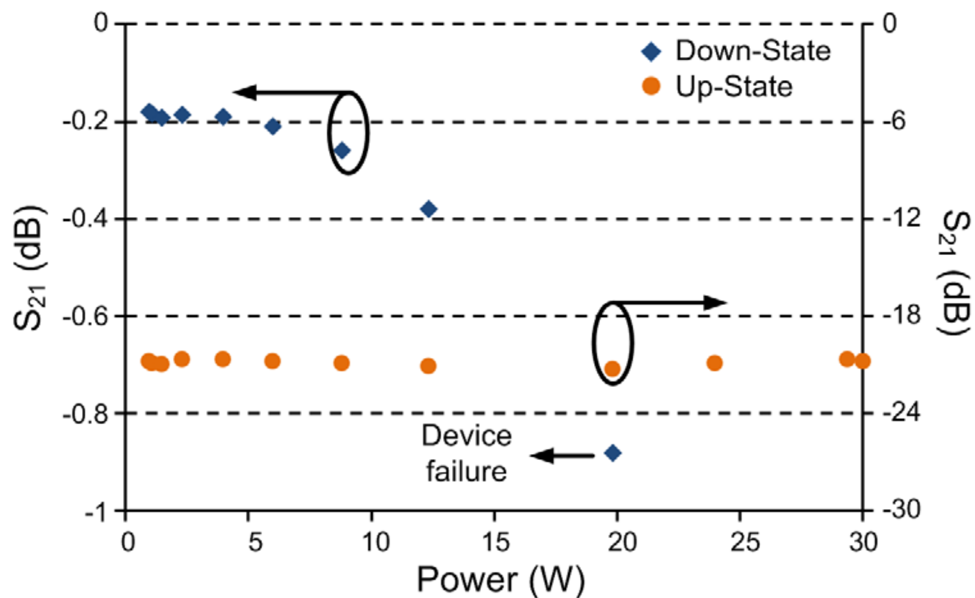

Figure 5.18: High power handling test for the packaged RF micro-relay (nitrogen in atmospheric pressure). Tests were performed at 3 GHz and up to 30 W of RF power (test setup limit), at 120 V actuation voltage, and 1 s on-state time. Insertion loss in the down-state was below -0.2 dB for up to 5 W and decayed down to -0.9 dB at 20 W where the device failed due to microwelding. The up-state isolation was approximately -21 dB over the 12 gain steps and self-actuation was not observed.

The output power was estimated using the input power and S-parameters following the relationship below [Poz05]:

$$P_{OUT}(W) = 10^{\frac{P(dBm)}{10}} \times 0.001; \quad P(dBm) = 10\log_{10} \frac{P_{in}(W)\left\{1 - \left(10^{\frac{S_{11}(dB)}{10}}\right)^2\right\}}{0.001(W)} + 2 \times S_{21}(dB) \quad (5.1)$$

In the above equation, S_{21} and S_{11} are the down-state insertion loss at high power and return loss at small-signal, respectively. The equation considers a non-reflection case where the constant S_{11} value of -22.7 dB at 3 GHz was used from the small-signal analysis since the high power test only included S_{21} characterization at different power levels. It should be noted that the S_{11} contribution to the output power has only a minor effect when compared to S_{21}, which is strongly related to contact degradation at high power levels. Figure 5.19 shows the input-output power relation. Output power was relatively linear with the input power up to 13 W. Beyond this power level, output power was reduced due to the degraded down-state insertion loss close to the point of failure.

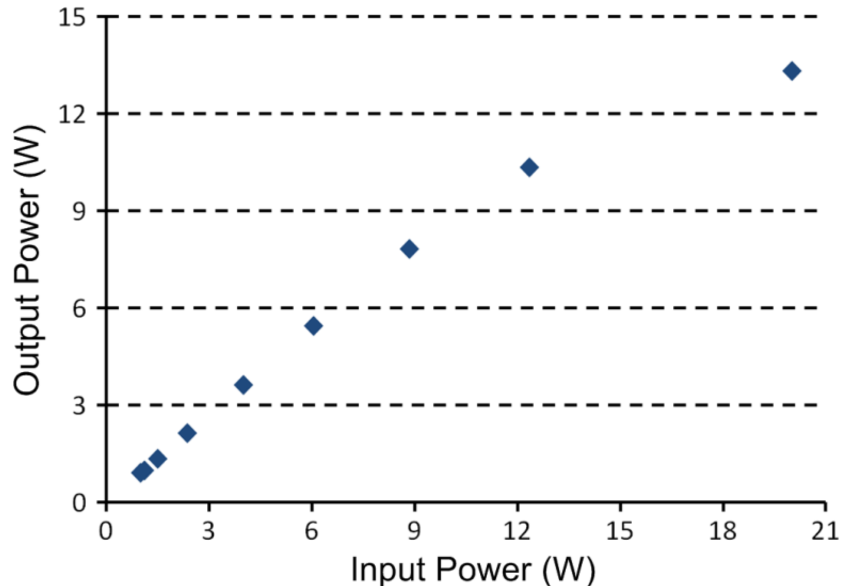

Figure 5.19: Output power estimated from the input power, down-state small-signal S_{11} and down-state high power S_{21}. Output power exhibited a relatively linear relationship with the input power up to approximately 13 W, beyond which the linearity was distorted due to dominant effect of down-state S_{21} which degrades significantly at the point of failure at 20 W.

5.3.2. Lifetime testing

Packaged micro-relays with nitrogen at atmospheric pressure were tested for the lifetime. Two experiments were conducted under hot switching conditions. The first experiment considered 1 W of continuous RF power supplied at 3 GHz. The switching frequency was set to 0.5 Hz frequency with 50% duty cycle as per 1 s on and 1 s off times. The second experiment considered 10 W of continuous RF power supplied at 3 GHz with a switching frequency of 0.2 Hz and 2% duty cycle, resulting in 0.1 s on-time and 4.9 s off-time. Similar to high power testing, the actuation voltage was kept at 120 V for both experiments. Figure 5.20 shows the S_{21} for the up-state and the down-state. For 1 W power, the device failed at the $10{,}913^{th}$ cycle in the down-state where insertion loss was below -0.9 dB. The up-state isolation remained within ±3 dB of -21 dB throughout the test (Fig. 5.20(a)). For 10 W power, the device failed after 8,414 cycles in the down state with similar insertion loss and isolation values to 1 W case (Fig. 5.20(b)).

5.3.3. Package testing

Package testing for the devices followed MIL-STD-883G hermeticity standards (Polaris Electronics Corp., KS). A total of nine packages – filled with nitrogen at atmospheric pressure – were tested. Test consisted of He bombing of packages at 60 Psi pressure for 1 hour. The packages were then removed from bombing chamber and placed in a vacuum chamber at 1 Pa for He detection. The packages were tested at three different time intervals to allow for any He residue that might be trapped in the epoxy to be released. He detection was done right after the bombing, 30 minutes after the bombing and 60 minutes after the bombing and was repeated for certain devices. The

testing scheme and results are summarized in Table 5.2. The pass/fail threshold for this standard was 5 $\times 10^{-8}$ atm cc/s. The packages 1-3 failed when tested right after the bombing potentially due to trapped He still present on the epoxy. Package 2 passed the test when re-tested after 60 minutes of bombing and package-3 passed when re-tested after both 60 minutes and 30 minutes of bombing. Packages 5,6, and 8 and 9 also passed the test similarly after 30 minutes and 60 minutes of bombing, respectively.

Packages were observed under the optical microscope after testing for any cracks or deformation as a result of high pressure He bombing which might lead to misinterpretation of the results. No such deformations were observed for any of the nine packages (Fig. 5.21).

5.4. Discussion and Conclusions

This chapter introduced a process to batch assemble multiple micro-relays with Pt-Rh contacts on PCBs. Multi-layer PCB structure allowed for the direct integration of a lid for the device packaging. Singulated micro-relays had a footprint of 8.4 mm^2. The pull-in voltage was 78 V, within 10% of modeled value of 72 V. The small difference can be related to minimal gap changes during the assembly process. On-state resistance, R_{ON}, included the contact resistance, the contact bridge resistance, and the parasitics. On-state resistances as low as 1.1 Ω were observed for an increased actuation voltage of 115 V.

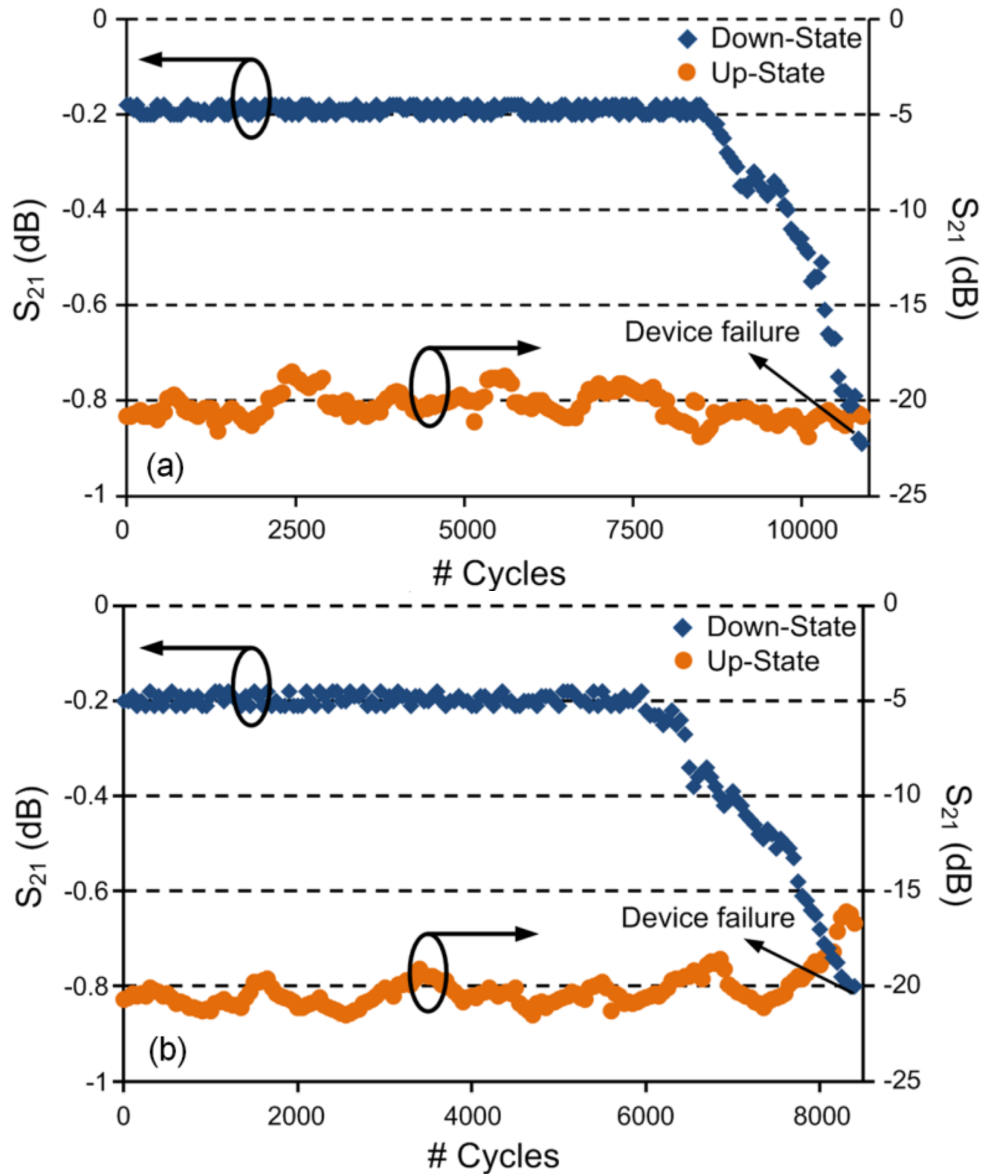

Figure 5.20: Hot switching lifetime characterization of packaged micro-relays operating in nitrogen at atmospheric pressure. Actuation voltage was set for 120 V. (a) Test with 1 W continuous RF power supplied at 3 GHz. Switching frequency was 0.5 Hz with 1s on and off-times. The device failed after 10,913 cycles in the down-state. (b) Test with 10 W continuous RF power at 3 GHz. Switching frequency was 0.2 Hz with 0.1s on and 4.9s off-times. The device failed after 8,414 cycles in the down-state. For both cases, insertion loss was below -0.8 dB at the point of failure whereas isolation remained within ± 3 dB of -21 dB and self-actuation was not observed.

Table 5.2: Package test results for nine packages tested for helium detection immediately after bombing, 30 minutes after bombing and 60 minutes after bombing

Package #	Immediately after bombing (10^{-8} atm cc/s)	30 min after bombing (10^{-8} atm cc/s)	60 min after bombing (10^{-8} atm cc/s)
1	50	10	6
2	10	8	4
3	8	5	1
4		9	6
5		4	1
6		5	2
7			7
8			5
9			3

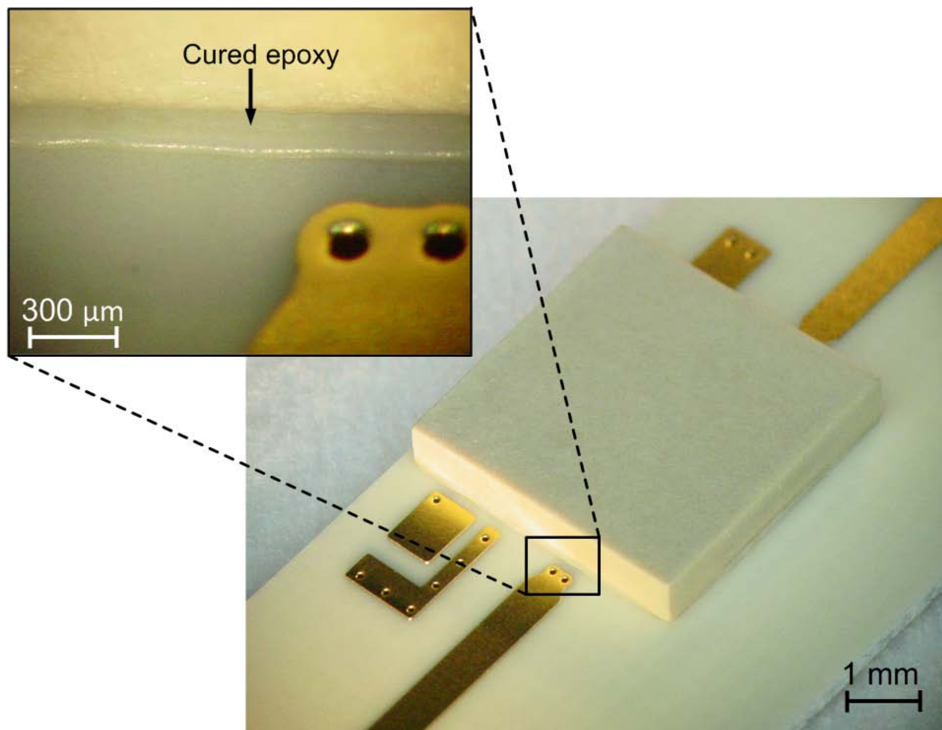

Figure 5.21: Device packages were observed under optical microscope after testing for any deformation or crack formation in the cured epoxy as a possible reason for high pressure He bombing. No such defects were observed for any of the nine packages.

Both unpackaged and packaged devices were tested for small-signal RF testing at 32 μW. Unpackaged devices operated in air ambient at atmospheric pressure whereas packaged devices operated in nitrogen at atmospheric pressure. For unpackaged devices, down-state insertion loss and up-state isolation were better than -0.2 dB, and -18 dB for up to 5 GHz, respectively. On the other hand, for packaged devices, down-state insertion loss and up-state isolation were better than -0.25 dB, and -15 dB for up to 5 GHz, respectively. The packaged test structures only introduced minimal degradation in RF performance mainly due to the insulation properties and very low loss tangent of the LCP package lid used. Overall, experimental data was in good agreement with HFSS. Maximum deviation for the down-state and the up-state was 0.1 dB and 5 dB, respectively. The reason for such deviation was the resonance possibly induced due to the assembly imperfections.

High power test was performed on the packaged devices operating in nitrogen at atmospheric pressure for up to 30 W at 3 GHz. The power and the frequency limits were due to the amplifier used in this study. For 1 s on-state times, the device failed in the down-state at 20 W and exhibited an S_{21} of -0.9 dB. The failure was due to the microwelding of the contacts under extreme local heating. Up-state isolation was nearly constant at approximately -21dB and no self-actuation was observed.

A packaged micro-relay operating in nitrogen at atmospheric pressure had a lifetime of 10,913 cycles under the hot switching conditions for 1 W of continuous RF power with 1 s on and off times. Another packaged micro-relay operating at 10 W continuous RF power with 0.1 s on and 4.9 s off times, operated up to 8,414 cycles.

Longer lifetimes can potentially be achieved by reducing the on-state times under the temperature rise time at the contact points.

Possible improvements to dissipate the heat generated at the contacts more effectively and increase the power handling include use of multiple vias next to contact regions as heat escape paths and alternative substrates with high thermal conductivity such as alumina and multi-layer low temperature co-fired ceramics [But08], [Kim09], [Tsa11, Gun, Uhl10].

Another possible improvement for higher RF power handling is to implement a 75 Ω impedance on transmission line, using impedance matching transformers right before the contacts, and convert the impedance back to 50 Ω after, for system level integration. Such an implementation would increase the root mean square (RMS) voltage at the transmission line but reduce the RMS current which has dominant effect in contact heating. The current reduction would result in a lower heat dissipation of the switch. This implementation may then be limited by the self-actuation voltage of the device.

The feasibility of batch fabrication and assembly of high power micro-relays as well as direct on-PCB device packaging were evaluated in this work. Based on the performance of the RF micro-relays presented in this chapter, the preliminary batch process provides an alternative for bulk foil device implementation.

CHAPTER 6

CONCLUSIONS AND FUTURE WORK

This chapter provides the conclusions of the research presented in this thesis and discusses some future directions.

6.1. Conclusions

This research effort aimed at investigating the feasibility of using bulk foil Pt-Rh contacts on micro-relays for high power DC and RF applications. Pt-Rh is a chemically inert and mechanically robust material which can withstand harsh environment and conditions. Pt-Rh alloy has excellent compromise between electrical resistivity and hardness. These properties render the material resistant to softening, melting and microwelding at very high temperatures which might occur in high power signal transmission in DC and RF switches. Therefore Pt-Rh is an ideal candidate for use in high power DC and RF micro-relays as contact material.

Three primary goals were established during the course of this study. The first one was to show the feasibility of proposed bulk foil Pt-Rh as a candidate contact metal for high power DC switching. The second one, as an extension to first goal, was to show the performance of Pt-Rh contacts for high power RF switching. The third goal was to develop a process to fabricate the micro-relays in batch and package them directly on PCBs.

For the first goal, electrostatically actuated micro-relay test structures were designed and fabricated. Design consisted of a double-cantilever structure with a Pt-Rh contact cantilever placed beneath an aluminum actuation cantilever that presses onto the former. A heat sink was located onto the actuation cantilever, directly above the contact point to dissipate local heating induced during high power switching. The entire micro-relay stack was manually assembled on a PCB for easy integration. The device had a footprint of 6.5 mm^2. The contact metal to mate with Pt-Rh was Au because of its widespread use in PCB manufacturing. In addition, the use of Au with Pt-group metals is known to alleviate the effects of frictional polymerization; the formation of a contaminant film due to absorption of organic vapor from the air under fretting conditions with shear or normal force. Devices with stainless steel 316L contact cantilevers were also fabricated to benchmark the performances with Pt-Rh.

The micro-relay contact resistance was estimated theoretically using Holm's permanent deformation model and was found 620 mΩ for 2.2 mN of total contact force. An empirical determination of contact resistance included pressing a contact cantilever against the signal line using of a precise force gauge. A total series resistance of 0.8 Ω was found.

The on-state resistance, R_{ON}, of the fabricated devices included the contact resistance, cantilever resistance and resistance of the signal lead transfer points at the anchor regions. For an actuation voltage of 160 V, the measured on-state resistances were approximately 1.5 Ω and 1.25 Ω for SS316L and Pt-Rh micro-relays, respectively. Experimentally found on-state resistances were higher than empirically estimated 0.8 Ω (for Pt-Rh micro-relays) possibly due to the added parasitic resistances during manual

assembly.

For high power tests, devices were operated until the point of failure. Failures due to localized heating occurred at 1.8 A and 2.6 A for SS316L and Pt-Rh devices, respectively. Pt-Rh micro-relays failed at a higher power than SS316L micro-relays due to lower electrical resistivity and thermal conductivity of SS316L when compared to Pt-Rh. Contact temperatures were experimentally measured and overall, they were in good agreement with the simulations. The heat management was used on the fabricated devices through forced cooling with a commercial mini-fan positioned in close proximity to the device. Pt-Rh devices with forced cooling exhibited a current rating of 2.8 A in 50.7 KPa nitrogen. The use of forced cooling suppressed contact temperature rise by approximately 20 K.

A lifetime test was also carried out. An unpackaged Pt-Rh micro-relay operated in 50.7 KPa nitrogen for 2226 cycles under 1 A line current.

For the second goal, micro-relays with SS304 cantilevers and Pt-Rh contact metals were fabricated and assembled on a PCB. The PCB was subjected to a sensitivity study and an iterative optimization for increased RF performance. Test structures with 6.4 mm^2 footprints had 90 V pull-in voltage. Unpackaged devices were tested in an air ambient and atmospheric pressures.

For small-signal tests, the down-state insertion loss and the up-state isolation were better than -0.2 dB and -25 dB up to 5 GHz, respectively. Experimental data was compared with HFSS and overall was in good agreement. High power testing was also performed on unpackaged devices for up to 30 W at 3 GHz for both 1 s and 20 s on-state times. Similar to DC micro-relay, forced air cooling was used on the devices. During

high power tests, microwelding occurred in the down-state at 18.5 W and 7 W for 1 s and 20 s on-state times, respectively. No self-actuation was observed in the up-state for both cases.

A lifetime test was performed on an unpackaged micro-relay operating in air ambient and at atmospheric pressure. Hot switching conditions were followed under 1 W of continuous RF power. The micro-relay test structure failed in the down-state after 3074 cycles due to microwelding.

For the third goal of this work, a process was developed to batch assemble devices in 4×1 array structures. A SS304 cantilever frame which carried four cantilevers with Pt-Rh contact bridges was assembled on a multi-layer PCB. The PCB consisted of three layers to allow segments of the transmission line and the DC path to connect beneath the surface. This configuration was essential to directly assemble a package lid on the PCB substrate. The package lid was chosen Vectra A130, an LCP based plastic for minimized RF performance deterioration. The transmission line segments were optimized for reduced impedance mismatch and reflection.

The footprint of a singulated test structure was 8.4 mm^2. The contact resistance and the pull-in voltage for the fabricated devices were lowest among the three designs, 78 V and 1.1 Ω for 115 V, respectively.

Small-signal RF tests were performed both for unpackaged devices operating in air ambient and atmospheric pressure and packaged devices operating in nitrogen and atmospheric pressure. For packaged devices, down-state insertion loss and up-state isolation were better than -0.25 dB, and -15 dB for up to 5 GHz, respectively. It was observed that RF performance of the packaged micro-relays were similar to the ones

without the packages. All the experimental data was compared to simulations and overall, both were in good agreement.

Packaged devices were also subjected to a high power test for 1 s actuation times up to 30 W of RF power at 3 GHz. The test structures failed in the down-state due to microwelding at 20 W with a measured S_{21} of -0.9 dB. There was no self-actuation in the up-state.

A lifetime test was carried out on a packaged micro-relay with nitrogen in atmospheric pressure. The devices were tested under hot switching conditions for 1 W (1 s on-state time) and 10 W (0.1 s on-state time) of power and failed in the down-state after 10,913 and 8,414 cycles respectively.

Low power lifetime study was not carried out in this work due to the lack of utility of the presented devices at low power levels.

6.2. Future work

In addition to the selection of hard metals with low electrical resistivity as contact materials, large contact forces are required to enhance high power handling capability for ohmic-contact micro-relays. Large contact forces are essential to break surface contaminations due to the humidity and hydrocarbons which are present in unpackaged devices but also to reduce the contact resistance for both unpackaged and packaged devices. As mentioned before, a lower contact resistance is highly desirable to reduce joule heating at the contact points and increase power handling. Therefore, a potential improvement for achieving very low contact resistance (<100 mΩ) and very high power handling (>10 A DC, 100 W RF) is by employing actuation forces in the order of tens of

mN. Large actuation forces can potentially be obtained by bi-stable latching mechanisms. Bi-stable mechanisms are favorable in switching technologies since they primarily offer zero stand-by power. Unlike in most electrostatically actuated switches where a certain amount of actuation voltage is required to keep the switch at on-state, bi-stable mechanisms can exhibit a snapping action on and off the signal line with no external force required to keep the beam in its current state. Large displacements coming with bi-stable actuation are also desirable from an RF performance point of view. In the up-state, with a large enough displacement away from the transmission line, the capacitance would be minimized and a very large isolation can be attained. Reciprocally, in the down-state, large actuation forces would reduce insertion loss due to a lower contact resistance.

Figure 6.1 shows a typical potential energy/force-displacement curve for a bi-stable mechanism. Units and material selection are arbitrary. The force offered by the bi-stable element to an actuator that is pushing it from the initial open position (in which it is fabricated) to the closed position is highly non-linear with the displacement. The reaction force (which is negative) initially increases in magnitude to a value F_{min}, and then decreases to zero at its unstable equilibrium point. After passing this position, the reaction force changes signs, indicating that the switch would close by itself. The positive force is the reaction force encountered in the opening of the switch when pushed from the opposite direction. The force on the closed contact can be tailored by positioning the bi-stable element at the distance from signal line that corresponds to the desired positive force. The two valleys in Figure 6.1(a) show the stable positions that would exist in the absence of external forces. In the case of the Si devices in Figure

6.1(b), reaction force is 1 mN at 9 μm displacement point. Reaction force is higher for Si structure due to higher Young`s modulus.

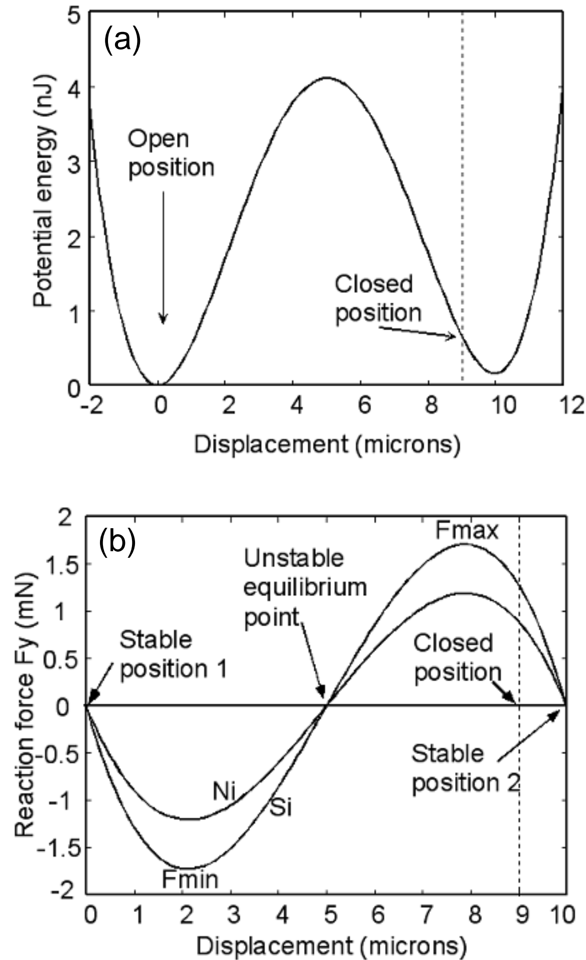

Figure 6.1: (a) Potential energy (Si) and (b) reaction force plots (Si and Ni) for a typical bi-stable element

Bi-stable mechanisms require large actuation forces to overcome potential energy barrier and snap into stable regions. Electrostatic actuation does not traditionally generate very large forces and might not be sufficient to drive bi-stable elements. Other actuation methods such as electrothermal actuation and magnetic actuation can be explored to overcome this force barrier. Previous studies showed feasibility to achieve bi-stable latching operations in microstructures [Que04, Mic05, Mic06].

Another potential future direction involves an improved fabrication and assembly process for higher throughput and yield. It is envisioned that automated pick-and-place assembly with robotic micro-grippers and conceivably a vision feedback mechanism might completely eliminate assembly imperfections contingent to manual assembly. For an automatic micro-relay assembly, individually fabricated pieces can be kept in different buffered containers. A vision control system can then detect each piece depending on the shape and position, and a robotic micro-gripper can pick-and-place those pieces into a full device assembly. The automated assembly scheme can even potentially allow the assembled device to be carried onto a testing bench and subjected to required mechanical and electrical tests prior to product release.

APPENDIX A

DESIGN OPTIMIZATION OF A CANTILEVER FOR LOW PULL-IN VOLTAGE

This section presents a theoretical model and an optimization process for a cantilever design to achieve low pull-in voltage. The theoretical contribution for the study has been led by Mr. Subhajit Banerjee, under the supervision of G. K. Ananthasuresh, both with Indian Institute of Science, Bangalore. Experimental evaluation of the theoretical model has been performed by the author of this thesis. Section A.1. provides a theoretical background for the mechanical cantilever design. This includes formulations for 1D lumped and distributed models. Section A.2. presents the theory for a structural optimization. Section A.3. describes geometric variations for the optimization and presents an experimental evaluation for the theoretical modeling.

A.1. Cantilever Design

The optimization process considered a set of variations based on the cantilever design presented in Chapter 4. General cantilever design principles are described in this section. The design process included coupled electromechanical analysis in terms of:

1. 1D lumped model,

2. 1D distributed model

Schematics of the current design are shown in Figs. A.1(a) and A.1(b). The design considered only the cantilever and neglected the contact bridge, heat sink and the micro-rod.

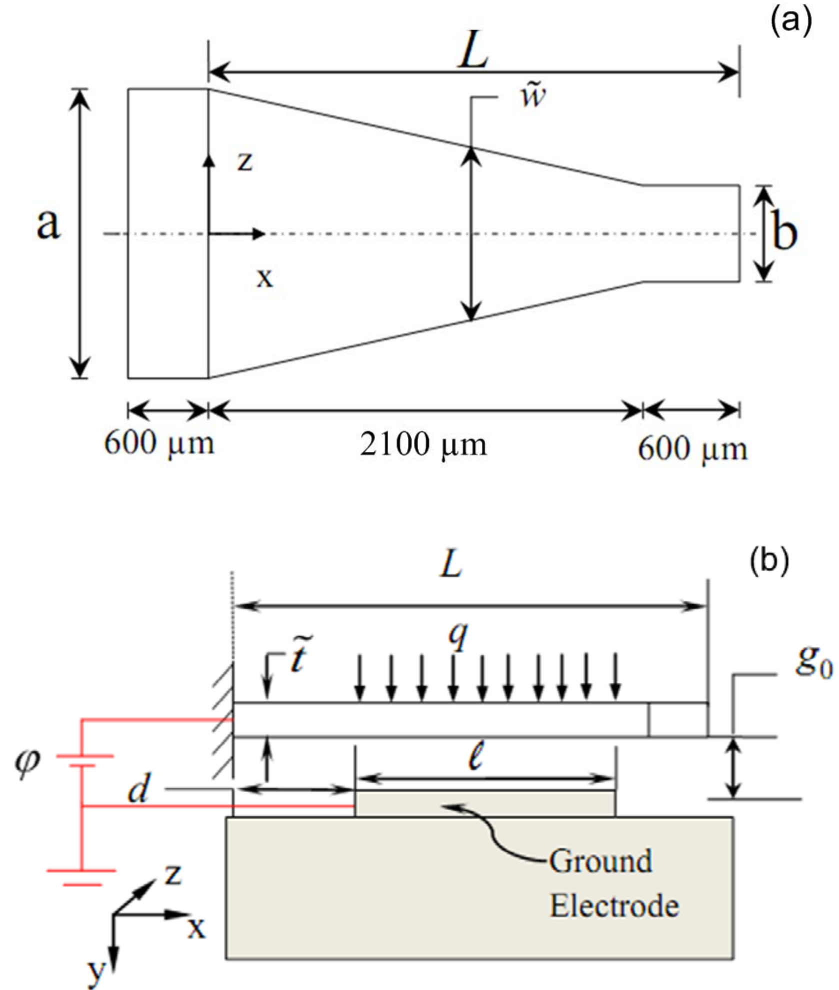

Figure A.1: Schematic of the existing design. (a) Top view, (b) side view

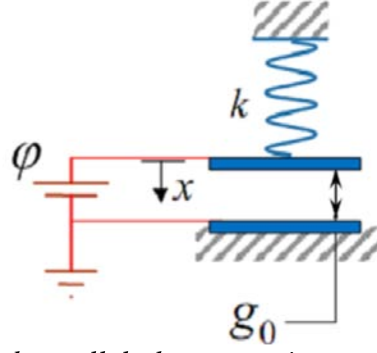

Figure A.2: A spring restrained parallel plate capacitor

A.1.1. Formulation for 1D lumped model

Figure A.2 represents an approximate 1D model of an electrostatically actuated cantilever. Here, the elastic properties of the cantilever are lumped into a linear translational spring, with stiffness k. The electrostatic interaction between the cantilever and the electrode underneath is lumped as a capacitance between parallel plates. The undamped dynamic response of the system to an actuation voltage ϕ is obtained by solving the governing differential equation of motion which is given below:

$$\tilde{L} = \text{Kinetic Energy - Potential Energy} = \frac{1}{2}m\dot{x}^2 - \left(\frac{1}{2}kx^2 - \frac{1}{2}\frac{\epsilon_0 A}{(g_0 - x)}\phi^2\right) \tag{A.1}$$

where, m is the lumped inertia of the system, x is the representative displacement along the chosen degree of freedom, ε_0 is the vacuum permittivity, A is the overlapping area between the electrodes, and g_0 is the initial gap between the electrodes. The equation A.1 can be rearranged into:

$$m\ddot{x} + kx = \frac{1}{2}\frac{\epsilon_0 A}{(g_0 - x)^2}\phi^2 \tag{A.2}$$

The above equation provides the simplest, most intuitive, and analytically solvable model.

The cross-sectional area of the cantilever, as shown in Figure A.1 varies along its length. This variation needs to be taken into account while calculating the stiffness. In Fig. A.3, let L be the total length of the beam and l the length of the electrode underneath it. The electrode is placed at a distance d from the fixed end and along a direction parallel to x axis. Here, it will be assumed that the initial load, (i.e., before bending), will be uniformly distributed over the beam. Therefore, the intensity of this uniformly distributed load (q) is: $\frac{1}{2l}\frac{\varepsilon_0 A}{{g_0}^2}\phi^2$. It is further assumed that this same load q will act throughout the entire range of deformation. If P is a virtual load applied at $x = L$ to obtain the tip deflection, then the strain energy of the beam in bending is:

$$U = \int_0^d \frac{[M_1(x)]^2}{2EI_{ZZ1}}\,dx + \int_d^{d+l} \frac{[M_2(x)]^2}{2EI_{ZZ1}}\,dx + \int_{d+l}^{L-b} \frac{[M_3(x)]^2}{2EI_{ZZ1}}\,dx + \int_{L-b}^{L} \frac{[M_4(x)]^2}{2EI_{ZZ2}}\,dx \quad \text{(A.3)}$$

Referring to Fig. A3, $I_{zz1}(x) = \tilde{w}(x)\tilde{t}^3/12$ (parts 1, 2, and 3), and $I_{zz2}(x) = b\tilde{t}^3/12$ (part 4) are the area moment of inertias of the tapered and the prismatic section of the beam, respectively.

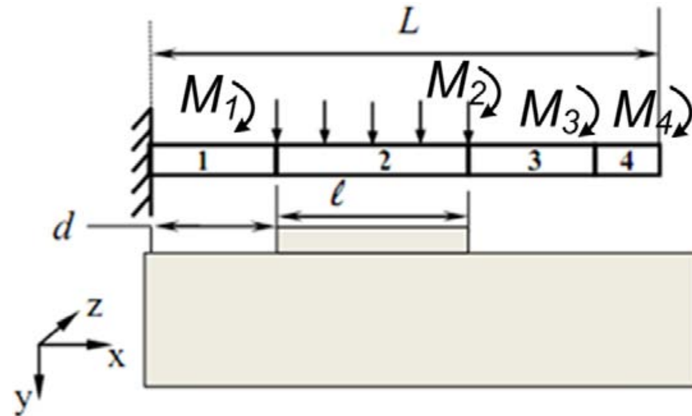

Figure A.3: Various parts of the beam, showing individual moments for each parts.

The moments of the various parts i.e., part 1, 2, 3, and 4 in Fig. A.3 are:

$$M_1(x) = \frac{1}{2}ql^2 + ql(d-x) + P(L-x)$$

$$M_2(x) = \frac{1}{2}q(l^2 + (x-d)^2) - ql(d-x) + P(L-x) \tag{A.4}$$

$$M_3(x) = P(L-x)$$

$$M_4(x) = M_3(x)$$

The deflection at the end point of the cantilever can be calculated from Castigliano's second theorem (i.e., $\delta_{endpoints} = \left(\frac{\partial U}{\partial P}\right)_{P=0}$). The cantilever stiffness for the given loading condition (i.e., electrode location and voltage difference), is calculated as:

$$k = \frac{ql}{\delta_{endpoint}} \tag{A.5}$$

A.1.2. Formulation for 1D distributed model

Euler-Bernoulli beam equation can be used on the existing design for 1 D distributed model. The Euler Bernoulli beam equation can be written as:

$$\begin{aligned}
\frac{\partial^2}{\partial x^2}\left(\tilde{E}I_{ZZ}(x)\frac{\partial^2 w(x,t)}{\partial x^2}\right) + \rho\tilde{w}\tilde{t}\frac{\partial^2 w(x,t)}{\partial t^2} &= 0 && \forall x \in [0,d], \\
&= \frac{\epsilon_0 \tilde{w}(x)}{2(g_0 - w(x,t))^2}\phi^2 && \forall x \in [d, d+l], \\
&= 0 && \forall x \in [d+l, L].
\end{aligned}$$

where w(x, t) denotes the transverse deflection of any point on the beam at a distance x from the fixed end, ρ is cantilever beam material density. Depending on the beam width, Young's modulus is:

$$\begin{aligned}
\tilde{E} &= \frac{E}{(1-\nu^2)} \qquad \forall \quad \tilde{w} \geq 5\tilde{t} \qquad \text{i.e., wide beams,} \\
&= E \qquad \forall \quad \tilde{w} \leq 5\tilde{t} \qquad \text{i.e., narrow beams}
\end{aligned} \tag{A.6}$$

The 1D distributed model can be solved by the displacement-based beam finite element method coupled with electrostatic analysis. Iterative relaxation scheme is used

to solve the coupling between electrical and mechanical domains. Solving the corresponding Dirichlet boundary value problem, with the tip contacting after removing the actuation voltage, yields the recoil force with which the switch will come out of contact from the transmission line. Figure A.4(a) shows the cross section of the cantilever with actuation gap (g_a) and contact gap (g_c) whereas Figure A.4(b) exhibits Dirichlet boundary value problem and recoil force. The variation of pull-in voltage with the actuation gap for the existing design is shown in Figure A.5. The model considers that the actuation gap is always larger than the contact gap. Calculated recoil force for the actual design was 3.5 mN.

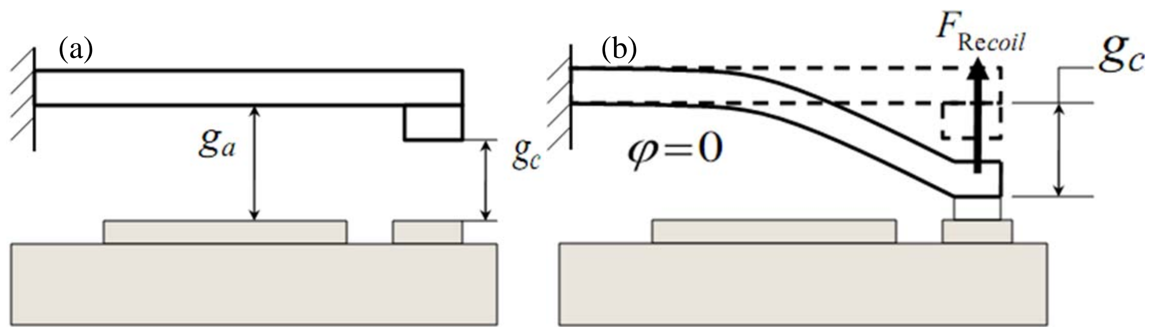

Figure A.4: Model used for beam FEM showing (a) actuation and contact gaps (b) Dirichlet boundary value problem with recoil force

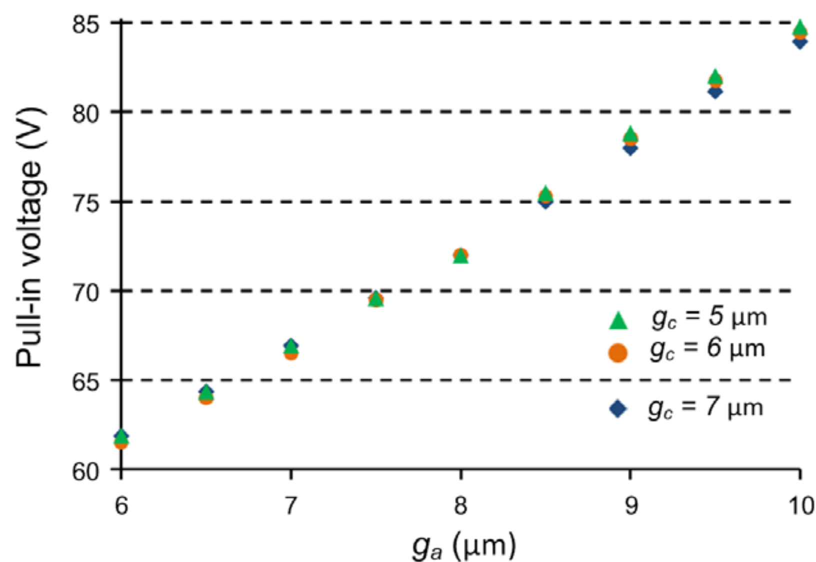

Figure A.5: Variation of pull-in voltage with different actuation and contact gaps

A.2. Structural optimization

As mentioned in the introductory chapters, power handling of the ohmic-contact type MEMS switches is limited by the interface problems at hot switching conditions, such as melting of contact materials at high temperatures and an increase of contact resistance beyond useful range.

With the aforementioned limitations in mind the present section focuses on obtaining a design which would have:

- Low pull-in voltage
- Large recoil force at no-load condition. This will alleviate the adhesion problem at the contact region.

For the optimization process, Euler Bernoulli beam equation was assumed to be valid throughout the formulation. Considering a certain maximum volume of material (V_{max}) having Young's modulus E and Poisson's ratio v, the micro-relay should undergo a deflection Δ under the action of a voltage difference ϕ. It was also considered that the width and the thickness of any section of the switch is are $w(x)$ and t, respectively. The cross-sectional area is $A = w(x)t$. The area moment of inertia of any cross-section of the switch is then given by:

$I = \frac{wt^3}{12}$; where $\alpha = \frac{t^2}{12}$

The structural optimization problem statement can be constructed as:

Minimize $\frac{1}{F_{recoil}}$ where it is defined as:

$$\frac{1}{F_{Recoil}} = \frac{1}{\tilde{E}\Delta\alpha}\int_0^L \frac{(L-x)^2}{A}\,dx \quad \text{(A.7)}$$

A is subject to:

$$\begin{aligned} \Lambda_1 &: \Delta - \int_0^L \frac{M_l m_u}{A\tilde{E}\alpha}\, dx \leq 0 \\ \Lambda_2 &: \int_0^L A\, dx - V_{max} \leq 0 \end{aligned} \tag{A.8}$$

where,

M_l is the bending moment due to the mechanical load applied by the voltage bias, and m_u is the bending moment due to a virtual unit load applied at the end of the micro-relay.

Data is:

$$\phi, t, \Delta, L, E, \nu, \tilde{E}(= \frac{E}{(1-\nu^2)})\text{ (for wide beams)}$$

The solution considered SS304 cantilever material, 50 µm thickness, and $\Delta = 8$ µm. Solving with $\Lambda_1 \neq 0$ and $\Lambda_2 \neq 0$ (i.e., both of the constraints are active), yields the shape shown in Fig. A.6(a). For the same data set, but with $\Lambda_1 = 0$ and $\Lambda_2 \neq 0$ (i.e., volume constraint is inactive whereas the end-point deflection constraint is active) will yield the shape shown in A.6(b). Pull-in voltage was found 50 V.

The design optimization using tapered profiles motivates a pull-in voltage analysis for different shapes.

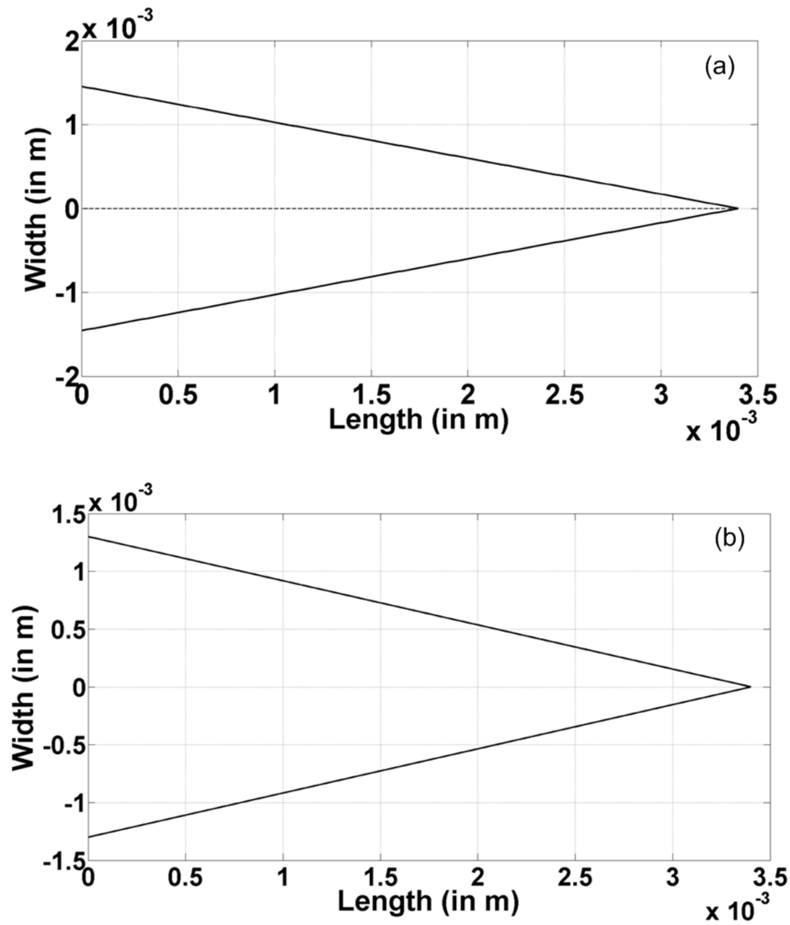

Figure A.6: Result of structural optimization problem. (a) Shape-1, $\Lambda_1 \neq 0$ and $\Lambda_2 \neq 0$, (b) Shape-2 $\Lambda_1 = 0$ and $\Lambda_2 \neq 0$.

A.3. Investigation of various shapes

A.3.1. Theoretical model

This section presents the determination of the pull-in voltage for six configurations, each having the same volume of material with the original design presented in Chapter 4. Figure A.7 represents the generic shape of such configurations.

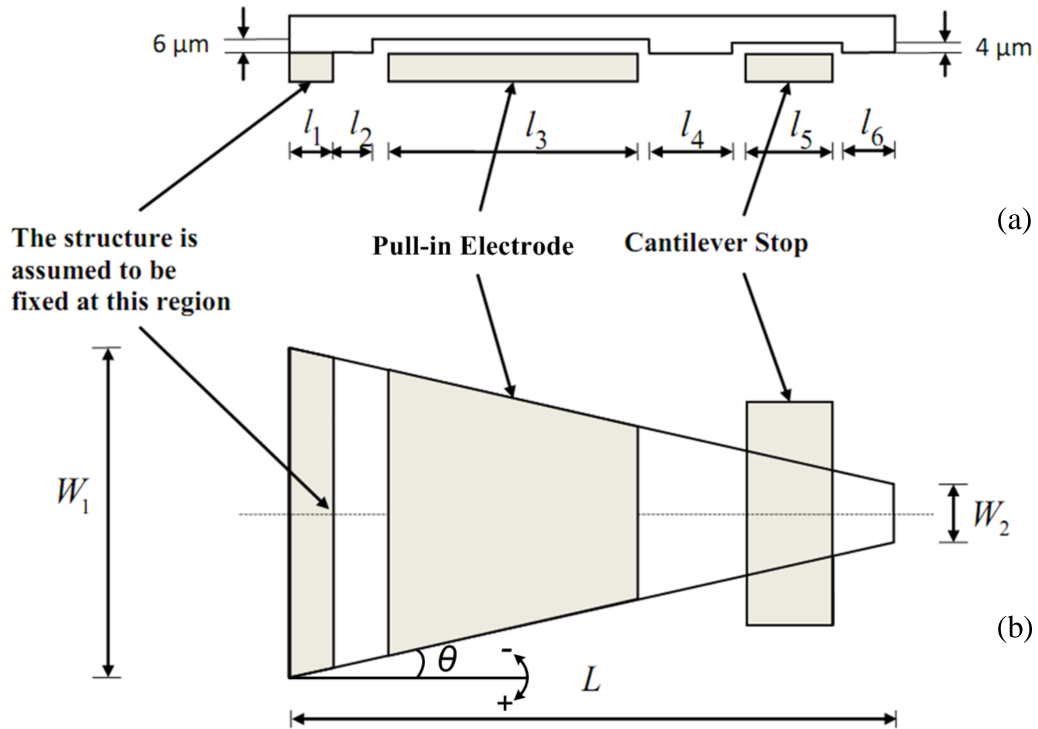

Figure A.7: Generic shape of the optimized structure. (a) Side view, (b) top view.

The critical lengths l_1-l_6 are presented in the table below:

Table A.1: Critical lengths for the optimized design.

Length	Value (µm)
l_1	500
l_2	500
l_3	1430
l_4	130
l_5	600
l_6	200
L	3400

The angle θ represents the slope of the tapered profiles. A negative slope is defined as the angle of the tapered side wall deviating from the horizontal line in a counter clockwise direction as for the configuration in Figure A.7. A positive slope is defined as the angle deviating in a clockwise direction.

For each of the six shapes considered, the thickness was fixed to 50 µm. In

addition, the end having width W_1 was fixed, while the other end (width W_2) was in the free condition. Width W_2 was varied uniformly from 572 µm to 2292 µm to generate six different shapes. Width W_1 was calculated so as to keep the volume to be equal to the original design. The clearance everywhere was set to 10 µm. The material was selected as SS304 as in the original design. The values of the slope, W_1 and W_1 for six configurations are tabulated below (Table A.2).

Table A.2: Slope and width values for different configurations

Configuration	Slope (in deg.)	W_1 (in µm)	W_2 (in µm)
1	-13.71	2231.34	572.14
2	-6.11	1769.29	1041.69
3	-0.92	1462.58	1353.78
4	1.70	1308.43	1510.39
5	6.9	1000.53	1823.33
6	14.47	538.48	2292.88

Figure A.8 shows pull-in voltage calculations following 1D beam FEM solution introduced earlier.

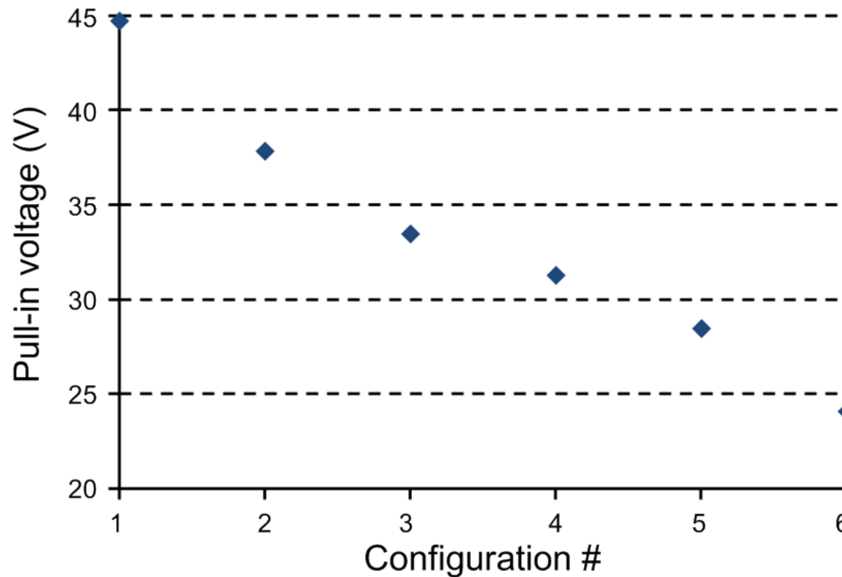

Figure A.8: Modeled pull-in voltages for six configurations

A.3.2. Experimental evaluation

This section presents the implementation of all six configurations to experimentally evaluate pull-in voltages modeled in the previous section. Figure A.9 shows the design of Configuration-2 which is chosen randomly. A solid cantilever is located on a PCB circuit. A pair of alignment posts is used to align and fix the cantilever in its place. A pull-in electrode is used as a gate terminal and biased with a source electrode for electrostatic actuation. A contact pad is located on the PCB underneath the distal end of the cantilever. It acts as a drain terminal. Following sub-sections details fabrication and testing for the structure.

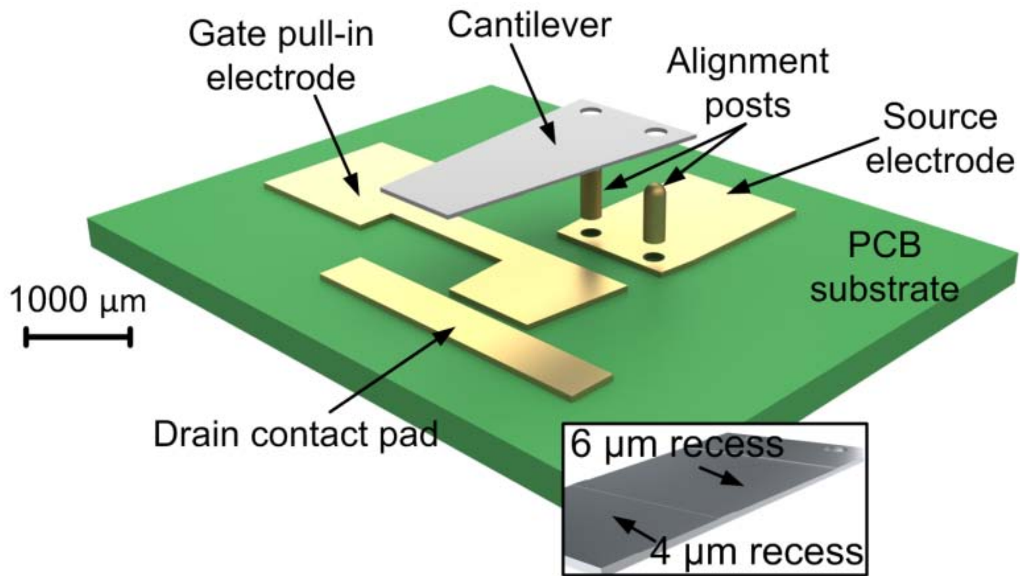

Figure A.9: Exploded view of the test structure for Configuration-2. Gold posts align and hold the cantilever over gold-coated copper traces on the PCB. The cantilever has two recessed regions with depths 6 µm and 4 µm over the ground electrode and contact pad, respectively (shown upside down in the inset).

A.3.2.1. Fabrication

The cantilever was photochemically etched from 50 µm-thick SS304 foils

(Kemac Technology Inc., CA). The recesses of 6 μm and 4 μm were machined using μEDM. Perforations of 300 μm diameter were located for the alignment and the attachment on the PCB (Fig. A.10(a)).

A 600 μm-thick Rogers 4003 was used as the substrate (Advanced Circuits Inc., CO). Metal interconnect traces of 70 μm-thick Cu provided bias electrodes and contact pad. In such PCBs, 4 μm thick Ni was used as an adhesion layer on the Cu base, and 0.15 μm thick outer gold layer provided an electrical contact. Through vias were located on the PCB for the subsequent attachment of the cantilever.

For the assembly, alignment posts (1000 μm-height; 300 μm-diameter), were machined from gold wire using μEDM, and tightly fitted into the isolated-vias on the PCB (Fig. A.10(b)). Conical wire tips facilitated the insertion of the cantilever. The cantilever was assembled over the posts and fixed by applying conductive epoxy (Creative Materials). The flatness of the cantilever was maintained during the assembly process with the help of a high resolution laser displacement sensor (Keyence LK-G32).

The test circuit (Fig.A.11(a)-(b)) used the variable gate actuation voltage (V_G) and constant drain voltage (V_D) as inputs. Output voltage V_{OUT} was monitored to detect the pull-in. V_G was increased in 50 mV steps from 30 V to 45 V. When the test structure was in off-state V_{OUT} was equal to zero (denoted as $V_{OUT-OFF}$). When a pull-in occurred, V_{OUT} was approximately $V_D/2 = 1$ V due to the relationship given in Fig. A.11b (denoted as V_{OUT-ON}). R_{ON} represented the on-state resistance and included contact resistance and the parasitics. Test was run in air ambient and atmosphere.

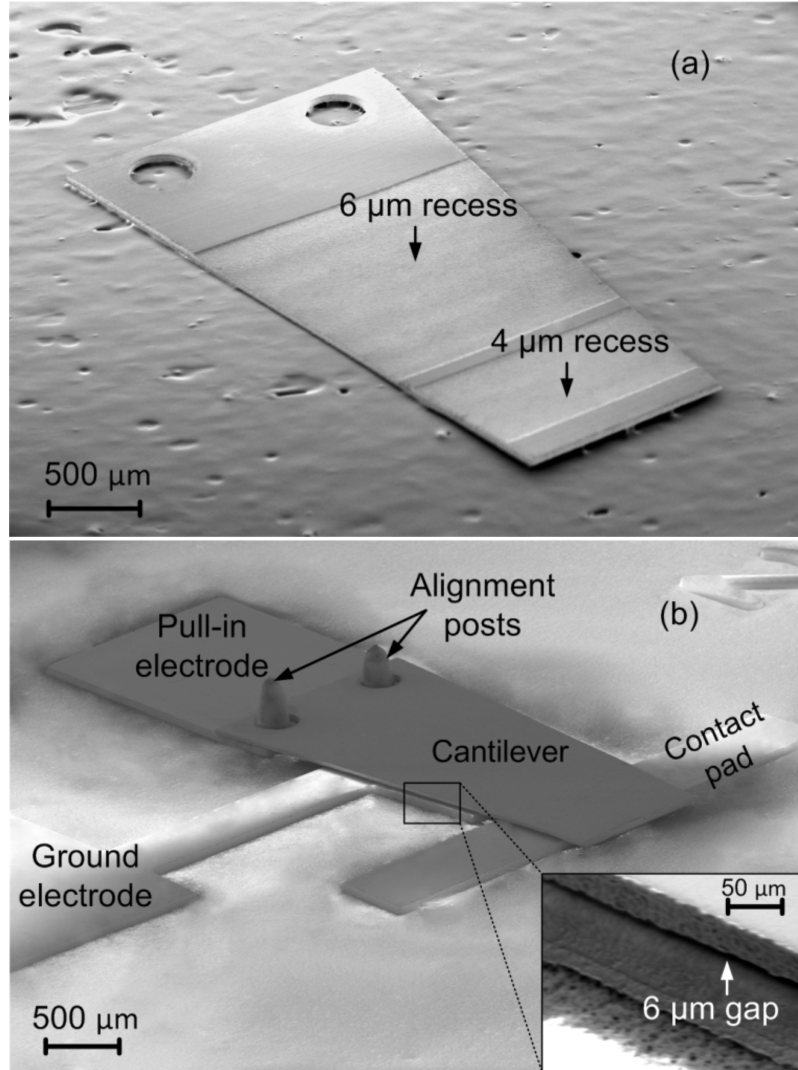

Figure A.10: SEM micrographs for Configuration-2 test structure. (a) Cantilever is shown upside down with recessed regions. (b) Assembled structure with 6 µm gap between the cantilever and the ground electrode shown in the inset.

A.3.2.2. Testing

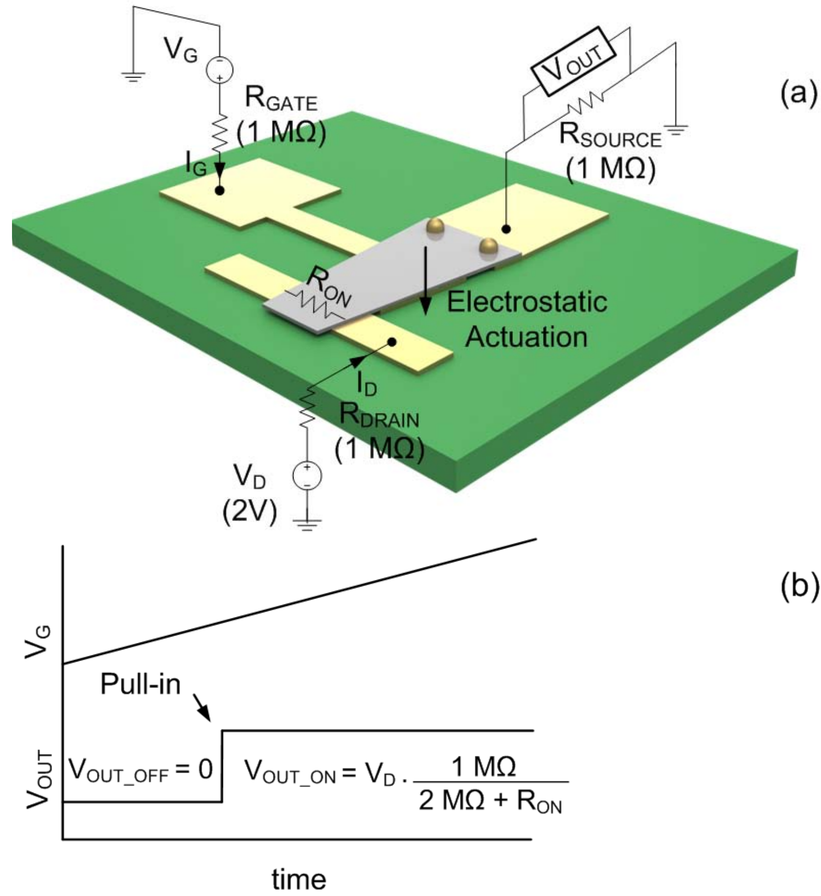

Figure A.11: (a) Circuitry for testing, using variable gate actuation voltage (V_G), and constant drain voltage V_D as the input. R_{ON} was the on-state resistance, and was combination of contact resistance and all the parasitic resistances. (b) Actuation concept showing $V_{OUT-OFF}$ and V_{OUT-ON} conditions

Figure A.12 shows the pull-in behavior of the Configuration-2 test structure. The pull-in occurred at 40.95 V. Further increase in actuation voltage caused the V_{OUT} to remain constant at approximately 1 V since R_{ON} was negligibly low compared to fixed resistors. The experimental data was in good agreement with the theoretically modeled pull-in voltage of 37.81 V by only a 7% deviation. Figure A.13 shows the experimental pull-in voltages of all six configurations and compare them to modeled values. Table A.3

summarizes the data for all the configurations including actuation and recoil forces estimated from pull-in and turn-off voltages in the hysteresis study.

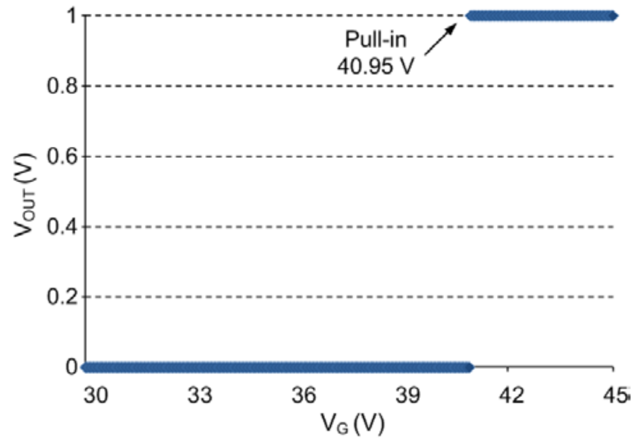

Figure A.12: Experimental result showing change of V_{OUT} with the actuation voltage. V_{OUT} was zero until pull-in occurred at 40.95 V. Beyond this point, V_{OUT} remained constant at approximately 1 V.

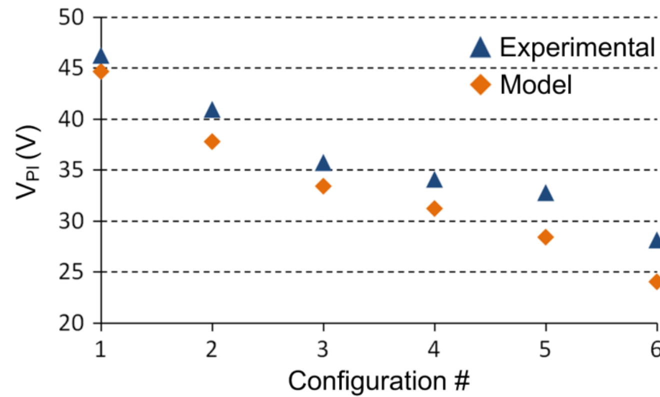

Figure A.13: Experimentally found pull-in voltage compared to model for all six configurations

Table A.3: Summary of pull-in and turn-off voltages and associated actuation and recoil force estimates for all six configurations

Pull-in Voltage (Model) (V)	Pull-in Voltage (Experiment) (V)	Error %	Turn-off Voltage (V)	Actuation force (mN)	Recoil force (mN)	Turn-on time (ms)
44.69	46.25	3.491	31.15	2.09	0.81	4-5
37.81	40.95	8.305	28.25	1.65	0.79	4-6
33.44	35.75	6.908	26.65	1.27	0.72	5-6
31.25	34.1	9.120	26.05	1.16	0.69	5-7
28.44	32.8	15.331	25.15	1.08	0.64	5-8
24.06	28.15	16.999	20.05	0.81	0.52	6-8

BIBLIOGRAPHY

[Abb78] W. H. Abbott, and W. K. Campbell "Frictional polymer formation on precious metals. Experimental observation," *Proceedings of the 9th International Conference on Electrical Contact Phenomena, Chicago, USA*, pp. 359–363, 1978.

[Aga02] A. Agarwal, S. Ryu, C. Capell, J. Richmond, J. W. Palmour, B. Phan, J. Stambaugh, H. Bartlow, and K. Brewer, "SiC BJT's for High Power Switching and RF Applications," *Proc. Materials Research Society Silicon Carbide 2002 – Materials, Processing and Devices*, 742, K7.3, 2002.

[Alm07] L. Almeida, R. Ramadoss, R. Jackson, and K. Ishikawa, Q. Yu, "Laterally actuated multicontact MEMS relay fabricated using MetalMUMPS process: experimental characterization and multiscale contact modeling," *Journal of Micro/Nanolithography, MEMS, and MOEMS*, 6, (2), pp.023009-1–10, 2007.

[Ant82] M. Antler, "The Application of Palladium in Electronic Connectors" *Platinum Metals Review*, 26, (3), pp. 106–117, 1982.

[Ash01a] W. R. Ashurst, C. Yau, and C. Carraro, "Alkene based monolayer films as anti-stiction coatings for polysilicon MEMS," *Sensors and Actuators A*, 91, (3), pp. 239-248, 2001.

[Ash01b] W. R. Ashurst, C. Yau, and C. Carraro, "Dichlorodimethylsilane as an anti-stiction monolayer for MEMS: A comparison to the octadecyltrichlosilane self-assembled monolayer," *Journal of Microelectromechanical Systems*, 10, (1), pp. 41-49, 2001.

[Aut09] http://www.automationdirect.com/adc/Overview/Catalog/Relays_-z-_Timers/Solid-State_Relays, referenced June 2011.

[Bow64] F. P. Bowden, and D. Tabor, *Friction and Lubrication of Solids, Vol. 2*. Oxford, UK: Oxford University Press, 1964.

[Boz00] C. Bozler, R. Drangmeister, S. Duffy, M. Gouker, J. Knecht, L. Kushner, R. Parr, S. Rabe, and L. Travis, "MEMS microswitch arrays for reconfigurable distributed microwave components," I*EEE International Microwave Symposium* Dig., pp. 153–156, 2000.

[Bro98] E. R. Brown, "RF-MEMS switches for reconfigurable integrated circuits," *IEEE Trans. Microwave Theory and Techniques*, 46, (11), pp. 1868–1880, 1998.

[But08] R. Buttiglione, S. Catoni, G. de Angelis, M. Dispenza, A. Fiorello, K. Kautio, M. Ladhes, R. Marcelli, and K. Ronka, "Alumina and LTCC Technology for RF MEMS Switches and True Time Delay Lines," *Microwave Integrated Circuit Conference, EuMIC 2008*, pp. 366–69, 2008.

[Cae09] K. Van Caekenberghe, "RF MEMS on the Radar," IEEE Microwave Magazine, 10, (6), pp. 99–116, 2009.

[Cet03] B.A. Cetiner, H.P. Chang, J.Y. Qian, M. Bachman, G.P. Li, and F. De Flaviis, Monolithic integration of RF MEMS switches with diversity antenna on PCB substrate, *IEEE Trans. on Microwave Theory and Techniques*, 51, 332–335, 2003.

[Cha03] R. Chan, R. Lesnick, D. Becher, and M. Feng, "Low-actuation voltage RF MEMS shunt switch with cold switching lifetime of seven billion cycles," *Journal of Microelectromechanical Systems*, 12, pp. 713–719, 2003.

[Cha05] H. Chang, J. Qian, B. A. Cetiner, F. D. Flaviis, M. Bachman, and G. P. Li, "Design and Process Considerations for Fabricating RF MEMS Switches on Printed Circuit Boards", *Journal of Microelectromechanical Systems*, 14, (6), pp. 1311–1322, 2005.

[Cha87] W. R. Chang, I. Etsion, and D. B. Bogy, "An Elastic-plastic Model for the Contact of Rough Surfaces," Transactions of the ASME Journal of Tribology, 109, pp. 257–263, 1987.

[Chr04] D. Christiansen, C.K. Alexander, and R.K. Jurgen, *Standard Handbook of Electronic Engineering, 5th Edition*, McGraw-Hill, Boston, MA, 2004.

[Che09] S. Cheng, P. Rantakari, R. Malmqvist, C. Samuelsson, T. Vaha-Heikkila, A. Rydberg, and J. Varis, "Switched Beam Antenna Based on RF MEMS SPDT Switch on Quartz Substrate," *IEEE Antennas and Wireless Propagation Letters*, 8, pp. 383–386, 2009.

[Cho09] J-Y. Choi, J. Ruan, F. Coccetti, and Stepan Lucyszyn, "Three-Dimensional RF MEMS Switch for Power Applications," *IEEE Trans. on Industrial Electronics*, 56, (4), pp. 1031–1039, 2009.

[Cim94] S. Cimtalay, and R. E. Fulton, "Parameter design of heat sink: multiple trade-offs," *Proc. ASME Winter Annual Meeting*, EEP-9, pp.53–59, 1994.

[Cou04] R. A. Coutu, P. E. Kladitis, K. D. Leedy, and R. L. Crane, "Selecting metal alloy electric contact materials for MEMS switches," *Journal of Micromechanics and Microengineering*, 14, pp. 1157–1164, 2004.

[Cre08] http://www.cree.com/products/power_docs2.asp, referenced June 2011.

[Dea07] R. Dean, J. Weller, M. Bozack, B. Farrell, K. Jauniskis, J. Ting, D. Edell, and J Hetke, "Micromachined LCP connectors for packaging MEMS devices in biological environments," *Journal of Microelectronics and Electronic Packaging*, 4, (1), pp. 17–22, 2007.

[Der97] G. Dereli, T. Cagin, M. Uludogan, and M. Tomak, "Thermal and Mechanical Properties of Pt-Rh Alloys," *Philosophical Magazine Letters*, 75, pp. 209–217, 1997.

[Duf01] S. Duffy, C. Bozler, S. Rabe, J. Knecht, L. Travis, P. Wyatt, C. Keast and M. Couker, "MEMS microswitches for reconfigurable microwaves circuitry," *IEEE Microwave and Wireless Components Letters*, 11, (3), pp. 106–108, 2001.

[Ehr96] W. Ehrfeld, H. Lehr, F. Michel, and A. Wolf, "Microelectro Discharge Machining as a Technology in Micromachining," *SPIE's Symposium on Micromachining and Microfabrication*, 2879, pp. 332–337, 1996.

[Fai09] http://www.fairchildsemi.com/ds/IS/ISL9V2040D3S.pdf, referenced June 2011.

[Gho05] B. Ghodsian, C. Jung, B. A. Cetiner, and F. De Flaviis, "Development of RF-MEMS Switch on PCB Substrates With Polyimide Planarization," *IEEE Sensors Journal*, 5, (5), pp. 950–955, 2005.

[Gra04] P. D. Grant, M.W. Denhoff, and R. R. Mansour, "A comparison between RF MEMS switches and semiconductor switches," *International Conference on MEMS, NANO and Smart Systems*, pp. 514–521, 2004.

[Gre66] J. A. Greenwood, and J. B. P. Williamson, "The contact of nominally flat surfaces," Proc. Royal Society A: Mathematical, Physical and Engineering Sciences, 295, pp. 300–319, 1966.

[Gol01] C. Goldsmith, J. Ehmke, A. Malczewski, B. Pillans, S. Eshelman, J. Yao, Z. Brank, and M. Eberly, "Lifetime characterization of capacitive RF MEMS switches," *IEEE MTT-S International Microwave Theory and Techniques Symposium Proc.*, pp. 227–230, 2001.

[Gol95] C. L. Goldsmith, T. H. Lin, B. Powers, W. R. Wu, and B. Norvell, "Micromechanical membrane switches for microwave applications," *IEEE MTT-S International Microwave Theory and Techniques Symposium Proc.*, pp.91–94, 1995.

[Gol96] C. L. Goldsmith, J. Randall, S. Eshelman, T. H. Lin, D. Denniston, S. Chen, and B. Norvell, "Characteristics of micromachined switches at microwave frequencies," *IEEE MTT-S International Microwave Theory and Techniques Symposium Proc.*, pp. 1141–1144, 1996.

[Gol98] C. L. Goldsmith, S. Eshelman, Z. Yao, T. H. Lin, and D. Denniston, "Performance of low-loss RF MEMS capacitive switches," *IEEE Microwave Guided Wave Letters*, 8, pp. 269–271, 1998.

[Har00] K. F. Harsh, B. Su, W. Zhang, V. B. Bright, and Y. C. Lee, "The realization and design considerations of a flip-chip integrated MEMS tunable capacitor," *Sensors and Actuators A,* 80, (2), pp. 108–118, 2000.

[Ho03] K. H. Ho, and S. T. Newman, "State of the art electrical discharge machining (EDM)," *International Journal of Machine Tools & Manufacture*, 43, pp. 1287–1300, 2003.

[Hol68] R. Holm, *Electric Contacts*, Springer-Verlac, Berlin, Germany, 1968.

[Hon04] J. S. Hong, S. G. Tan, Z. Cui, L. Wang, R. B. Greed, and D. C. Voyce, "Development of high power RF MEMS switches," *Proc. ICMMT 4th International Conference on Microwave and Millimeter Wave Technology*, pp. 7–10, 2004.

[Hou07] Z. H. Hou, Z. W. Liu, and G. W. Hu, "Study on the reliability of capacitive shunt RF MEMS switch", *Proc. International Conference on Electronics Packaging Technology*, pp. 599–602, 2007.

[Hua01] J. M. Huang, K. M. Liew, C. H. Wong, S. Rajendran, M. J. Tan, and A. Q. Liu, "Mechanical design and optimization of capacitive micromachined switch," *Sensors and Actuators A*, 93, pp. 273–285, 2001.

[Huf06] G. H. Huff, and J. T. Bernhard, "Integration of packaged RF MEMS switches with radiation pattern reconfigurable square spiral microstrip antennas," *IEEE Trans. on Antennas and Propagation*, 54, (2), pp. 464–469, 2006.

[Hym99] D. Hyman and M. Mehregany, "Contact physics of gold microcontacts for MEMS switches," *IEEE Trans. on Components & Packaging Technologies*, 22, (3), pp. 357–364, 1999.

[Ish05] H. Ishida, Y. Hirose, T. Murata, Y. Ikeda, T. Matsuno, K. Inoue, Y. Uemoto, T. Tanaka, T. Egawa, and D. Ueda, "A high-power RF switch IC using AlGaN/GaN HFETs with single-stage configuration," *IEEE Trans on Electron Devices*, 52, (8), pp. 1893–1899, 2005.

[Jac06] C. B. Jacobina, I. S. D. Freitas, E. R. C. D. Silva, A. M. N. Lima, and R. L. D. A. Ribeiro, "Reduced Switch Count DC-link AC–AC Five-Leg Converter," *IEEE Trans. on Power Electronics*, 21, (5), 2006.

[Jen05] B. D. Jensen, L. L. W. Chow, K. Huang, K. Saitou, J. L. Volakis, and K. Kurabayashi, "Effect of Nanoscale Heating on Electrical Transport in RF MEMS Switch Contacts," *Journal of Microelectromechanical Systems*, 14, (5), pp. 935–946, 2005.

[Ke08] F. X. Ke, J. M. Miao, and J. Oberhammer, "A Ruthenium-Based Multimetal-Contact RF MEMS Switch With a Corrugated Diaphragm," *Journal of Microelectromechanical Systems*, 17, (6), pp. 1447–1459, 2008.

[Kim01a] B. H. Kim, T. D. Chung, and C.H. Oh, "A new organic modifier for anti-stiction," *Journal of Microelectromechanical Systems*, 10, (1), pp. 33–40, 2001.

[Kim01b] M. Kim, J. B. Hacker, R. E. Mihailovich, and J. F. DeNatale, "A monolithic MEMS switched dual-path power amplifier," *IEEE Microwave and Wireless Components Letters*, 11, (7), pp. 285–286, 2001.

[Kim08] J-M. Kim, S. Lee, C-W. Baek, Y. Kwon, and Y-K. Kim, "Cold- and hot switching lifetime characterizations of ohmic-contact RF MEMS switches," *IEICE Electronics Express*, 5, (11), pp. 418–423, 2008.

[Kim09] T. Kim, M. U. Faz, L. Vietzorreck, "Investigation and optimization of transitions in an LTCC based RF MEMS switching matrix for space applications," *Asia Pacific Microwave Conference, APMC 2009*, pp. 988–991, 2009.

[Koc00] O. Koch, W. Ehrfeld, and F. Michel, "Micro-Electro Discharge Machining - Application, Strategy and Technology," *Proc. 2nd International Workshop on Microfactories (IWMF)*, pp. 79–82, 2000.

[Kre05] L.C. Kretly, A. A. S. Tavora, and C. E. Capovilla, "MEMS Switch for Wireless Communication Circuits: Process and Simulation", *IEEE MTT-S International Microwave Theory and Techniques Symposium Proc.*, pp. 427–429, 2005.

[Kwo07] H. Kwon, D-J. Choi, J.-H. Park, H.-C. Lee, Y.-H. Park, Y.-D. Kim, H.-J. Nam, Y.-C. Joo, and J.-U. Bu, "Contact Materials and Reliability for High Power RF-MEMS Switches," *Proc. 20th IEEE International Conference on Microelectromechanical Systems (MEMS'07)*, pp. 231–234, 2007.

[Lac06] B. Lacroix, A. Pothier, and A. Crunteanu, "Sub-microsecond RF MEMS switched capacitors" , *IEEE 36th European Microwave Conference Proc.*, 55, (6), pp. 1314–1321, 2006.

[Lam04] J. Lampen, S. Majumder, and R. Morrison, "A wafer-capped, high-lifetime ohmic MEMS RF switch," *Journal of RF and Microwave CAE*, 14, (4), pp. 338–344, 2004.

[Lar91] L. E. Larson, R. H. Hackett, M. A. Melendes, and R. F. Lohr, "Micromachined microwave actuator (MIMAC) technology-a new tuning approach for microwave integrated circuits," *IEEE Microwave and Millimeter-Wave Monolithic Circuits Symposium Dig.*, pp. 27–30, 1991.

[Lee02] H. S. Lee, C. H. Leung, J. Shi, and S.C. Chang, "Electrostatically actuated copper-blade microrelays," *Sensors and Actuators A*, 100, pp. 105–113, 2002.

[Lee06] H. Lee, R. A Coutu, S. Mall, and K. D. Leedy, "Characterization of metal and metal alloy films as contact materials in MEMS switches," *Journal of Micromechanics and Microengineering*, 16, pp. 557–563, 2006.

[Lee09] K.-Y Lee, S. Y. Meng, A. K. Sen, N. G. Ing, and W. Hong, "Integration of RF MEMS switch with MMIC pHEMT and passive devices on GaAs," *IEEE International Symposium on Radio Frequency-Integration Technology, RFIT 2009*, pp. 288–291, 2009.

[Li00] Z. H. Li, D. C. Zhang, T. Li, W. Wang, and G. Wu, "Bulk micromachined relay with lateral contact," *Journal of Micromechanics and Microengineering*, 10, pp. 329–333, 2000.

[Li09] T. Li, "Ultrasonic batch mode micromachining and its application to piezoelectric sensors for fine needle aspiration biopsy," *Ph. D. Thesis, University of Michigan,* 2009.

[Lin02] Y. Ling, "On current carrying capacities of PCB traces," *Proc. Electronic Components Conference*, pp. 1683-1693, 2002.

[Liu01] Y. Liu, Y, Li, T. Abe, Y. Haga, and M. Esashi, "A thermomechanical relay with microspring contact array," *Proc. 14th IEEE International Conference on Microelectromechanical Systems (MEMS'01)*, pp. 220–223, 2001.

[Luc04] S. Lucyszyn, "Review of radio frequency microelectromechanical systems technology," *IEEE Proc. Science, Measurement & Technology*, 151, (2), pp. 93–103, 2004.

[Mab02] R. Maboudian, W. R. Ashurst, and C. Carraro, "Tribological challenges in micromechanic systems," *Tribology Letters*, 12, (2), pp. 95–100, 2002.

[Mac04] J. Maciel, S. Majumder, R. Morrison, and J. Lamen, "Lifetime characteristics of ohmic MEMS switches (Invited Paper)," *Proc. SPIE-International Society for Optical Engineering*, pp. 9–14, 2004.

[Mad95] C. Madhusadana, *Thermal Contact Conductance*, Springer-Verlag, New York, 1995.

[Mad07] M. Maddela, and R. Ramadoss, "A MEMS-based tunable coplanar patch antenna fabricated using PCB processing techniques," *Journal of Micromechanics and Microengineering*, 17, pp. 812–819, 2007.

[Mah10] R. Mahameed, and G. M. Rebeiz, "A High-Power Temperature-Stable electrostatic RF MEMS Capacitive Switch Based on a Thermal Buckle-Beam Design," *Journal of Microelectromechanical Systems*, 19, (4), pp. 816–826, 2010.

[Maj97] S. Majumder, N. E. McGruer, P. M. Zavracky, G. G. Adams, R. H. Morrison, and J. Krim, "Measurement and modeling of surface micromachined, electrostatically actuated microswitches," *Proc.* IEEE International Conference on Solid-State Sensors and Actuators (*Transducers)*, 1-2, pp.1145–1148, 1997.

[Maj03a] S. Majumder, J. Lampen, R. Morrison, and J. Maciel, "MEMS switches," *IEEE Instrumentation & Measurement Magazine*, pp. 12–15, 2003.

[Maj03b] S. Majumder, J. Lampen, R. Morrison, and J. Maciel, "A packaged, high-lifetime ohmic MEMS RF switch," *IEEE MTT-S International Microwave Theory and Techniques Symposium Proc.*, 3, pp. 1935–1938, 2003.

[Mas90] T. Masaki, K. Kawata, and T. Masuzawa, "Micro electro-discharge machining and its applications," *Proc. 3rd IEEE International Conference on Microelectromechanical Systems (MEMS'90)*, pp. 21-26, 1990.

[McG06] N. E. McGruer, G. G. Adams, L. Chen, Z. J. Guo, and Y. Du, "Mechanical, Thermal, and Material Influences on Ohmic-contact-type MEMS Switch Operation," *Proc. 19th IEEE International Conference on Microelectromechanical Systems (MEMS'06)*, pp. 230–233, 2006.

[Mer05] D. Mercier, K. Van Caekenberghe, and G. M. Rebeiz, "Miniature RF MEMS switched capacitors," *IEEE MTT-S International Microwave Theory and Techniques Symposium Proc.*, pp.745–748, 2005

[Mic05] A. Michael, K. Yu , M. Mackenzie, and C. Y. Kwok, "Out-of-plane Electrothermally Actuated Bistable Buckled Microbridge Actuator," *IEEE Sensors 2005,* pp. 596–699, 2005.

[Mic06] A. Michael, and C. Y. Kwok, "Design criteria for bi-stable behavior in a buckled multi-layered MEMS bridge," *Journal of Micromechanics and Microengineering*, 16, pp. 2034–2043, 2006.

[Mih01a] R. E. Mihailovich and J. DeNatale, Personal communications, Rockwell Scientific, Agoura Hills, CA, 2001.

[Mih01b] R. Mihailovich, M. Kim, J. Hacker, E. Sovero, J. Studer, J. Higgins, and J. F. DeNatale, "MEM relay for reconfigurable RF circuits," *IEEE Microwave & Wireless Components Letters*, 11, (2), pp. 53–55, 2001.

[Mit00] G. Mitic, H.P. Degischer, G. Lefranc, and T. Licht, "AlSiC composite materials in IGBT power modules," *IEEE 2000 Industry Applications Conference*, 5, pp. 3021–3027, 2000.

[Mul00] J. B. Muldavin, and G. M. Rebeiz, "High-isolation CPW MEMS shunt switches: Modeling and design," *IEEE Trans. Microwave Theory and Techniques*, 48, (6), pp. 1045–1056, 2000.

[Mul01a] J. B. Muldavin, and G. M. Rebeiz, "Nonlinear electro-mechanical modeling of MEMS switches," *IEEE MTT-S International Microwave Theory and Techniques Symposium Proc.*, 3, pp. 2119–2122, 2001.

[Mul01b] J. B. Muldavin, “Design and analysis of series and shunt MEMS switches,” *Ph.D. Thesis, University of Michigan*, 2009.

[Nor99] B. Norvell, R. Hancock, J. Smith, M. Pugh, S. Theis, and J. Kviatkofsky, “Micro Electro Mechanical Switch (MEMS) Technology Applied to Electronically Scanned Arrays for Space Based Radar,” *Proc. IEEE Aerospace Conference*, (3), pp. 239–247, 1999.

[Obe97] E. Obermeier, “Mechanical and thermophysical properties of thin film materials for MEMS: Techniques and devices,” *Proc. Materials Research Society Symposium*, 444, pp. 39–57, 1997.

[Ozk10a] F. M. Ozkeskin, and Y. B. Gianchandani, “A Hybrid Technology for Pt-Rh and SS316L High Power Micro-Relays,” *Tech. Dig. Hilton Head Workshop 2010*, pp. 182–185, 2010.

[Ozk10b] F. M. Ozkeskin, and Y. B. Gianchandani, “Double-cantilever micro-relay with integrated heat sink for high power applications,” *PowerMEMS2010 Conference*, pp. 159–162, 2010.

[Ozk11] F. M. Ozkeskin, S. Choi, K. Sarabandi, and Y. B. Gianchandani, “Metal Foil RF Micro-Relay with Integrated Heat Sink for High Power Applications,” *Proc. 24th IEEE International Conference on Micro Electro Mechanical Systems (MEMS’11)*, pp. 776–779, 2011.

[Pac00] S. P. Pacheco, L. P. B. Katehi, and C. T. C. Nguyen, “Design of low actuation voltage RF MEMS switch,” *IEEE MTT-S International Microwave Theory and Techniques Symposium Proc.*, pp.165–168, 2000.

[Pat05] S. T. Patton, and J. S. Zabinski, “Fundamental studies of Au contacts in MEMS RF switches” *Tribology Letters*, 18, (2), pp. 215–230, 2005.

[Per03] D. Peroulis, S. P. Pacheco, K. Sarabandi, and L. P. B. Katehi, “Electromechanical considerations in developing low-voltage RF MEMS switches,” *IEEE MTT-S International Microwave Theory and Techniques Symposium Proc.*, 51, (1), pp. 259–270, 2003.

[Per04] D. Peroulis, S. P. Pacheco, K. Sarabandi and L. P. B. Katehi, “RF MEMS switches with enhanced power handling capabilities,” *IEEE Trans. Microwave Theory and Technology*, 52, (1), pp. 59–68, 2004.

[Per08] http://www.psemi.com/content/products/wireless/wir_rf_switch.html, referenced November 2011.

[Pet79] K. E. Petersen, “Micromechanical membrane switches on silicon,” *IBM Journal of Research and Development*, 23, (4), pp. 376–385, 1979.

[Pla09] http://www.platinummetalsreview.com/jmpgm/tree.do?node=978&action=open&database=cesdatabase#node978, referenced July 2011.

[Poz05] D. M. Pozar, *Microwave Engineering*, Wiley, Hoboken, NJ, 2005.

[Pre60] E. Preston, "Platinum in the Glass Industry," *Platinum Metals Review*, 4, (1), pp. 2–9, 1960.

[Pro11] http://prospector.ides.com/DataView.aspx?E=83, referenced July 2011.

[Que04] L. Que, K. Udeshi, J.-H. Park, and Y. B. Gianchandani, "A Bi-Stable Electro-thermal RF Switch for High Power Applications," *17th* IEEE International Conference on Micro Electro Mechanical Systems (MEMS'04), pp. 797–800, 2004.

[Ram05] R. Ramadoss, A. Sundaram, L.M. Feldner, RF MEMS phase shifters based on PCB MEMS technology, *IEE Electron Letters*, 41, 654–656, 2005.

[Ram07] R. Ramadoss, S. Lee, Y. C. Lee,V. M. Bright, and K. C. Gupta, "MEMS Capacitive Series Switch Fabricated Using PCB Technology," *International Journal of RF and Microwave Computer-Aided Engineering*, 17, (4), pp. 387–397, 2007.

[Rea09] M. B. Read, J. H. Lang, and A. H. Slocum, "Contact Resistance in Flat Thin Films," *Proc. 55th IEEE Holm Conference on Electrical Contacts*, pp. 303–309, 2009.

[Reb01] G. M. Rebeiz, and J. B. Muldavin, "RF MEMS Switches and Switch Circuits," *IEEE Mircrowave Magazine*, pp. 59–71, 2001.

[Reb03] G. M. Rebeiz, *RF MEMS: Theory, Design and Technology*, Wiley, Hoboken, NJ, 2003.

[Ric08] M. T. Richardson, "High Resolution Lithography-Compatible Micro-Electro-Discharge Machining of Bulk Metal Foils for Micro-Electro-Mechanical-Systems," *Ph. D. Thesis, University of Michigan*, 2008.

[Rob01] I. D. Robertson, and S. Lucyszyn, Eds., *RFIC and MMIC Design and Technology*. London, U.K.: Institution of Electrical Engineers, 2001.

[Sak99] M. Sakata, Y. Komura, T. Seki, K. Kobayashi, K. Sano, and S. Horike, "Micro machined relay which utilizes single crystal silicon electrostatic actuator," *Proc. 12th IEEE International Conference on Microelectromechanical Systems (MEMS'99)*, pp. 21–24, 1999.

[San04] H. J. Santos, G. Fischer, H.A.C. Tilmans, and J.T.M. Beek, "RF MEMS for Ubiquitous Wireless Connectivity," *IEEE Microwave Magazine*, pp. 36–49, 2004.

[Sch96] H. F. Schlaak, F. Amdt, J. Schimkat, and M. Hanke, "Silicon-microrelay with electrostatic moving wedge actuator-new functions and miniaturisation by micro mechanics," *5th International Conference on Micro Electro, Opto, Mechanical Systems and Components,* Potsdam, pp. 463–467, 1996.

[Sch98] J. Schimkat, "Contact materials in microrelays," *Proc. 11th IEEE International Conference on Microelectromechanical Systems (MEMS'98)*, pp. 190-194, 1998.

[Seg07] K. Segueni, A. S. Rollier, L. L. Garrec, R. Robin, and S. Touati, "A totally free flexible membrane : a design for low electrostatic actuation MEMS," *Proc.* IEEE International Conference on Solid-State Sensors and Actuators (*Transducers)*, pp. 461-464, 2007.

[Sem09] http://www.semikron.com/internet/webcms/online/asim/07894300_DS.pdf, referenced June 2011.

[Sha74] S. P. Sharma, "Adhesion of electrical contacts," *Proc. 3rd International Relay Conference*, 237, pp. 11–14, 1974.

[Sha76] S. P. Sharma, "Adhesion coefficients of plated contact materials," *Journal of Applied Physics*, 47, (8), pp. 3573–3576, 1976.

[She01] S. C. Shen, D. T. Becher, D. Caruth, and M. Feng, "Development of broadband low-voltage RF MEM switches," in *Proc. 2001 GaAs MANTECH Conference*, pp. 81–84, 2001.

[She02] S. C. Shen, D. T. Becher, Z. Fan, D. Caruth, and M. Feng, "Development of broadband low-voltage RF MEM switches," *Active and Passive Electric Components*, pp. 97–111, 2002.

[Shi07] E. S. Shim, W. Choi, Y. Kim, Y. Kwon, J. S. No, S. Nam, and D.-I. Cho, "Hot-Switching Test of Non-Contact Type MEMS Switch," *IEEE MTT-S International Microwave Theory and Techniques Symposium Proc.,* pp. 1809–1812, 2007.

[Sin99] A. Singh, D. A. Horsley, M. B. Cohn, A. P. Pisano, and R. T. Howe, "Batch transfer of microstructures using flip-chip solder bonding," *Journal of Microelectromechanical Systems*, 8, (1), pp. 27–33,1999.

[Sla99] P. G. Slade (editor), *Electrical Contacts: Principles and Applications*. New York: Marcel Dekker, 1999.

[Sma09] http://www.smaltec.com/, referenced June 2011.

[Son07] Y. T. Songa, H. Y. Lee, and M. Esashi, "A corrugated bridge of low residual stress for RF-MEMS switch," *Sensors and Actuators A*, pp. 818–826, 2007.

[Ste05] P. G. Steeneken, T. Rijks, J. van Beek, M. J. E. Ulenaers, J. De Coster, and R. Puers, “Dynamics and squeeze film gas damping of a capacitive RF MEMS switch,” *Journal of Micromechanics and Microengineering*, 15, pp. 176–184, 2005.

[Str01] R. D. Streeter, C. A. Hall, R. Wood, and R. Madadevan, “VHF high-power tunable RF bandpass filter using microelectromechanical (MEM) microrelays,” *International Journal of RF and Microwave Computer-Aided Engineering*, 11, (5), pp. 261–275, 2001.

[Sun05] A. Sundaram, R. Ramadoss, and L.M. Feldner, Electronically steerable antenna array using PCB-based MEMS phase shifters, *Proc. of the 31st Annual Conference of the IEEE Industrial Electronics Society (IECON’05)*, pp. 2341–2345, 2005.

[Sut01] A. Sutono, N.G. Cafaro, J. Laskar, and M.M. Tentzeris, “Experimental Modeling, Repeatability Investigation and Optimization of Microwave Bond Wire Interconnects,” *IEEE Trans. on Advanced Packaging*, pp. 595- 603, Nov. 2001

[Sze81] S. M. Sze, *Physics of Semiconductor Devices*, John Wiley & Sons, New York, 1981.

[Tak02] K. Takahata, and Y. B. Gianchandani, “Batch Mode Micro-Electro-Discharge Machining,” *Journal of Microelectromechanical Systems*, 11, (2), pp. 102–110, 2002.

[Tak05] K. Takahata, “Batch Manufacturing Technology Based on Micro-Electro-Discharge Machining and Application to Cardiovascular Stents,” *PhD Dissertation, University of Michigan*, 2005.

[Tan02] G. L. Tan and G. M., “A DC-Contact MEMS Shunt Switch,” *IEEE Microwave and Wireless Components Letters,* 12, (6), pp. 212–214, 2002.

[Tay98] W. P. Taylor, O. Brand, and M. G. Allen, “Fully Integrated Magnetically Actuated Micromachined Relays,” *Journal of Microelectromechanical Systems*, 7, (4), pp. 181–191, 1998.

[Tou08] S. Touati, N. Lorphelin, A. Kanciurzewski, R. Robin, A. S. Rollier, O. Millet, and K. Segueni, “Low actuation voltage totally free flexible RF MEMS switch with antistiction system,” *MEMS/MOEMS, Design, Test, Integration and Packaging Symposium*, pp. 66–70, 2008.

[Tsa11] C.-C. Tsai, Y.-S. Cheng, T.-Y. Huang, Y. A. Hsu, and R.-B. Wu, “Design of Microstrip-to-Microstrip Via Transition in Multilayered LTCC for Frequencies up to 67 GHz,” *IEEE Trans. on Components, Packaging and Manufacturing Technology*, 1, (4), pp. 595–601, 2011.

[Uhl10] R. Kulke, and P. Uhlig, “LTCC Technology for RF Applications,” *Electrical and Electronic Engineering for Communication Workshop*, *EEEfCOM 2010*, 2010.

[Vps11] http://www.vp-scientific.com/parylene_properties.htm, referenced June 2011.

[Web07] B. S. Weber, and L. C. Kretly, "PCB-MEMS RF Switch: Parametric analysis and design guide lines", *IEEE MTT-S International Microwave Theory and Techniques Symposium Proc.*, pp. 141–144, 2007.

[Won00] J.-E. Wong, J. H. Lang, and M. A. Schmidt, "An electrostatically-actuated MEMS switch for power applications," *Proc. 13th IEEE International Conference on Microelectromechanical Systems (MEMS'00),* pp. 633–638, 2000.

[Woo98] R. Wood, R. Madadevan, V. Dhuler, B. Dudley, A. Cowen, E. Hill, and K. Markus, "MEMS microrelays," *Mechatronics*, 8, pp. 535–547, 1998.

[Xu06] G. Xu, X. H. Mingwu, and Y. M. Jiao, "A novel comb electrostatic microrelay with lateral-driven," *8th International Conference on Solid-State and Integrated Circuit Technology (ICSICT)*, pp. 658–660, 2006.

[Zah79] M. Zahn, *Electromagnetic Field Theory: A Problem Solving Approach*, John Wiley & Sons, New York, NY, 1979.

[Zav97] P. M. Zavracky, S. Majumder, and N. E. McGruer, "Micromechanical switches fabricated using nickel surface micromachining," *Journal of Microelectromechanical Systems*, 6, pp. 3–9, 1997.

[Zav99] P.M. Zavracky, N.E. McGruer, R.H. Morrison, and D. Potter, "Microswitches and microrelays with a view toward microwave applications," *Int. J. RF Microwave CAE*, 9, pp. 338–347, 1999.

[Zha02a] Y. P. Zhao, "Morphological stability of epitaxial thin elastic films by van der Waals force," *Archive of Applied Mechanics*, 72, (1), pp. 77–84, 2002.

[Zha02b] Y. P. Zhao, and W. J. Li, "Surface stability of epitaxial elastic films by the Casimir force," *Chinese Physics Letters*, 19, (8), pp. 1161–1163, 2002.

[Zha03] L. X. Zhang, and Y. P. Zhao, "Electromechanical model of RF MEMS switches," *Microsystem Technologies,* 9, (6-7), pp. 420–426, 2003.

[Zit99] M. Zitouni, F. Morancho, H. Tranduc, P. Rossel, J. Buxo, I. Pagès, and S. Merchant, "A new lateral power MOSFET for smart power ICs: the "LUDMOS concept,"" *Microelectronics Journal*, 30, (6), pp. 551–561, 1999.